Hydrated silica on Mars:
Global comparison and in-depth analysis at Antoniadi Crater

Matthew R. Smith

A dissertation
submitted in partial fulfillment of
the requirements for the degree of

Doctor of Philosophy

University of Washington

2012

Reading Committee:

Alan Gillespie, Chair
Joshua Bandfield, Co-Chair
David Montgomery

Program Authorized to Offer Degree:
Department of Earth and Space Sciences

University of Washington

Abstract

Hydrated silica on Mars:
Global comparison and in-depth analysis at Antoniadi Crater

Matthew R. Smith

Chairs of the Supervisory Committee:

Professor Alan Gillespie
Professor Joshua Bandfield
Department of Earth and Space Sciences

Hydrated silica is found in a variety of Martian deposits within suites of minerals that indicate aqueous alteration, mostly because hydrated silica forms easily in different environments. Because of its relative ubiquity on Mars, it makes a good tracer mineral to compare otherwise dissimilar deposits and relate their relative degrees of aqueous alteration. The first portion of this dissertation uses near-infrared and thermal-infrared spectroscopy to determine the relative degree of crystallinity of hydrated silica and the bulk SiO_2 abundance of hydrated-silica-bearing surfaces. This analysis reveals that Martian hydrated silicas exhibit a range of crystalline structures, from noncrystalline (opal-A or hydrated glass) to crystalline (quartz), implying a range in the maturity of these silica deposits.

However, bulk SiO_2 abundances show less diversity, with most Martian silica deposits having relatively low SiO_2 abundances, similar to a basaltic andesitic composition that exists over much of the surface and that suggests little interaction with water.

The second portion of this dissertation focuses on one location that contains the only detected quartz on the planet. High-resolution satellite imagery and thermal and near-infrared spectroscopy is used to construct a geologic history of these deposits and their local context. The quartz-bearing deposits are consistently found co-located with hydrated silica, and this spatial coherence suggests that the quartz formed as a diagenetic product of amorphous silica, rather than as a primary igneous mineral. Diagenetic quartz is a mature alteration product of hydrated amorphous silica, and indicates more persistent water and/or higher temperatures at this site. There is also spectral evidence for smectites beneath the silica-bearing rocks, in the lowermost exposed Noachian-aged breccia. A similar stratigraphic sequence — smectite-bearing breccias beneath deposits containing minerals indicating a greater degree of alteration — has also been found at nearby exposures at Nili Fossae and Toro Crater, suggesting a widespread sequence of alteration. The two sections of this dissertation provide a global and in-depth view of Martian hydrated silica deposits, thereby broadening and refining our search for past water on Mars.

TABLE OF CONTENTS

LIST OF FIGURES iii

LIST OF TABLES iv

Chapter 1 | Hydrated silica on Mars 1
1.1 Nature and varieties of hydrated silica 2
1.1.1 Hydrated silicate glass 3
1.1.2 Opal-A (non-crystalline silica) 4
1.1.3 Opal-C/CT 4
1.1.4 Chalcedony 5
1.1.5 Microquartz (microcrystalline or fine quartz) 6
1.1.6 Summary of hydration of silica phases 6
1.2 Formation of hydrated silica 7
1.2.1 Primary silica precipitation 7
1.2.2 Diagenetic alteration sequence of silicas 9
1.2.3 Secondary mineral replacement 9
1.2.4 Summary of crystallinity as an indicator of formation conditions 10
1.3 Spectroscopic detection of silica 12
1.3.1 Near-infrared (NIR) spectroscopy 12
1.3.2 Thermal-infrared (TIR) spectroscopy 14

Chapter 2 | Antoniadi Crater and Northern Syrtis Major 26

Chapter 3 | Datasets and methods 29
3.1 Compact Reconnaissance Imaging Spectrometer for Mars [CRISM] 29
3.1.1 Instrument and data processing 29
3.1.2 Spectral analysis 30
3.1.3 Relative degree of silica crystallinity from near-infrared data 31
3.2 Thermal Emission Spectrometer [TES] 33
3.3 Thermal Emission Imaging System [THEMIS] 34
3.3.1 SiO_2 abundance from TIR data and the 'center of gravity' 35
3.3.2 Surface thermal inertia 37
3.3.3 Decorrelation stretch images 38
3.4 High-Resolution Imaging Science Experience [HiRISE] 38
3.5 Context Camera [CTX] 39

Chapter 4 | Global characterization of Martian hydrated silica deposits 47
4.1 Relative crystallinity and bulk composition of Martian hydrated silica 47
4.1.1 Determination of relative crystallinity from CRISM 47
4.1.2 SiO_2 abundance from thermal spectroscopy 49
4.2 Discussion 51
4.2.1 Implications for alteration environment 51
4.2.2 Spatial relationships between thermal and near-infrared silica detections 53
4.2.3 Comparison of orbitally detected and "Home Plate" silica 55
4.2.4 Synthesis of global Martian silica study 58

Chapter 5 | Geology and spectroscopy of the Antoniadi Crater region 67
5.1 Large Elliptical Depression 67
5.1.1 Geologic context 67
5.1.2 Spectral identifications 70

5.2 Small Elliptical Depression 72
5.2.1 Geologic context 72
5.2.2 Spectral identifications 73
5.3 Rim Crater Ejecta 74
5.3.1 Geologic context 74
5.3.2 Spectral identifications 75
5.4 Syrtis Craters 75
5.4.1 Geologic context 75
5.4.2 Spectral identifications 77
5.5 Summary of observations 78
Chapter 6 | Discussion and implications for the Antoniadi Crater region 93
6.1 Geologic and aqueous history of the region 93
6.1.1 Age of the deposits 93
6.1.2 Regional extent of alteration 94
6.1.3 Geological sequence 95
6.2 Silica: Diagenesis, terrestrial examples and implications for the duration of water 100
6.3 Broader geologic context 107
6.3.1 Other exposures in the Syrtis Major region 107
6.3.2 Global context 113
6.3.3 Geology on a reworked planet 116
6.3.4 Summary and unresolved questions 118
6.4 Astrobiological implications of the observed mineral phases 120
Chapter 7 | Summary and conclusions 125
Bibliography 128
Appendix A: Omission of silicas in Mawrth Vallis and Arabia Terra 142

LIST OF FIGURES

1.1 Map of locations of Martian hydrated silica 21
1.2 Near-infrared spectra of hydrated silica varieties with attributed bands 22
1.3 Diagnostic near-infrared band indices for different silica species 23
1.4 Relationship of Reststrahlen band minima and SiO_2 content in the TIR 24
1.5 Behavior of the crystallinity indices for opal-A under Martian conditions 25
3.1 Summed-Gaussian fits to NIR features of hydrated silica 45
3.2 'Center of gravity' of multispectral thermal data 46
4.1 CRISM spectra of Martian hydrated silica deposits 61
4.2 Relative degree of crystallinity for Martian hydrated silica 62
4.3 'Center of gravity' λ for Martian silica, Surface Types 1/2, and lab minerals 63
4.4 Distribution of silica in N. Syrtis Major crater 64
4.5 Distribution of silica in Nili Patera 65
4.6 Distribution of silica in Toro Crater 66
5.1 'Context image of Antoniadi Crater region 80
5.2 Context map of Large Elliptical Depression province 81
5.3 Geomorphology and spectra of the Large Elliptical Depression 82
5.4 Light-toned aeolian sediments in the Large Elliptical Depression 83
5.5 Co-located quartz and hydrated silica-bearing surfaces 84
5.6 Hydrated silica detections in the Small Elliptical Depression 85
5.7 Possible sources of high-silica sediments 86
5.8 Context map of Rim Crater province 87
5.9 Rim Crater ejecta units and spectra 88
5.10 Context map of Syrtis Craters province 89
5.11 Silica concentration along transport of mobile sediments 90
5.12 Phyllosilicate-bearing surfaces in the Syrtis Craters 91
5.13 Silica transport and concentration in SW Syrtis Crater 92
6.1 'Crystallinity indices' of Antoniadi Crater and other Martian silicas 122
6.2 Context map for sites adjacent to Antoniadi Crater 123
6.3 Comparison of cross-sections of adjacent altered mineral suites 124
A.1 Arabia Terra/Mawrth Vallis hydrated silica spectra comparison 144

LIST OF TABLES

1.1 Locations of published CRISM detections of hydrated silica 18
1.2 Crystallinity and water content of hydrated silica species 19
1.3 Near-infrared vibrational species in hydrated silica 20
3.1 CRISM and HiRISE image IDs for Antoniadi Crater region 40
3.2 Images and locations of CRISM spectra of global Martian silica 41
3.3 Images and locations of CRISM spectra in the Antoniadi Crater region 42
3.4 Specifications for continuum removal and curve-fitting algorithms 43
3.5 THEMIS and TES data of hydrated silica locations 44
4.1 Calculated silica parameters (relative % and degree of crystallinity) 60

ACKNOWLEDGEMENTS

I would like to sincerely thank the whole of the Department of Earth and Space Sciences for its steadfast support and guidance throughout my time as a graduate student. There is no member of the faculty or staff, nor graduate student, that did not give his or her time generously and selflessly to aid me on my way toward academic and personal growth. I would especially like to thank my advisors: Alan Gillespie, for teaching me the invaluable lesson that intellectual breadth is the path to a fulfilling and richer quest for knowledge, and Josh Bandfield, for instilling a spirit of inquisitive flexibility to avoid entrenched dogmatic beliefs. Were it not for the help, friendship, and love of my friends and colleagues — especially Kat Huybers, Dave Williams, Ariah Kidder, Adam Campbell, and many others — I would be the lesser person for it. Thank you all.

Chapter 1 | Hydrated silica on Mars

Hydrated silica is a common and widespread mineral phase on Mars, detected in many recent studies with both orbital and *in situ* measurements. Orbital instruments have detected hydrated silica in a variety of terrains (Table 1.1; Figure 1.1), in association with phyllosilicates [*Ehlmann et al.,* 2009; *Marzo et al.*, 2010; *Wray et al.*, 2011; *Weitz et al.*, 2011] and sulfates [*Milliken et al.*, 2008; *Squyres et al.,* 2008] in both Hesperian [*Skok et al.,* 2010; *Amador and Bandfield*, 2011] and Noachian-aged units [*Bandfield et al.,* 2004a; *Bandfield,* 2006; *Smith and Bandfield,* 2012]. In two locations, the mineral phase of the hydrated silica has been determined with thermal spectroscopy: opaline silica at Western Hellas [*Bandfield*, 2008] and quartz at Antoniadi Crater [*Bandfield et al.,* 2004a; *Bandfield,* 2006]. *In situ* observations by the Spirit Rover have also detected hydrated opaline silica [*Rice et al.*, 2010] in nodules and in white soils, estimated to contain up to 98 wt% silica [*Squyres et al.*, 2008; *Ruff et al.,* 2011]. Because it is found in a variety of alteration mineral suites, it may be a useful tracer mineral across eras in ancient Martian geologic history thought to represent varying amounts of water and pH conditions.

Hydrated silica has been studied extensively in the terrestrial literature, and as a category encompasses a suite of minerals and crystal structures. This chapter seeks to

describe the different varieties of hydrated silica, how they form, and how they may be detected on other planetary surfaces.

1.1 Nature and varieties of hydrated silica

The term 'hydrated silica' is commonly applied to a family of minerals that are comprised almost entirely of $SiO_2 \cdot nH_2O$ (< 0.5–1 mol% non-volatile impurities; *Graetsch,* 1994) with water and/or hydroxyl (OH) either structurally bound or adsorbed on surfaces [*Flörke et al.,* 1991]. Water molecules are associated with the silica in two ways: as isolated single molecules of non-hydrogen-bonded H_2O that are trapped in isolated "cages" in the silica structure ('H_2O Type A'), and as strongly hydrogen-bonded water molecules ("liquid water") that form interstitial films on silica surfaces and within micropores ('H_2O Type B') [*Langer and Flörke,* 1974]. Also, hydroxyl (OH) is also found as two varieties within hydrated silica associated with Si–OH bonding: as isolated Si–OH molecules within the crystal structure at structural defects ('Si–OH Type A'), and as hydrogen-bonded Si–OH along mineral surfaces ('Si–OH Type B') [*Langer and Flörke,* 1974]. The relative amounts of the Types A and B of water and Si–OH that exist within hydrated silica are found in various proportions depending on the crystalline structure of the hydrated silica phase [*Langer and Flörke,* 1974; *Flörke et al.*, 1982].

There are many varieties of natural hydrated silica, with both non-crystalline and microcrystalline structures (Table 1.2). Macrocrystalline silica (quartz) has a very regular crystalline structure and lacks void space that allows for only trace amounts of water/hydroxyl (<0.1 wt%) along dislocations and defects within the crystal lattice [*Aines and Rossman*, 1984], and therefore is not generally regarded as hydrated. I will briefly describe the common varieties of hydrated silica using the nomenclature of *Flörke et al.* [1991] and *Smith* [1998], with specific attention to their crystallinity and types of water, also summarized in Table 1.2.

1.1.1 Hydrated silicate glass

Hydrated silicate glass is an igneously derived phase that forms directly from hydrous melts through rapid quenching and consists of a poorly crystalline structure with bound H_2O and OH. Though not typically discussed alongside the purer phases of hydrated silica, silicate glasses have likewise been shown to contain OH, H_2O and Si–OH bonds, which make them close mimics with other silica phases when remotely detected with near-infrared spectroscopy [*Wu,* 1980]. *Stolper* [1982] also showed that all H_2O, OH, and Si-OH molecules in silicate glasses are isolated and structurally bound (Type A) because they do not exhibit infrared absorption ice bands when frozen, suggesting that the water is monomeric.

1.1.2 Opal-A (non-crystalline silica)

Opal-A is a non-crystalline form of hydrated silica, and is made of a random network of silica tetrahedra. Opal-A is further subdivided by *Langer and Flörke* [1974] into two types: opal-A_G (gel-like) and opal-A_N (network). Opal-A_G is the more common variety of opal-A, comprised of closely packed silica nanospheres (~100–500 nm in diameter) with interstitial water in pore space and individual water/hydroxyl molecules located in isolated cages within the spheres [*Flörke et al.* 2008]. Opal-A_N (hyalite) is a silica glass that forms a network structure that is distinct from opal-A_G in that it is semi-infinite, rather than in discrete spheres [*Smith*, 1998].

Compared to silicate glasses, more of the bound water in opal-A is Type B (surficial, not structurally bound), meaning that a greater amount of water forms interstitial films or fills void spaces in the more porous microstructures of these phases [*Langer and Flörke,* 1974].

1.1.3 Opal-C/CT

Opal-C and opal-CT are composed of intermixed cristobalite (C) and tridymite (T), and considered "paracrystalline" polymorphs because their crystal structure is made of stacked parallel layers of the two minerals instead of a full three-dimensional structure [*Flörke et al.,* 2008]. The geometry of the layer structures of cristobalite and tridymite share similar ring shapes and are largely interchangeable [*Heaney,* 1994], resulting in

the common and relatively stable polymorphs that are intimate intergrowths of the two minerals: opal-CT (~50% cristobalite, 50% tridymite) and opal-C (mainly cristobalite, possibly 20–30% tridymite; *Graetsch et al.,* 1994).

The water within opal-C/CT has an increasingly greater proportion of Type B water than opal-A; opal-CT has 73% Type B water [*Langer and Flörke,* 1974], and the water in opal-C is estimated to be almost entirely Type B [*Graetsch et al.,* 1985]. This trend is attributed to two factors: the increasing amount of void space that may be occupied by interstitial water, and the increasing degree of crystallinity which disallows H_2O to exist in structural defects or cages, as it does in opal-A.

1.1.4 Chalcedony

Chalcedony is a microcrystalline variety of quartz, composed of bundles of radial fibers of crystallites or individual spherulites 50–100 nm in size [*Flörke et al.,* 1982]. Chalcedony, unlike macrocrystalline quartz, has small-scale porosity and is able to incorporate water along its microscopic grain boundaries and within pores. Much of this pore water exists within closed pores (~0.1 μm in diameter; *Folk and Weaver*, 1952), and is not easily lost when subject to temperatures >100°C [*Flörke et al.,* 1982]. Chalcedony has a more rigid three-dimensional structure than opals, and consequently has less water [*Graetsch et al.,* 1985; *Florke et al.*, 1991]. Furthermore, water in chalcedony cannot exist within isolated "cages" such as those that exist in the relatively

loose silica network of opals, and therefore nearly all water in chalcedony is Type B hydrogen-bonded water [*Flörke et al.,* 1982].

1.1.5 Microquartz (microcrystalline or fine quartz)

Microquartz is a microcrystalline equigranular variety of quartz, composed of ≤ 20 μm grains [*Folk and Weaver,* 1952; *Flörke et al.,* 1991]. Like chalcedony, microquartz may contain many micropores that are capable of housing small amounts of water (< 0.3–1.5 wt%; *Flörke et al.,* 1982; *Flörke et al.,* 2008), which is mainly in closed pores and not lost easily when heated [*Flörke et al.,* 1982]. The type and varieties of structural and liquid water have been less thoroughly studied in microquartz than in other varieties, though they are thought to be similar to chalcedony; water is likely housed along grain boundaries and micropores and is hydrogen-bonded rather than isolated, which has been confirmed through spectroscopic investigation of laboratory samples [*Flörke et al.,* 1982].

1.1.6 Summary of hydration of silica phases

As shown in Table 1.2, there is a trend of decreasing water content with increasing crystallinity, which is most apparent with the large decrease between the opals and microcrystalline quartz (chalcedony, microquartz). However, a stronger trend among all phases is the shift in the types of bound H_2O water, which vary from almost entirely Type A in hydrated silicate glasses to entirely Type B for opal-C and microcrystalline

quartz. This decrease in structurally bound Type A water reflects the increase in structural order of the microcrystalline varieties, which are less likely to incorporate structural water impurities into their regular structure, and instead carry water in pore space and hydrogen-bonded to silanol groups along their internal surfaces [*Iler,* 1979; *Dove and Rimstidt,* 1994].

1.2 Formation of hydrated silica

On modern-day Earth, formation and precipitation of hydrated silica are dominated by the influence of oceanic benthic organisms [*Carozzi*, 1993]. However, because this discussion is framed in the context of Martian mineralogy, only abiotic formation mechanisms will be discussed. Hydrated silica can form abiotically in one of three ways: 1) a primary precipitate from solution, 2) as a diagenetic alteration product, or 3) as a replacement mineral. Each of these formation methods will be briefly described here.

1.2.1 Primary silica precipitation

The precipitation of hydrated silica directly from solution is the main formation method for opal-A, a common formation method for chalcedony, and a minor contributor to terrestrial deposits of opal-CT, opal-C, and microquartz.

Opal-A typically forms as a primary precipitate through the mobilization and reprecipitation of silica through chemical weathering [*Frondel,* 1962]. Silica is easily liberated when silica-bearing rocks are subjected to even minor aqueous alteration [*McLennan,* 2003], with dissolution rates increasing with greater pH, temperature, pressure, or decreased salinity [*Williams et al.,* 1985; *Dove and Rimstidt*, 1994]. As silica becomes supersaturated in solution, opal-A is energetically favored to precipitate at Martian surface temperatures and pressures [*Rimstidt and Barnes*, 1980; *Dove and Rimstidt,* 1994].

Chalcedony commonly forms as a primary precipitate in late-stage hydrothermal systems in igneous rocks, lining walls of veins or vugs [*Frondel*, 1962]. It requires specific conditions to form: slight silica supersaturation, possibly acidic conditions [*Heaney*, 1993], temperatures below 180°C, and low pressures [*Fournier*, 1985].

Quartz may also precipitate directly from solution that is originally in equilibrium with rocks at temperatures between 200–340°C and cooled slowly enough so that only a weak supersaturation is attained [*Fournier*, 1985].

1.2.2 Diagenetic alteration sequence of silicas

The most common formation mechanism for paracrystalline (opal-CT, opal-C) and crystalline (microquartz) phases is through the diagenetic alteration of an opal-A precursor [*Hesse,* 1989; *Knauth*, 1994]. Opal-A is metastable at terrestrial surface temperatures and pressures, and will undergo a reorganization of its structure through dissolution and reprecipitation in water, with the common pathway of opal-A → opal-CT → opal-C → chalcedony → microquartz [*Williams and Crerar*, 1985; *Herdianita et al.,* 2000; *Lynne et al.*, 2005]. This transformation requires the dissolution of silica, and thus proceeds more rapidly in conditions where silica solubility is higher: elevated temperatures, higher pH, lower salinity, and higher pressures [*Williams et al.,* 1985]. However, this process will proceed in the same manner, albeit more slowly, in any system with liquid water and has been estimated to proceed entirely to quartz in a maximum of 400 Ma under Martian surface conditions (0°C) [*Tosca and Knoll*, 2009].

1.2.3 Secondary mineral replacement

Silica also commonly replaces pre-existing minerals in sedimentary rocks. Most often this occurs in limestone or dolostone beds, with opal-A or opal-CT precipitating as nodules and undergoing diagenetic transition to more crystalline phases [*Maliva and Siever*, 1988; *Gao and Land*, 1991]. Silica also commonly replaces terrestrial evaporites, including replacement of magnesium or sulfate-bearing evaporites with chalcedony [*Folk and Pittman*, 1971], or the formation of chalcedony in magadi-type cherts through

replacement of hydrous sodium silicates (magadiite, kenyaite) derived from alkaline brines [*Eugster,* 1967, 1969; *Rooney et al.*, 1969].

1.2.4 Summary of crystallinity as an indicator of formation conditions

Though hydrated silica may form in several ways, there is a general observable trend: increasing crystallinity is correlated with an increasing degree of aqueous alteration. The "degree of aqueous alteration" here is defined as the reaction of precursor rock or regolith with water and the combined effect of variables that affect the rate of alteration: heat, pressure, alkalinity and salinity. For example, as it is used here, a deposit may experience a similar degree of aqueous alteration when it interacts with a hot solution for a short time versus cooler solution for a much longer amount of time, assuming that reaction rate has an Arrhenius-like exponential dependence on temperature. Because these variables are difficult to uncouple when detecting remote surfaces, they will be discussed here collectively.

In the case of diagenetic formation of crystalline species, the relationship between the degrees of crystallinity and aqueous alteration is straightforward: as opal-A is subjected to a greater degree of aqueous alteration, it will progressively transform via diagenesis to a phase that more crystalline phases: opal-CT → opal-C → chalcedony » quartz [*Williams et al.,* 1985].

For the primary precipitation of silica, this trend is also observed. Unlike opal-A, which precipitates in deposits subject to only minor alteration [e.g. *Carozzi,* 1993], chalcedony and microquartz typically form as primary deposits as late-stage precipitates from hydrothermal systems [*Frondel,* 1962]. This is because crystalline forms of silica require very slight degrees of supersaturation to precipitate, which only occurs in long-lived hydrothermal systems after the more easily dissolvable fraction of the host rocks has been removed and precipitated as opaline silica [*Fournier,* 1985]. In early-stage hydrothermal systems in igneous rocks, the fluids are commonly in equilibrium with volcanic glass, which results in high silica concentrations as the system cools at the surface or comes into contact with more alkaline waters, preferentially precipitating opal-A. After volcanic glass is flushed from the system, typically within several weeks [*Rimstidt and Barnes,* 1980], hydrothermal systems then establish equilibrium with quartz, and achieve the low saturations required for quartz or chalcedony precipitation. Thus, the degree of alteration increases for more crystalline species even during primary precipitation.

The most poorly constrained formation mechanism is that of the magadi-type cherts due to their scarcity on Earth. However, their formation may also involve an opal-A precursor, and the conversion from the precursor magadiite to chalcedony is estimated to take hundreds of years under wet conditions [*Eugster,* 1969], also suggesting that the presence of chalcedony indicates a relatively high degree of aqueous alteration.

1.3 Spectroscopic detection of silica

On Mars, there are currently two methods to detect silica on a global scale and/or remotely discriminate between silica phases: near-infrared and thermal-infrared spectroscopy. Each dataset provides a unique and complementary view of silica that may be used.

1.3.1 Near-infrared (NIR) spectroscopy

With near-infrared (1–3 μm) spectroscopy, there are several diagnostic absorption features in its reflectance spectrum caused by the combinations of vibrational overtones of hydroxyl, water, and silanol (SiOH) that have been used to identify and characterize hydrated silica [*Anderson and Wickersheim,* 1964; *Langer and Flörke,* 1974; *Flörke et al.,* 1982; *Aines and Rossman,* 1984; *Graetsch*, 1994; *Goryniuk et al.,* 2004]. The locations and attributions of the different hydrated-silica near-infrared absorption bands are listed in Table 1.3 and shown in Figure 1.2.

Studies by *Anderson and Wickersheim* [1964], *Langer and Flörke* [1974] and *Flörke et al.* [1982] demonstrated that there are unique contributions of the different species of water — "Type-A" or "Type B" H_2O and Si-OH described in Section 1.1 — to the near-infrared spectra of different varieties of hydrated silica. More importantly, they showed that the spectral differences between varieties of hydrated silica reflect the various

proportions of different water/hydroxyl species in their crystal structure, suggesting that hydrated silica species may be spectroscopically discriminated by the differences in the way they held their bound water. This was confirmed in a recent study by *Rice et al.* [2012] that analyzed the near-infrared spectra of laboratory silicas and found systematic differences in their near-infrared spectra related to the bands attributed to water/hydroxyl (Figure 1.3). *Rice et al.* [2012] showed that the location of the absorption-band minimum of the 1.4 μm OH–H_2O band and the relative strengths of the 1.91 and 1.96 μm H_2O bands were the most diagnostic indicators in distinguishing between silica phases (Figure 1.3). Specifically, they showed that crystallinity was correlated with both a longer-wavelength band minimum for the 1.4 μm feature and a lower ratio of 1.91/1.96 μm band depths. Thus, they have demonstrated that it is feasible to use only the near-infrared spectrum of hydrated silica to determine the crystallinity of observed silica.

Although the results of *Rice et al.* [2012] may not be directly applied to studies of Martian hydrated silica, they may still be capable of determining the *relative* degree of crystallinity of silica deposits. This is because their study was mostly performed under ambient conditions, whereas the dry Martian atmosphere will likely change the hydration behavior of hydrated silica and modify its near-infrared spectrum. This change in its NIR spectrum, however, is predictable based on laboratory observations of how hydrated silica loses its loosely bound water. Studies by *Langer and Flörke* [1974] and *Graetsch et al.* [1985] demonstrated that the most easily liberated water in

hydrated silica was molecular interstitial water (Type B), and that the proportion of water lost under similar heating conditions decreased from opal-A→ opal-CT/C→ microcrystalline quartz. When Type B water is lost, the effect on the spectral shape is a shift of the 1.4 μm band toward shorter wavelengths and an increase of 1.91/1.96 μm band ratio. This was confirmed by *Rice et al.* [2012], who subjected a single opal-A sample to Martian atmospheric conditions (5 Torr CO_2) for 442 days and observed the band indices shift in the predicted direction (Figure 1.5). The trend observed by *Rice et al.* [2012] occurs along roughly the same trend direction as between opaline and crystalline silica varieties measured under ambient conditions. Because these changes in hydration are more pronounced among noncrystalline and paracrystalline varieties of silica than with microcrystalline varieties, subjecting them to Martian conditions would presumably act to accentuate the trend empirically derived by *Rice et al.* [2012]. Thus, it is still valid to use the overall trend shown in Figure 1.3 as an indicator of the relative degree of crystallinity, though not as a direct relationship between indices and crystal phase.

1.3.2 Thermal-infrared (TIR) spectroscopy

Compared with near-infrared spectroscopy, a more direct method of inferring silica phase is with thermal spectroscopy, which has often been used as a reliable method to differentiate between silica species both in the laboratory [*Lippincott et al.,* 1958; *Michalski et al.,* 2003], as well as on natural surfaces on Earth [*Vaughan et al.,* 2003; 2005] and Mars [*Bandfield et al.,* 2004a; *Bandfield,* 2006; *Glotch et al.*, 2006; *Ruff et al.,*

2011]. Thermal spectroscopy is sensitive to Si–O bending and stretching vibrations between 3 and 30 μm, which differ between silica phases [e.g. *Lippencott et al.,* 1958]. However, many detections of hydrated silica on Mars (except at two locations: Antoniadi Crater [*Bandfield et al.,* 2004a] and Western Hellas [*Bandfield,* 2008]) are too small to be seen with the Thermal Emission Spectrometer (TES; Section 3.2), which is the only orbiting thermal spectrometer with sufficient spectral resolution to differentiate among silica phases. Thus, remote detection of silica phase using thermal-infrared spectroscopy is not currently possible in most cases on Mars.

However, an advantage of thermal spectroscopy that is not possible with near-infrared spectroscopy is the capability of measuring quantitative abundances of minerals, as has been done effectively on Earth [e.g. *Adams and Gillespie,* 2006] and Mars [e.g. *Bandfield et al.,* 2000a]. It is specifically well-suited for determining the bulk SiO_2 abundance of surfaces, by measuring the location of a diagnostic Reststrahlen (fundamental molecular vibration) band between 8 and 12 μm, which shifts to longer wavelengths with lower bulk SiO_2 abundances [Figure 1.4; *Lyon*, 1965], and is measurable even with few spectral bands [*Vincent and Thomson,* 1972; *Gillespie and Abbott*, 1984; *Walter and Salisbury,* 1989]. Thus, the relative silica concentration may be determined with the higher spatial resolution Thermal Emission Imaging Spectrometer (THEMIS; Section 3.3) that is capable of resolving the small hydrated silica deposits.

If we assume that Mars is primarily composed of low-silica materials — Surface Types 1 (basaltic) and 2 (andesitic) — then it may be assumed that, when analyzing a surface determined to contain hydrated silica, that any elevated silica concentration could be attributed to a greater degree of aqueous alteration. This argument was made by *Ruff et al.* [2011] who stated that the hydrated silica deposits at Gusev Crater necessitated high water-to-rock ratios for sustained periods of time to mobilize and concentrate the large amounts of silica that are observed. On Earth, a common process and possible analog for Martian aqueous alteration is the semi-arid weathering of Hawaiian basalts, where surfaces coated with basaltic dust are leached to form a surficial high-silica coating that grows with age [*Farr and Adams,* 1984] and exhibits a detectable increase in multispectral thermal-infrared spectroscopy between younger and older deposits [*Kahle et al.,* 1988]. Thus, for Martian hydrated silica deposits, if we assume that the SiO_2 abundance of a hydrated silica-bearing surface is controlled through the production of silica from weathering, then we may use the SiO_2 abundance of the surface as a proxy for their degree of alteration.

With this in mind, this investigation to characterize Martian hydrated silica has two goals:

1. Analyze all detections of hydrated silica on Mars to determine the relative degree of crystallinity, using the diagnostic near-infrared spectral indices of *Rice et al.* [2012]
2. Determine the bulk SiO_2 abundance of the hydrated silica deposits using thermal spectroscopy to infer the degree of aqueous alteration.

Tables for Chapter 1

Table 1.1 — Published locations of Martian hydrated silica detected with CRISM as of April 2012. (*) corresponds to locations in Figure 1.1.

#*	*Location*	*Center Lat, Lon*	*References*
1	N. Syrtis Major (near Antoniadi Crater)	18.5°N, 65.15°E	*Ehlmann et al.* [2009]; *Smith and Bandfield* [2012]
2 3	Isidis Basin	23.54°N, 69.54°E (1) 20.75°N, 75.81°E (2)	*Ehlmann et al.* [2009]
4	Toro Crater	17.36°N, 71.86°E (1) 17.07°N, 71.90°E (2)	*Marzo et al.* [2010]
5	Nili Patera	8.92°N, 67.29°E (1) 9.13°N, 67.59°E (2)	*Skok et al.* [2010]; *Amador and Bandfield* [2011]
6	Western Hellas	43.42°S, 48.13°E	*Bandfield* [2008]
7	Terra Sirenum (near Columbus Crater)	33.20°S, 192.56°E	*Wray et al.* [2011]
8	Noctis Labyrinthus	10.44°S, 261.55°E	*Weitz et al.* [2011]
9	Melas Chasma	11.09°S, 281.99°E	*Milliken et al.* [2008]
10	Juventae Chasma	4.65°S, 296.39°E	*Milliken et al.* [2008]

Table 1.2 — Crystallinity and water content of hydrated silica species.

Silica Phase	*Crystallinity*	*Water Content (wt %)*	*% Bound water (H_2O)*		*Reference*
			Type A	*Type B*	
Hydrated glass	Noncrystalline	0.06–6.8	~ 100	~ 0	*Stolper* [1982]
Opal-A_G	Noncrystalline (particulate)	5–8	50	50	*Langer and Flörke* [1974]
Opal-A_N	Noncrystalline (massive)	3–8	33	66	*Langer and Flörke* [1974]
Opal-CT	Paracrystalline (2-D stacking of cristobalite/tridymite)	3–10	27	73	*Langer and Flörke* [1974]; *Graetsch et al.* [1994]
Opal-C		1–8	~ 0	~ 100	*Graetsch et al.* [1985]; *Graetsch et al.* [1994]
Chalcedony	Micro- or cryptocrystalline (50–100 nm quartz crystallites)	0.5–2	~ 0	~ 100	*Flörke et al.* [1982]
Microquartz	Microcrystalline (≤ 20 μm quartz grains)	< 0.3–1.5	~ 0	~ 100	*Flörke et al.* [1982]

Table 1.3 — Near-infrared vibrational species in hydrated silica.

λ (μm)	*υ (cm^{-1})*	*Vibrating Molecule*[*]	*Notes*
1.38	~7250	OH [$2\nu_{OH}$][a,b,c,d,e]	Isolated (non H-bonded); sharp, clear band
1.41	~7090	OH [$2\nu_{OH}$][c,d,f,g]	Hydrogen (H)-bonded
1.46	~6850	H_2O [$2\nu_2+\nu_3$[e,h]; $2\nu_3$[h]; $\nu_1+\nu_3$[h,i]]	H-bonded H_2O; vibrational modes are debated
1.91	~5240	H_2O [$\nu_2+\nu_3$][e,h,i]	Type A (isolated)[†]
1.96	~5100	H_2O [$\nu_2+\nu_3$][h,i]	Type B (H-bonded)[†]
2.21	~4520	SiOH [$\delta+\nu_{OH}$][i]	Type A (isolated)[†]
2.26	~4420	SiOH [$\delta+\nu_{OH}$][i]	Type B (H-bonded)[†]

[*] *ν_1: symmetric stretch; ν_2: bending; ν_3: asymmetric stretch; ν_{OH}: OH stretch; δ: SiOH bending*

† *Types A and B are described in Section 1.1, and defined in Langer and Flörke [1974].*

a. *Errera and Mollet* [1936]
b. *Buswell et al.* [1937]
c. *McDonald* [1958]
d. *Anderson and Wickersheim* [1964]
e. *Herzberg* [1945]
f. *Hunt* [1977]
g. *Aines and Rossman* [1984]
h. *Bayly et al.* [1963]
i. *Langer and Flörke* [1974]

Figures for Chapter 1

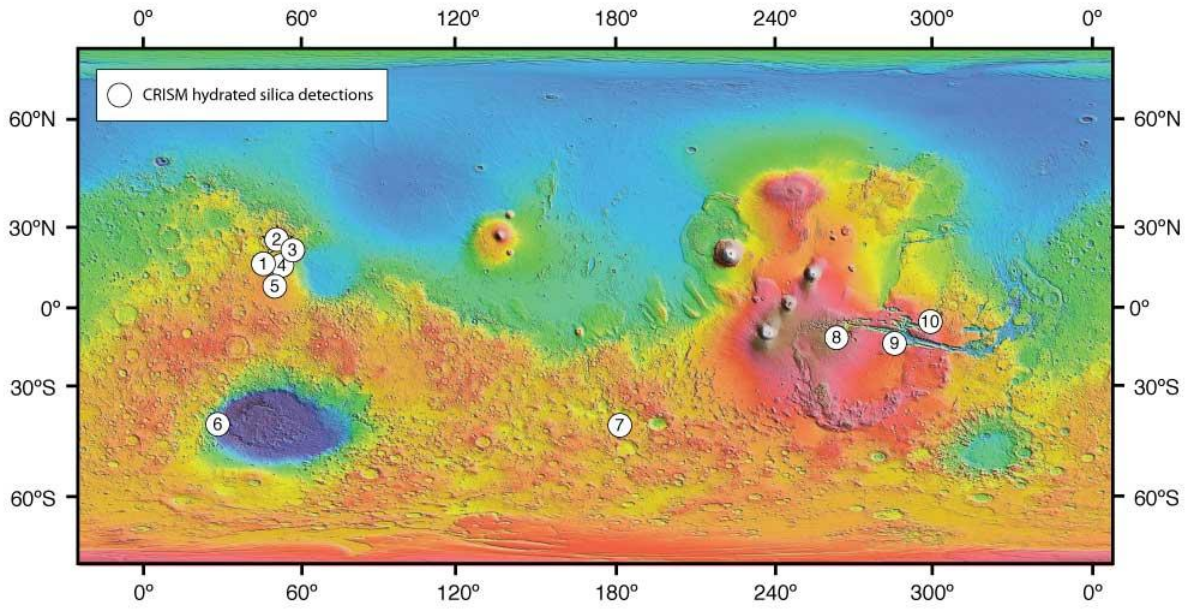

Figure 1.1 — Map of locations of hydrated silica detected with CRISM. Numbers correspond to locations in Table 1.1.

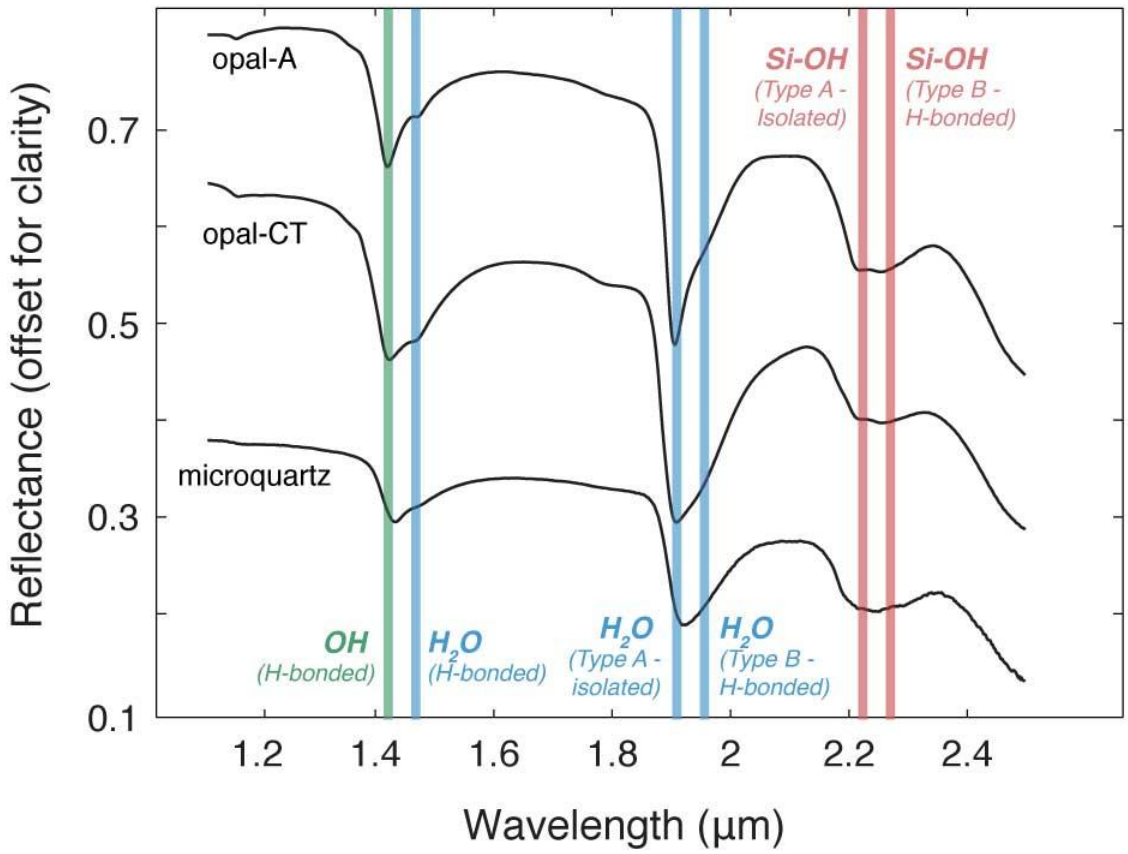

Figure 1.2 — Near-infrared spectra of varieties of hydrated silica (spectra courtesy of E. Cloutis, University of Winnipeg). Absorption bands are labeled with their causal molecule. Further information on vibrational modes is given in Table 1.3.

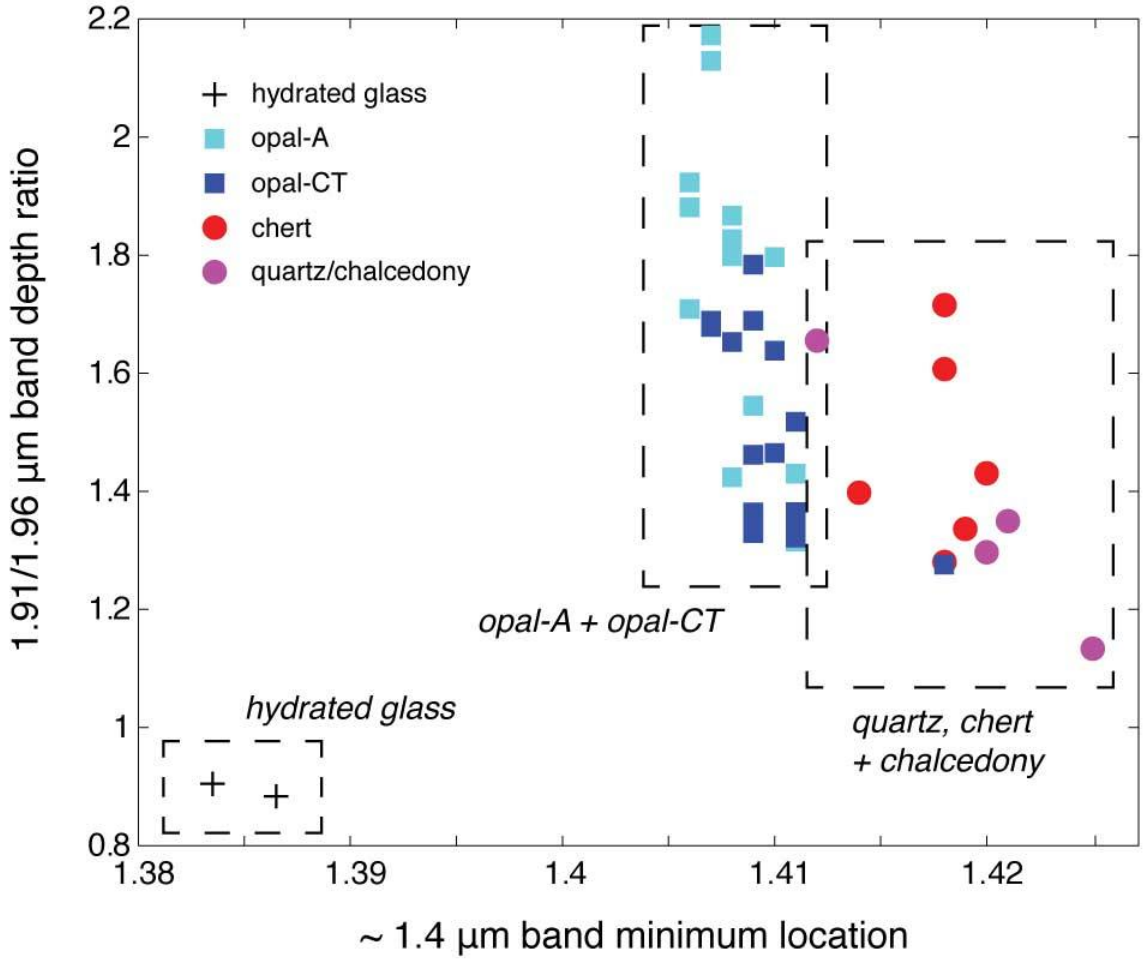

Figure 1.3 — Diagnostic band indices to identify distinguish among silica species, calculated from spectra collected on laboratory samples (modified from *Rice et al.* [2012]). Chert is a rock that is primarily composed of microcrystalline quartz with minor chalcedony [*Knauth, 1994*].

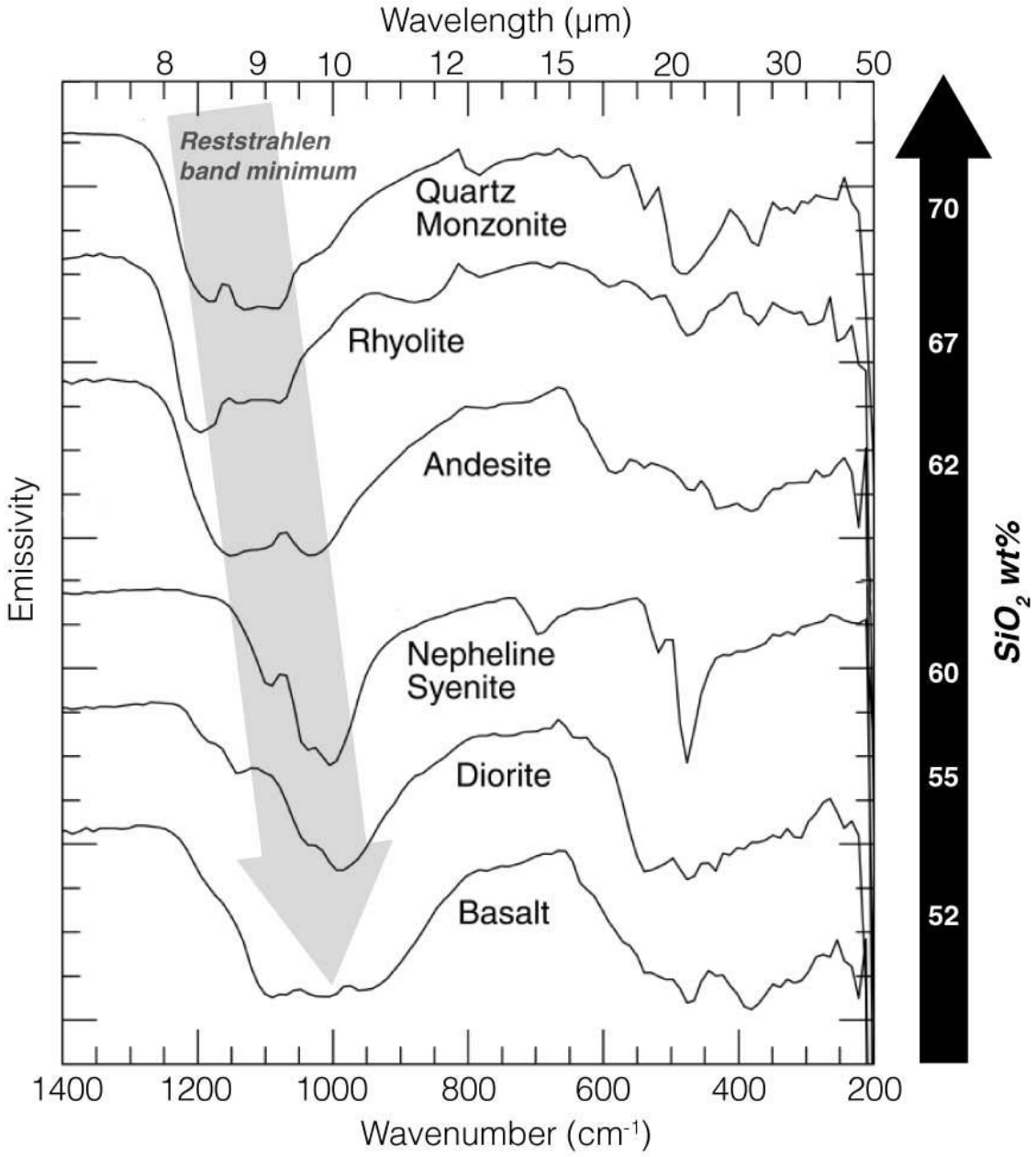

Figure 1.4 — Thermal-infrared spectra of many igneous compositions, depicting the negative trend between decreasing SiO_2 abundance with increasing Reststrahlen band minimum wavelength (located between 1300 and 800 cm^{-1} [8–11 μm]). The location of this band minimum may be used to ascertain relative bulk SiO_2 abundance of hydrated silica deposits.

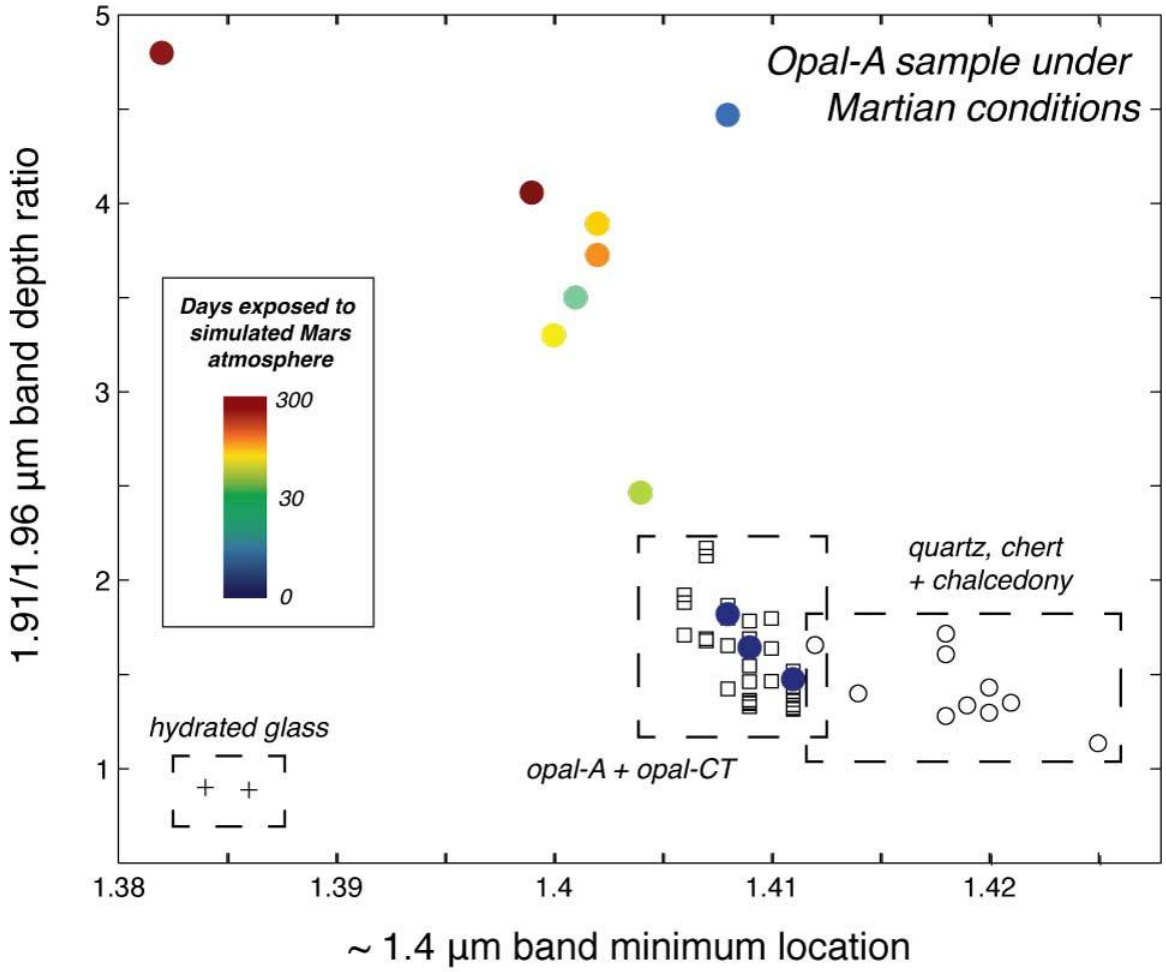

Figure 1.5 — Change in spectral indices for an opal-A sample under Martian conditions [modified from *Rice et al.*, 2012]. As opal-A loses its interstitial water, its band indices move toward the upper left of the plot, accentuating the trend of crystallinity, where more crystalline forms of hydrated silica plot in the lower right. Points marked by boxes (e.g. "hydrated glass," "opal-A") are from Figure 1.3.

Chapter 2 | Antoniadi Crater and Northern Syrtis Major

To accompany the global perspective of hydrated silica, the second section of this dissertation (Chapter 5 and Chapter 6) will delve into greater detail in one location of hydrated silica within the northern Syrtis Major region near Antoniadi Crater (64°E, 19°N). This area is unique on Mars for being the only location identified from orbital data to exhibit thermal-infrared spectral signatures consistent with the presence of crystalline quartz, found in isolated exposures in impact craters [*Bandfield et al.*, 2004a] and in nearby knobby and fractured terrains [*Bandfield*, 2006]. All detected quartz is co-located with plagioclase feldspar, which had implied that these exposures might represent a felsic pluton that was later excavated by impacts [*Bandfield, et al.,* 2004a]. All Martian surfaces described thus far suggest a mafic composition (abundant in minerals that contain iron and magnesium, such as pyroxenes), and felsic compositions (high in quartz and plagioclase) have not been previously found on Mars. Martian surfaces are dominated by two thermal-infrared spectrally defined compositions [*Bandfield et al.,* 2000a]: Surface Type I, a basaltic composition, and Surface Type 2, a more silica-rich composition assumed to have a greater proportion of volcanic glass (i.e. andesitic basalt) [*Bandfield et al.*, 2000a] or alternatively explained as a partially weathered basalt [*Wyatt and McSween*, 2002]. The least mafic Martian surface yet detected is a lava flow in Nili Patera rich in Si-K glass, and determined to be dacitic [*Christensen et al.*, 2005]. Because of the scarcity of felsic surfaces on Mars, the detection of quartz- and plagioclase-rich rocks near Antoniadi Crater is anomalous and so far unexplained.

This area was also imaged with the CRISM instrument as part of a larger study of the Nili Fossae region to search for hydrated and altered mineral phases [*Ehlmann et al.,* 2009]. They found that the detections of felsic minerals in two impact craters were spatially associated with minerals formed under aqueous conditions: hydrated silica on crater floors, Fe/Mg-phyllosilicate minerals (e.g. nontronite, saponite) on the craters' central peaks, and putative minor outcrops of zeolites also on the central peaks. Similar to hydrated silica, phyllosilicate minerals are widespread on Mars, most commonly found in ancient Noachian terrains [*Bibring et al.,* 2006; *Murchie et al.,* 2009; *Ehlmann et al.* 2011]. However, the apparent persistence of both opaline silica (Chapter 1) and smectitic clays for billions of years suggests limited interaction with water after their formation [*Tosca and Knoll,* 2009]. Likewise, smectite clays like those common in Noachian terrains preferentially transform to more stable illite or chlorite, often under elevated temperatures on Earth, leaving smectite clays uncommon in the terrestrial geologic record [*Weaver*, 1989].

The second section of this dissertation (Chapter 5 and Chapter 6) documents the association of the unusual outcrops of quartz and plagioclase with the hydrated silica and phyllosilicates, and uses the complementary information given by the detections from the two wavelength ranges (thermal-infrared and near-infrared), as well as high-resolution visible imagery, to construct a more thorough geologic history of this location. Specifically, I will investigate if the felsic and hydrated minerals are spatially

linked, and if the unique presence of quartz is related to the hydrous alteration of opaline silica, as is commonly observed on Earth. If so, this site may represent more sustained water and greater degree of crystallinity than all other Martian exposures of hydrated silica.

Chapter 3 | Datasets and methods

Similar techniques were used to analyze the Martian surfaces in both of the main components of this dissertation. Therefore, the datasets and methods used to study both will be discussed together. When instruments or methods pertain to only one specific section, it will be noted explicitly.

3.1 Compact Reconnaissance Imaging Spectrometer for Mars [CRISM]

3.1.1 Instrument and data processing

CRISM is a hyperspectral imaging visible/near-infrared spectrometer onboard the 2005 Mars Reconnaissance Orbiter (MRO) [*Murchie et al.,* 2007]. CRISM has 544 spectral bands between 0.4 and 4.0 μm and there are two data-collection modes used for this study: full-resolution targeted (FRT) observations (spatial resolution of 15–19 m/pixel) and half-resolution long-targeted observations (HRL) (spatial resolution of 36 m/pixel and double the spatial coverage of FRT images).

All CRISM data used for this study were derived from the TRR3 data products that incorporate improved destriping and noise reduction over the previous TRR2 products [*Seelos et al.*, 2011]. Atmospheric gas absorptions were removed using the scaled

volcano-scan method described by *McGuire et al.* [2009]. This method uses the difference spectrum between the summit and base of Olympus Mons to isolate the gas absorption features. The resulting spectrum is scaled to the depth of the 2.0 μm CO_2 absorption feature for each pixel in the image and subtracted from the retrieved radiance of each pixel to remove its effects. Scenes are converted to I/F — defined as the ratio between the radiance measured by the sensor divided by solar irradiance divided by pi — and corrected for solar incidence angle.

3.1.2 Spectral analysis

CRISM scenes were first analyzed by use of spectral index maps, where the spectrum of each pixel in the scene is analyzed for diagnostic absorption features to determine the distribution of specific minerals. Many spectral index maps are released as standard data products that accompany CRISM scenes and some were developed for this study, such as for hydrated silica. The hydrated silica index that is used is sensitive to the diagnostic absorption at 2.21 μm due to vibrational overtones of Si–OH bonds, and explicitly calculated as the ratio between the average of the CRISM I/F values between 2.10 and 2.16 μm (CRISM bands 262–271) relative to the average CRISM I/F between 2.19 and 2.29 μm (CRISM bands 243–257). However, the hydrated silica spectral index map is not uniquely sensitive to hydrated silica but is also somewhat sensitive to other minerals with absorptions in this 2.1–2.3 μm spectral range (e.g., kaolinite, montmorillonite, illite). To avoid false detections that may arise in index maps, analysis

is then corroborated through examination of the full spectrum to locate diagnostic absorption features.

When an area warrants further analysis, an average surface spectrum is calculated over the area for comparison of the spectral shape. The average spectrum is ratioed against a nearby region that is lacking narrow absorption features (null region) to further reduce noise, cancel systematic errors and residual atmospheric effects in the data and accentuate mineral absorption features [e.g., *Milliken et al.*, 2008; *Ehlmann et al.,* 2009]. In nearly all cases, the target and null regions are located in the same column to reduce the impact of cross-image artifacts (e.g., spectral "smile", column-correlated noise: *Parente,* 2008). Locations of all collected CRISM spectra used for the global silica survey are listed in Table 3.2; image IDs for all CRISM footprints are used in the analysis of the Antoniadi Crater region are listed in Table 3.1 and specific locations for all collected spectra are listed in Table 3.3.

3.1.3 Relative degree of silica crystallinity from near-infrared data

To ascertain the relative crystallinity of global silica, I used the "crystallinity indices" of *Rice et al.* [2012] (Section 1.3.1) to quantitatively compare between isolated spectra. However, many of the CRISM spectra are too noisy to determine specific band minimums and relative band depths confidently, especially for those collected for surfaces that are smaller than ten CRISM pixels (~0.004 km^2). To reduce the noise, I fit the absorption features at 1.4, 1.9, and 2.2 μm with a continuous best-fit function meant

to approximate their spectral shape (Figure 3.1). The function used was a sum of Gaussian functions similar to the technique employed by *Sunshine et al.* [1990] for near-infrared laboratory spectra of minerals, and shown to be adequate for approximating the shapes of water and hydroxyl bands [*Wilkins,* 1967; *Langer and Flörke,* 1974].

For these spectra, the individual features are isolated and continuum removed [e.g., *Clark and Roush*, 1984]. The isolated features are then inverted, and their minimum values set to zero, so that their shapes could be fit with traditionally described Gaussian functions. Each inverted and normalized feature is then fit with a sum of two Gaussian functions (inputs into the band-fitting algorithm are listed in Table 3.4):

$$f = \alpha_1 e^{-\frac{(\lambda-\beta_1)^2}{2\psi_1^2}} + \alpha_2 e^{-\frac{(\lambda-\beta_2)^2}{2\psi_2^2}}$$

Equation 3.1

where α represents the depth of the feature at its peak, β is its center wavelength, and ψ relates to its width. The subscripts *1* and *2* indicate the two individual features that are being summed to approximate each feature — ~ 1.41 and 1.46 μm for the 1.4 μm feature, ~ 1.91 and 1.96 μm for the 1.9 μm feature, and ~ 2.21 and 2.26 μm for the 2.2 μm feature. Curve fitting was performed using a non-linear least-squares best-fit algorithm that uses Equation 3.1 to determine the optimal $\alpha_{1,2}$, $\beta_{1,2}$, and $\psi_{1,2}$ for each absorption feature iteratively. The initial condition for the band centers are the theoretical centers, stated above and in Table 3.4 (e.g. 1.41 μm, 1.46 μm, etc.). The initial conditions for band width and depth are arbitrary, and only chosen so that they

converge on a stable solution. From these Gaussian fits of the retrieved Martian spectra, the diagnostic indices defined by *Rice et al.* [2012] for silica phases were determined: the band minimum for the 1.4 μm feature and the ratio of spectral band depths for the 1.91 and 1.96 μm features.

A common feature of Martian near-infrared spectra is a weak or missing 1.4 μm OH vibrational overtone, because hydration features tend to wane under cold and dry conditions [*Clark,* 1981; *Bishop and Pieters,* 1995]. In cases where the band depth of the continuum-removed 1.4 μm feature was less than 0.007, it was unresolvable below the level of noise and excluded from study.

3.2 Thermal Emission Spectrometer [TES]

TES is a Fourier transform Michelson interferometer (FTIR), with a spectral range between 6 and 50 μm (~1650–200 cm^{-1}), with spectral resolution between 5 and 10 cm^{-1} [*Christensen et al.,* 1992]. TES is comprised of three cross-track and two along-track detectors with a spatial sampling of 8.3 mrad, which corresponds to a spatial footprint of 3 × 8 km from its orbiting height of 380 km. The elongated pixel dimension is due to a lack of image-motion compensation, which was not implemented due to the extended period of MGS aerobraking resulting in spacecraft groundtrack motion in a direction opposite of that which was originally intended.

TES atmospheric correction is done by performing a linear deconvolution — a linearly squared fit of retrieved spectra — using atmospheric and surface spectra as endmember inputs [*Bandfield et al.,* 2000b; *Smith et al.,* 2001a]. More details of the instrument specifications, including radiometric and operation calibration are found in *Christensen et al.* [2001]. For this dissertation, TES was used primarily to enable atmospheric correction for the higher-resolution THEMIS imaging spectrometer.

3.3 Thermal Emission Imaging System [THEMIS]

THEMIS is a multispectral visible, near-infrared, and thermal imager onboard the 2001 Mars Odyssey orbiter. It has ten thermal spectral channels that are spaced between 6.5 and 15 μm, and has a spatial sampling of ~100 m/pixel and swath width of 32 km. The thermal portion of the sensor is an uncooled 320 × 240 element microbolometer array which produces calibrated radiance images using an internal calibration flag and instrument-response functions assembled from pre-launch data. Some effects of focal-plane temperature drift are determined from variations in measured radiance within the 15 μm CO_2 band (THEMIS band 10) and removed. The calibration procedures and errors are described further by *Christensen et al.* [2004] and *Bandfield et al.* [2004b].

THEMIS data was atmospherically corrected using a two-step process: 1) isolate a large, and spectrally uniform region with a variety of surface temperatures (e.g., shaded and

sunlit slopes) and use the range of values to isolate and remove the additive contributions of atmospheric emission and scattering, and 2) use atmospherically corrected TES data from the same region as the THEMIS scene to provide the multiplicative contributions for atmospheric attenuation in each band. Assuming that the atmosphere is constant across the image (this is generally the case in areas of small elevation differences and low water-ice opacity), these multiplicative terms may be applied on a per-pixel basis to retrieve atmospherically corrected surface emissivity spectra at the full spatial resolution of THEMIS [*Bandfield et al.,* 2004b].

3.3.1 SiO_2 abundance from TIR data and the 'center of gravity'

As part the global silica survey, for each location in Table 1.1 that was resolvable with THEMIS resolution, atmospherically corrected emissivity data were collected to describe its bulk composition with thermal spectroscopy. Locations used for THEMIS analysis and their associated TES atmospheric correction data are listed in Table 3.5. In order to determine the SiO_2 abundance of the surface, the location of the band minimum was calculated for each atmospherically corrected THEMIS spectra. The minima were taken to be the locations of the diagnostic Reststrahlen bands between 8 and 12 μm, whose locations correlate with bulk SiO_2 abundance of the surface (Figure 1.4) [e.g. *Walter and Salisbury,* 1989]. Due to the coarse (0.6–2.3 μm) spectral resolution of the ten-band THEMIS, I employed a method developed by *Vincent and Thomson* [1972], which analyzes multispectral thermal-infrared data and identifies the

so-called 'center of gravity' of the spectrum, defined in Equation 3.2 and depicted graphically in Figure 3.2:

$$\int_{\lambda_0}^{\lambda_g} 1-\varepsilon = 0.5 \int_{\lambda_0}^{\lambda_{max}} 1-\varepsilon$$

Equation 3.2

where λ_g is defined as the 'center of gravity' wavelength, λ_0 and λ_{max} are the minimum and maximum wavelengths of the spectrum and ε is emissivity. λ_g is a reasonable approximation of the location of the true band minimum as measured in multi-spectral data, and is well correlated with the true bulk SiO_2 abundance of rocks [*Vincent and Thomson,* 1972].

A caveat to this technique is that the 'center of gravity' of a thermal spectrum is not a direct measure of amorphous silica content, but only of the spectral shape consistent with silica-rich materials. There are other minerals (clays, zeolites, serpentine) that also have spectral features in the TIR and would affect this index. Though, these minerals have not been detected with CRISM, even though near-infrared spectroscopy is especially sensitive to them even in sufficiently small concentrations as to be undetectable with thermal spectroscopy [*Rogers and Bandfield*, 2009]. Because these minerals have not been detected with CRISM, this indicates that they are, at maximum, in very small concentrations that would not contribute measurably to their thermal spectrum.

3.3.2 Surface thermal inertia

As part of the analysis of Antoniadi Crater region, Nighttime THEMIS IR data were used to calculate the thermal inertia of the surface using a method simplified from that described in *Fergason et al.* [2006a]. We used the KRC thermal model [*Kieffer et al.*, 2000], which has been used in a wide variety of applications [e.g. *Titus et al.*, 2003; *Fergason et al.*, 2006a,b; *Bandfield and Feldman,* 2008; *Bandfield and Edwards*, 2008; *Edwards et al.,* 2009] and produces results similar to other models [e.g. *Mellon et al.*, 2000, *Putzig et al.*, 2005]. Thermal inertia was calculated for each THEMIS pixel using regional averages for latitude, season, local time, albedo, elevation, and atmospheric opacity. The use of parameters applied on a regional, rather than per-pixel, basis may result in slight variations in derived thermal inertia, with the largest effects present on steep slopes of variable azimuth orientations. Although these effects appear in the data, they are not of a magnitude that changes the qualitative interpretation of the surface materials, which is the primary use for this study. In addition, effects of differences in surface albedo largely dissipate during the night and the resulting effects on nighttime surface temperature do not affect the interpretation of the nature of surface materials [*Mellon et al.*, 2000; *Bandfield and Feldman*, 2008]. Other parameters, such as elevation and atmospheric opacity, do not vary significantly across the scenes used for this study. Comparison of rover and orbital measurements using this method agree to within 10% [*Fergason et al.,* 2006a].

Surface brightness temperatures are estimated using THEMIS band 9 (centered at 12.6 μm). This is a wavelength where the atmosphere is relatively transparent when water-ice clouds are absent, surface emissivity is relatively high, and the data have high signal-to-noise ratios for typical Martian nighttime surface temperatures. The limited temperature contrast between the Martian surface and atmosphere at night at low latitudes also minimizes the effect of the atmosphere on retrieved surface temperatures.

3.3.3 Decorrelation stretch images

Also as part of the investigation into the Antoniadi Crater region, decorrelation stretch (DCS) images [*Gillespie et al.*, 1986], derived as standard products from THEMIS-IR data [*Bandfield et al.*, 2004b], were analyzed to assess spectral variability across the image and to rapidly identify distinct spectral units. Units that have been previously identified as quartz- and plagioclase-bearing (quartzofeldspathic), appearing yellow, yellow and magenta in DCS images using bands 8-7-5, 9-6-4, and 6-4-2 for R-G-B, respectively, were identified and compared with other spectral and morphologic datasets.

3.4 High-Resolution Imaging Science Experience [HiRISE]

HiRISE, a high-resolution camera onboard Mars Reconnaissance Orbiter, was used for isolated and detailed morphological and textural distinctions between rock units, breccia

blocks or sediments, and to provide a geomorphic context for spectral observations. HiRISE is able to collect images at ~30 cm/pixel in both grayscale (6 km swath width) and color (1.2 km swath width), with spectral filters detecting blue-green (400–580 nm), red (570–830 nm), and infrared (790–1100 nm) wavelengths. A detailed description of the HiRISE experiment may be found in *McEwen et al.* [2007]. HiRISE images used for this study are listed in Table 3.1.

3.5 Context Camera [CTX]

CTX, a medium-resolution visible imager onboard MRO, was used to provide lower spatial resolution information on morphology and surface characteristics over broad regions. CTX collects monochromatic visible wavelength images at ~5.5 m/pixel with a swath width of 30 km. CTX images fully cover all regions analyzed in this study. Additional technical details describing the CTX instrument characteristics may be found in *Malin et al.* [2007].

Tables for Chapter 3

Table 3.1 — CRISM and HiRISE image IDs for each province within the Antoniadi Crater region. Provinces described further in Chapter 5.

Province	*CRISM Image IDs*	*HiRISE Image IDs*
Large Elliptical Depression	FRT00007CBB	ESP_018883_2010; ESP_019305_2010
Small Elliptical Depression	HRL0001330D	ESP_016048_2004
Rim Crater Ejecta	FRT0000862C; FRT0000B7B7; HRL0000BF4D; FRT000090F8; FRT0000A94C; FRT0000AB8D	PSP_009534_1995; PSP_006673_2000
Syrtis Crater (SW)	FRT00009BCE; FRT0000A2B3; FRT0000B4F8; FRT0000B9D3; FRT0000C059; FRT0000CEF7; FRT000118C9; FRT000135DB; HRL000098E4; HRL0000A88D	ESP_017116_1985; ESP_022074_1985; ESP_023208_1985; PSP_001385_1985; PSP_006607_1985; PSP_006963_1990; PSP_007108_1985; PSP_007464_1985; PSP_008110_1990; PSP_009613_1985; PSP_010391_1985
Syrtis Crater (NE)	FRT000051EE; FRT00009312; FRT00009E5D; FRT0000BD3A; HRL0000AC95	ESP_013015_2000; PSP_003205_2000; PSP_003706_2000; PSP_007253_2000; PSP_009402_2000

Table 3.2 — Locations of pixels used in the global silica section for calculated CRISM spectra. An average spectrum is calculated for the target and nearby null surfaces and the two average spectra are divided to obtain the displayed ratio spectrum. Pixel locations are for unprojected and correctly oriented CRISM data (north is at the top of the image). (*) denotes an average of multiple spots of one scene.

Location Name	*CRISM Image ID*	*Numerator bounding pixels = target region*	*Denominator bounding pixels = null region*
Isidis Basin 1	FRT00007B7A	X: 185–187; Y: 351–352	X: 185–187; Y: 328–332
Isidis Basin 2	FRT0000B573	X: 182–185; Y: 261–264	X: 182–185; Y: 216–229
Juventae Chasma	FRT00005814	X: 112–118; Y: 144–153	X: 112–118; Y: 96–121
Melas Chasma	HRL000044AC	X: 107–125; Y: 202–211	X: 107–125; Y: 170–179
N. Syrtis Major	FRT0000A2B3	X: 39-–8; Y: 75–100	X: 39–58; Y: 16–41
Nili Patera 1	FRT000082EE	X_1: 237–240; Y_1: 71–73 X_2: 131–135; Y_2: 119–121*	X_1: 237–240; Y_1: 384–386 X_2: 131–135; Y_2: 248–250*
Nili Patera 2	FRT0000B80F	X_1: 459–462; Y_1: 147–150 X_2: 469–473; Y_2: 196–198*	X_1: 459–462; Y_1: 244–247 X_2: 469–473; Y_2: 260–262*
Noctis Labyrinthus 1	FRT000096EE	X: 127–132; Y: 274–283	X: 127–132; Y: 22–31
Noctis Labyrinthus 2	FRT000096EE	X: 68–76; Y: 243–251	X: 68–76; Y: 26–34
Terra Sirenum 1	FRT00010EC5	X: 338–354; Y: 45–63	X: 338–354; Y: 90–108
Terra Sirenum 2	FRT00010EC5	X_1: 282 –304; Y_1: 289–296 X_2: 299–311; Y_2: 278–292*	X_1: 282–304; Y_1: 304–311 X_2: 299–311; Y_2: 307–321*
Toro Crater 1	FRT00009786	X: 425–431; Y: 32–34	X: 425–431; Y: 37–42
Toro Crater 2	FRT0000B1B5	X: 33–36; Y: 204–208	X: 33–36; Y: 227–237
Western Hellas	HRL00013366	X: 155–170; Y: 328–344	X: 155–170; Y: 390–402

Table 3.3 — Locations of pixels used in the study of the Antoniadi Crater region for calculated CRISM spectra. Spectra were acquired as described in Section 3.1 and Table 3.2.

Spectrum ID [Figure #]	*CRISM Image ID*	*Numerator bounding pixels = target region*	*Denominator bounding pixels = null region*
S1 [5.3C]	FRT00007CBB	X: 480–490; Y: 219–233	X: 480–490; Y: 185–199
S2 [5.3C]	FRT00007CBB	X: 461–474; Y: 232–242	X: 461–474; Y: 184–194
S3 [5.3C]	FRT00007CBB	X: 537–545; Y: 92–96	X: 537–545; Y: 48–52
S4 [5.6C]	HRL0001330D	X: 185–188, Y:65–70	X: 185–188; Y: 20–32
S5 [5.6C]	HRL0001330D	X: 200–207; Y: 65	X: 200–207; Y: 91–95
S6 [5.6C]	HRL0001330D	X: 226–228; Y: 58–60	X: 226–228; Y: 37–46
S7 [5.6C]	HRL0001330D	X: 223–227; Y: 74–77	X: 223–227; Y: 89–93
S8 [5.6C]	HRL0001330D	X: 193–201; Y: 79–81	X: 193–201; Y: 94–100
S9 [5.6C]	HRL0001330D	X: 183–190; Y: 74–77	X: 183–190; Y: 90–97
S10 [5.7D]	FRT0000A2B3	X: 39–58; Y: 75–100	X: 39–58; Y: 16–41
S11 [5.7D]	FRT00009EFD	X: 150–156; Y: 85–91	X: 150–156; Y: 18–24
S12 [5.7D]	HRL0001330D	X: 184–191; Y: 65–77	X: 184–191; Y: 20–32
S13 [5.9C]	FRT000090F8	X: 423–427; Y: 395–398	X: 423–427; Y: 383–391
S14 [5.9D]	FRT0000862C	X: 352–362; Y: 271:279	X: 352–362; Y: 352–360
S15 [5.11C]	FRT00009E5D	X: 292–306; Y: 175–188	X: 292–306; Y: 55–68
S16 [5.11C]	FRT00009E5D	X: 150–156; Y: 282–289	X: 150–156; Y: 301–308
S17 [5.11C]	FRT00009E5D	X: 163–176; Y: 142–153	X: 163–176; Y: 331–342
S18 [5.11C]	FRT00009E5D	X: 125–144; Y: 41–55	X: 125–144; Y: 374–388
S19 [5.12C]	FRT00009312	X: 300–307; Y: 250–255	X: 300–307; Y: 209–214
S20 [5.12F]	FRT0000B9D3	X: 415–421; Y: 347–350	X: 415–421; Y: 464–480
S21 [5.13B]	FRT0000A2B3	X: 121–125; Y: 159–163	X: 121–125; Y: 258–262
S22 [5.13B]	FRT0000A2B3	X: 138–146; Y: 121–124	X: 138–146; Y: 106–109
S23 [5.13B]	FRT0000A2B3	X: 102–108; Y: 129–138	X: 102–108; Y: 256–165
S24 [5.13B]	FRT0000A2B3	X: 72–84; Y: 113–121	X: 72–84; Y: 269–277

Table 3.4 — Specifications for continuum removal (*) and starting conditions for summed-Gaussian fit algorithm (ǂ).

λ (μm) of broad feature	*Left Edge λ (μm)**	*Right Edge λ (μm)**	*Initial β_1 ,β_2 (μm) (Band centers)ǂ*	*Initial α_1 ,α_2 (Band depth)ǂ*	*Initial ψ_1 ,ψ_2 (Band width)ǂ*
1.4	1.35	1.6	1.41, 1.46	0.01, 0.0006	0.05, 0.002
1.9	1.82	2.13	1.91, 1.96	0.3, 0.001	0.05, 0.01
2.2	2.13	2.35	2.21, 2.26	0.01, 0.003	0.2, 0.01

Table 3.5 — Specifications for THEMIS and TES data used for thermal spectroscopic analysis. Sites identified with CRISM that were too small to be resolved with THEMIS: Melas Chasma, Nili Patera 2, Noctis Labyrinthus 1 & 2, Toro Crater 2. Western Hellas spectrum is taken from *Bandfield* [2008]

Location Name	*THEMIS Image ID*	*Bounding Lat. (south, north)*	*Target mineral loc.*	*Location of TES data*	*TES Orbital No. (ock)*	*TES icks*
Isidis Basin 1	I37961009	22.4°N, 24.5°N	X: 265–278 Y: 576–583	X: 160–260 Y: 837–910	3962	1970–1972
Isidis Basin 2	I03505002	19°N, 21.4°N	X: 20–49 Y: 293–312	X: 95–165 Y: 750–950	3094	1941–1944
Juventae Chasma	I40874001	6.6°S, 3.9°S	X: 264–277 Y: 508–509	X: 250–290 Y: 800–880	5325	1691–1693
N. Syrtis Major	I01221005	19°N, 20.4°N	X: 234–237 Y: 257–260	X: 300–320 Y: 430–530	2956	1936–1938
Nili Patera 1	I17771017	8.2°N, 9.6°N	X: 297–298 Y: 301–301	X: 40–150 Y: 680–800	3937	1825–1828
Terra Sirenum 1	I15284003	34.6°S, 32.8°S	X: 189–193 Y: 198–206	X: 250–340 Y: 490–600	5203	1432–1436
Terra Sirenum 2	I15284003	34.6°S, 32.8°S	X: 192–193 Y: 251–252	X: 250–340 Y: 490–600	5203	1432–1436
Toro Crater 1	I36401029	16.3°N, 20.3°N	X: 233–244 Y: 231–248	X: 15–115 Y: 385–535	3069	1920–1922

Figures for Chapter 3

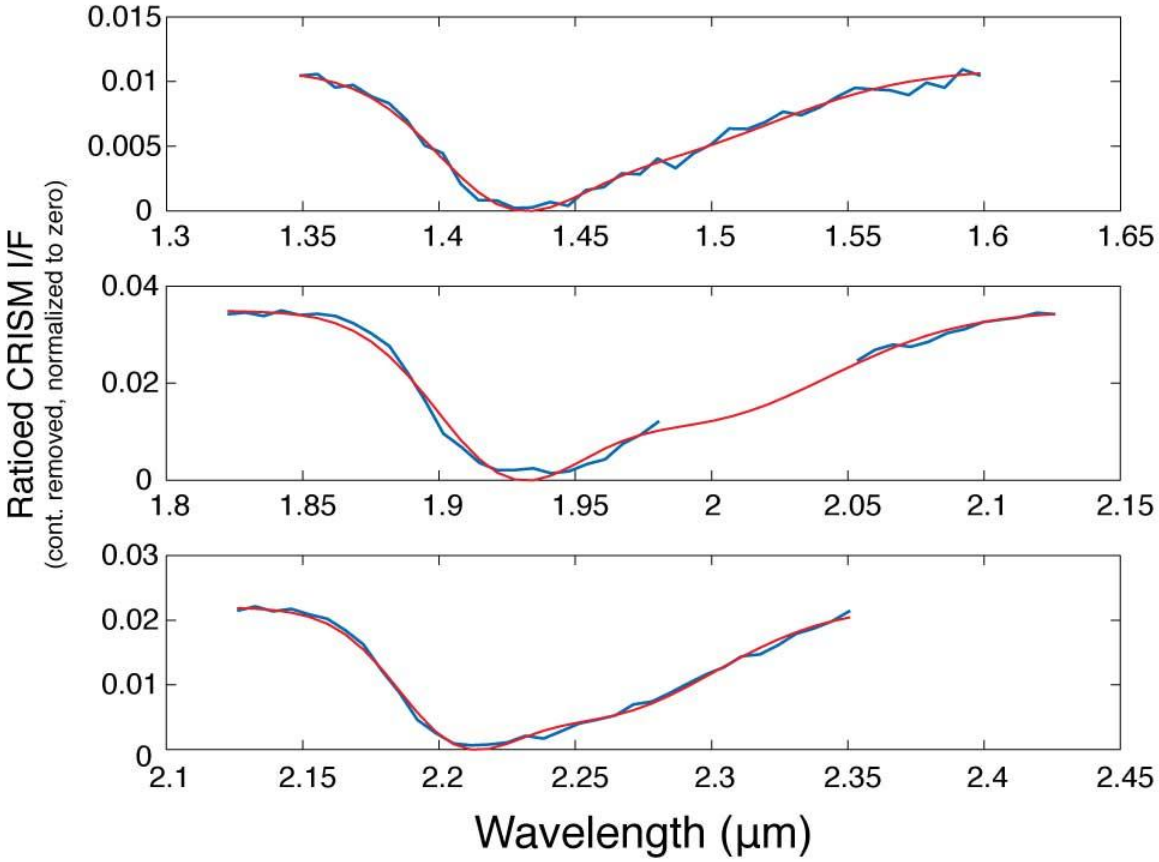

Figure 3.1 — Example of the summed-Gaussian fits for the 1.4, 1.9 and 2.2 μm features of hydrated silica. Blue curves: ratioed and continuum-removed CRISM data. Red curves: summed-Gaussian model fits.

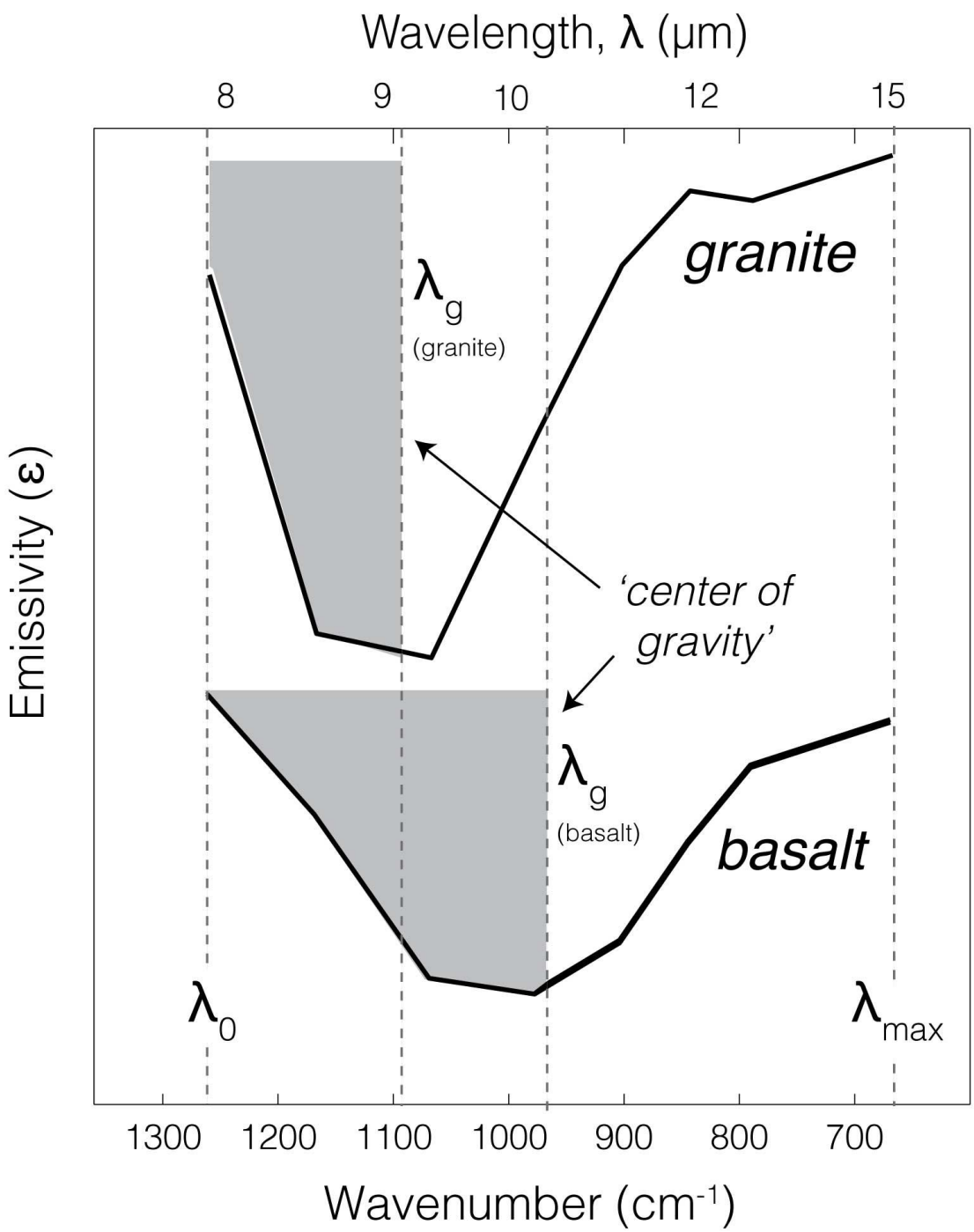

Figure 3.2 — Depiction of the wavelength of the 'center of gravity' [*Vincent and Thomson, 1972*], described in Section 3.3.1 and Equation 3.2. The 'center of gravity' wavelength is able to describe the location of the Reststrahlen band minimum in multispectral thermal data, which is correlated to the bulk SiO_2 abundance of the sample.

Chapter 4 | Global characterization of Martian hydrated silica deposits

4.1 Relative crystallinity and bulk composition of Martian hydrated silica

This section describes the findings pertaining to the two goals for the improved characterization of hydrated silica on Mars:

1. Using CRISM and the empirical crystallinity indices from *Rice et al.* [2012] to determine the relative degree of crystallinity of the hydrated silica deposits;
2. Use THEMIS to determine the SiO_2 abundance of the silica-bearing surfaces to ascertain a relative degree of alteration.

4.1.1 Determination of relative crystallinity from CRISM

All CRISM spectra collected from the sites in Table 1.1 are shown in Figure 4.1. The 'crystallinity indices', calculated using the methods described in Section 3.1.3, are shown in Figure 4.2 and listed in Table 4.1. Juventae Chasma, Nili Patera 1, Isidis Basin 1, and Terra Sirenum 2 were excluded from analysis due to weak 1.4 μm features.

Some notable omissions from these analyses are previously published accounts of hydrated silica in the Arabia Terra/Mawrth Vallis region and in the white soils of the

Gusev plains by the Spirit rover. The reasoning behind Arabia Terra's absence is described in Appendix A. The Gusev soils were found to contain silica by the mini-TES instrument [*Squyres et al.*, 2008] and confirmed to be hydrated using a diagnostic spectral slope in Pancam images [*Rice et al.*, 2010]. However, because of their limited exposure, no near-infrared spectra of these deposits have been acquired from orbit, and thus they cannot be compared with similar deposits elsewhere. Comparison between Gusev silicas and orbitally detected silicas will be discussed further in Section 4.2.3

A few things may be inferred from the near-infrared indices. First, a trend similar to the laboratory studies of *Rice et al.* [2012] is observed (Figure 1.3): a negative slope between opal-A/CT and microcrystalline quartz species (increasing 1.4 μm band minimum wavelength, lower 1.91/1.96 μm band-depth ratio) that was correlated with increasing crystallinity. This agrees with prior determinations of crystallinity from TES measurements; Western Hellas was found to contain primarily non- or paracrystalline opaline silica [*Bandfield,* 2008], and the N. Syrtis Major location contains predominantly quartz [*Bandfield et al.,* 2004]. From these results, the thermal and near-infrared spectral determinations of relative degrees of crystallinity appear to be in good agreement. Furthermore, the most crystalline silica phase yet detected on Mars in the TIR is in the N. Syrtis Major region, and this is verified by near-infrared analysis.

Second, there is a large variability of the "crystallinity indices" between different deposits globally. Though band indices cannot be used as direct indicators of silica

phase, TIR determinations of silica phase (opaline silica at Western Hellas Basin, quartz at N. Syrtis Major) may be used to provide constraints on the crystallinity for other Martian silica phases. For instance, all silica deposits with lower crystallinity indices than the Western Hellas Basin silica bearing surfaces (Figure 4.2) can be assumed to be less or equally crystalline phases. Thus, Martian silicas display a range of crystallinity from amorphous to crystalline varieties. This range of crystallinities may indicate a range of exposures to variable that increase the rate of diagenesis, including heat, water, alkalinity or some combination thereof, as discussed further in Section 4.2.1.

Finally, there is relatively little small-scale variability of the degree of crystallinity between nearby deposits. Multiple spectra collected from adjacent deposits (e.g., Toro Crater, Noctis Labyrinthus) show similar degrees of crystallinity, indicating locally homogeneous amounts of alteration, despite a more globally heterogeneous distribution.

4.1.2 SiO_2 abundance from thermal spectroscopy

THEMIS spectra were collected over all resolvable hydrated silica deposits and analyzed using the 'center of gravity' determination described in Section 3.3.1. Values are given in Table 4.1 and plotted in Figure 4.3. Surface Types 1 and 2 and laboratory spectra of many rock-forming minerals were also plotted for comparison.

First, the 'center of gravity' determinations appear to match well among compositions that are known to be similar. Martian TES Surface Type 1, a basaltic composition [*Bandfield et al.*, 2000a], has values close to that of laboratory basalt spectra. Similarly, Surface Type 2, determined to have an andesitic composition, and laboratory andesite have similar values as well.

In most cases, it appears that the hydrated silica deposits are not markedly different from the composition of Surface Type 2, a composition that has been calculated to contain 25% amorphous components [*Bandfield et al.*, 2000a]. Surface Type 2 has been postulated to be a basaltic andesite [*Bandfield et al.*, 2000a] or an aqueously altered basalt [*Kraft et al.*, 2003], though neither mechanism requires large amounts of water to elevate their overall SiO_2 abundances [*Wyatt and McSween*, 2006]. Based on their similar SiO_2 abundances, it does not appear that many of these hydrated silica deposits reflect significant amounts of alteration.

A prominent exception to this is in Western Hellas. Here the 'center of gravity' values suggest SiO_2 abundances similar to granite, which commonly has a SiO_2 abundance of ~70 wt% [*Lyon*, 1965]. This is similar to modeled SiO_2 abundance of the Western Hellas deposits from TES that found roughly 75 wt% amorphous silica [*Bandfield*, 2008], providing a close agreement between the 'center of gravity' silica estimates and better-resolved models from TES.

There is also a weak correlation between SiO_2 abundance and relative degree of crystallinity from near-infrared band-indices (Figure 4.2). The most siliceous surfaces in Figure 4.3 — Western Hellas, Isidis Basin — are also some of the most crystalline. This trend also holds for Nili Patera, which is among the least siliceous surfaces and among the least crystalline. However, this trend does not hold for many of the intermediate cases, suggesting that the SiO_2 abundance of the surface is an unreliable indicator of the silica phase.

The case of N. Syrtis Major is unique among the sites discussed here. As will be discussed in Chapter 5 and 6, the silica there does not appear to be associated with any rock unit, but instead is concentrated in mobile, dune-forming units. Furthermore, the apparent source rocks for the sediment show no detectable silica. Therefore, the bulk SiO_2 abundances do not describe the *in situ* alteration of these deposits, although the anomalously high crystallinity of these deposits is still noteworthy.

4.2 Discussion

4.2.1 Implications for alteration environment

From the analysis of the spectral characteristics of the hydrated-silica-bearing deposits in the NIR and TIR, it may also be possible to infer something about the environmental conditions that formed them. Specifically, the relative degree of crystallinity and the relative bulk content of silica to may place some constraints on the degree of alteration.

The most common pathway to produce more crystalline silica phases is through slow diagenetic transformation to more stable, crystalline species through a gradual dissolution and reprecipitation in water (Section 1.2.2). Thus, one way to produce the range in the degrees of silica crystallinity is to vary the amount of time in contact with water, thereby allowing for the reaction to progress to different degrees.

However, this diagenetic process is predicated on silica dissolution and will proceed more rapidly in systems where silica solubility is increased, of which there are many (as summarized by *Dove and Rimstidt* [1994]): increased temperature, greater pressure, higher pH, smaller grain sizes, and a lower amount of dissolved solutes in solution (e.g., NaCl). If it is assumed that one or more of these factors is influencing the increased crystallinity of the observed silica phase, it should be reflected as an increased amount of alteration of the entire deposit, as expressed by the bulk SiO_2 abundance. Many of the factors that increase silica solubility will also increase the weathering of rock-forming minerals and glasses, so it may also be expected to increase the bulk SiO_2 abundance as the rock is weathered if diagenesis is the predominant cause of increased crystallinity.

So, is this the case? From these data, there is a weak, but not insignificant, correlation between greater crystallinity and higher bulk silica. In some cases, such as Nili Patera and Terra Sirenum, the surfaces are comprised of less crystalline silica within a low-SiO_2 deposit, suggesting little alteration of the surface. Conversely, at Isidis Basin and Western Hellas, higher degrees of crystallinity are associated with higher-SiO_2 surfaces,

indicating that the deposits were subjected to a greater degree of alteration. In these types of cases, the general agreement between crystallinity and SiO_2 abundance is consistent with a diagenetic origin for the silica.

In other cases, there is a stark contrast between the degree of crystallinity and overall surface SiO_2 abundance. For example, the two deposits of Toro Crater (Toro Crater 1 and 2) are separated by ~20 km yet both have consistent higher degrees of crystallinity despite low SiO_2 abundances. In Toro Crater, the hydrated silica is found associated with prehnite [*Marzo et al.,* 2010], a high-temperature mineral that forms in deep hydrothermal systems. In hydrothermal systems, the conversion from opal-A to opal-CT may occur in as short as 1 day at ~150°C in laboratory experiments [*Kastner et al.,* 1977]. If the hydrothermal alteration of the country rock was rapid, the precipitation and diagenesis of opal-A to more crystalline phases may occur quickly enough to suppress large-scale alteration of the rock.

4.2.2 Spatial relationships between thermal and near-infrared silica detections

In addition to analyzing the spectral information of both thermal and near-infrared spectroscopy in isolation, it is also useful to combine them and infer spatial distributions of the silica detected from the two different wavelength ranges. Here, specific examples representing the different types of silica concentration-crystallinity relationships will be explored further: N. Syrtis Major (high crystallinity), Nili Patera (low crystallinity, low SiO_2 abundance), and Toro Crater (moderate-to-high crystallinity, low SiO_2 abundance).

To examine the spatial distributions of the silica detections from thermal and near-infrared datasets, spectral mixture analysis of atmospherically corrected THEMIS data is performed using Surface Type 1, opal, and dust as spectral endmembers. Though these are unlikely to be the only mineral contributors to the scene, they provide a qualitative description of the distribution of silica within the THEMIS scene and allow for comparison with spectral index maps with CRISM.

N. Syrtis Major. Examining the spatial distribution of high-silica phases (THEMIS) and hydrated silica (CRISM) on the floor of a crater near Antoniadi Crater (Figure 4.4) shows that there is an excellent agreement between the two datasets. In both images, the highest concentrations of silica are found in the lowest points of the crater floor and ringing the central peak. The origin and distribution of silica here and nearby will be discussed further in Chapter 5 and Chapter 6.

Nili Patera. In Nili Patera, hydrated silica detections are located within and near a lobe of a high-silica lava flow [*Christensen et al.,* 2005]. This silica-rich primary igneous composition contributes to a more spatially extensive high-silica signal in THEMIS data than is seen with CRISM. In contrast, elevated hydrated silica detections with CRISM are only found in very isolated spots on and near the Si-rich lobe. These deposits have been previously interpreted as small hydrothermal mounds within the larger igneous surfaces within the caldera [*Skok et al.,* 2010; *Amador and Bandfield*, 2011]. Here it is also apparent that not all hydrated silica detections are associated with elevated silica

with THEMIS, especially evident near the proposed volcanic vent (Figure 4.5A). The low degree of crystallinity and SiO_2 abundance is consistent with prior models of short-lived fumarolic activity in small vents associated with volcanism to account for silica formation [*Skok et al.,* 2010].

Toro Crater. Toro Crater contains hydrated silica with deposits that exhibit low concentrations of silica, but relatively high degrees of crystallinity. The low SiO_2 abundance is evident in Figure 4.6A, where there are no detectable high-silica components within Toro Crater, with all silica in Toro Crater below the level of detectability of THEMIS. Despite the low concentrations, hydrated silica is still apparent in CRISM data (Figure 4.6D), found in deposits in the central peak and western portions of the crater. As mentioned previously, the presence of prehnite in nearby deposits suggests formation at depth and at elevated temperatures (200–350°C) [*Schiffman and Day,* 1999] that is sufficient to diagenetically transform to opal-CT in short timescales (~1 day; *Kastner et al.* 1977) without significant weathering of the deposits.

4.2.3 Comparison of orbitally detected and "Home Plate" silica

The only *in situ* identification of hydrated silica on Mars was made by the Spirit Rover at "Home Plate" in the Gusev Crater plains [*Squyres et al.,* 2008; *Ruff et al.,* 2011]. Because the rover measurements allow for a greater level of detail into the origin and formation environment for the silica, it would be useful to compare these observations with those

at “Home Plate” to determine how broadly applicable this type of silica is, and if the Gusev-type silica formation is a good analog for other sites on Mars.

“Home Plate” silica has many distinct characteristics that allow for direct comparison with other types of Martian hydrated silica. It is found in very high concentrations (~65–92 wt%) within friable nodules and in isolated light-toned soils. Despite their abundance, their limited exposures and burial by basaltic sands makes them invisible from orbit [*Arvidson et al.,* 2008]. Analysis with mini-TES instrument has suggested that the silica phase is mostly opal-A, and the microscopic imager revealed a spongy and porous microtexture that has eroded to form sediment with grain sizes ranging from <30 μm to 1 cm [*Ruff et al.,* 2011]. Additionally, silica deposits were found to be associated with carbonates, suggesting that the silica precipitated from an alkaline solution as a primary sinter and subject to little post-depositional aqueous alteration.

An inherent problem in comparing “Home Plate” silica with other orbital detections is that “Home Plate” showed no detectable silica prior to landing. Therefore, if one of the sites of this study does not exhibit similar characteristics as “Home Plate,” this does not preclude a similar formation mechanism due to the limitations of the ability to make detailed observations from orbit. However, there are some locations that appear to share some properties with “Home Plate” silica, possibly suggesting some commonalities in formational style.

The site that is most akin to the Gusev Crater deposits is in Western Hellas Basin. There, concentrations of silica from orbit (~75%; *Bandfield*, 2008) are within the range of the samples at "Home Plate" (~65–92%) and the silica phase is similarly noncrystalline. Furthermore, the silica in Western Hellas appears to be friable and was transported downslope by wind, implying a similar strength as the Gusev silica.

Another family of sites that exhibit similarities with Gusev Crater silica are located in the region just north of Syrtis Major: Toro Crater, Isidis Basin, and N. Syrtis Major/Antoniadi Crater. The Isidis Basin and Toro Crater sites have similarly noncrystalline silica phases, and the N. Syrtis Major and Toro Crater deposits are associated with mobile, aeolian sediments that indicate a friable deposit. As with the Western Hellas site, this family of sites appears to have formed from a similar alkaline origin as "Home Plate" silicas.

Other sites appear to represent a different style of silica formation. Silica deposits adjacent to Valles Marineris (Juventae Chasma, Melas Chasma, Noctis Labyrinthus) are all found in conjunction or mixed with sulfates: jarosite at Juventae and Melas Chasma [*Milliken et al.*, 2008] and a variety of polyhydrated and monohydrated sulfates at Noctis Labyrinthus [*Weitz et al.*, 2011]. Furthermore, Terra Sirenum silica is found next to kaolinite in a mound to the south of Columbus Crater [*Wray et al.*, 2011]. At all of these sites, the association with sulfates and kaolinite implies acidic conditions at the time of silica precipitation, and is most consistent with the acid-leaching model for the precipitation like that proposed by *Squyres et al.* [2008] to have formed the Gusev silica,

though this formation method at Gusev Crater is refuted [*Ruff et al.,* 2011]. If the Valles Marineris and Terra Sirenum deposits formed under acidic formation conditions, this implies a different regime of alteration than hydrated silica deposits associated with alkaline systems elsewhere.

4.2.4 Synthesis of global Martian silica study

From this analysis of Martian silicas, there are four main conclusions pertaining to the nature of hydrated silica on Mars:

1. Silica crystallinities span from noncrystalline to crystalline phases. Furthermore, they do not exhibit uniformly low degrees of crystallinity as may be expected for the otherwise underdeveloped soils of Mars [*Tosca and Knoll,* 2009].
2. Despite large-scale heterogeneity between silica deposits, local exposures displayed homogeneous degrees of crystallinity and bulk SiO_2 abundance, suggesting locally consistent alteration and formation conditions.
3. The bulk SiO_2 abundance of hydrated silica deposits ranges from concentrations similar to Surface Type 2 (~58 % SiO_2; *Hamilton et al.,* 2001) up to granite-like (~70 wt% silica).
4. Formation environments for global Martian silica are diverse and do not imply broad-scale similarities in silica formation. However, many sites show similarities with the well-studied Gusev Crater silica

deposits, such as alkaline formation conditions, high SiO_2 abundances, and friable sinter-like deposits.

Tables for Chapter 4

Table 4.1 — Calculated parameters for the amount of silica and degree of crystallinity. The 1.91/1.96 μm ratio is negatively correlated with increased crystallinity; the 1.4 μmband minimum location is positively correlated [*Rice et al.*, 2012]. The 'center of gravity' wavelength is negatively correlated with SiO_2 abundance [*Vincent and Thomson*, 1972]. Values are omitted due to weak 1.4 μm values (for NIR indices) and unresolvably small areas (for the 'Centers of Gravity'). Values are plotted in Figure 4.2 and Figure 4.3.

Location Name	*1.91/1.96 μm band depth ratio*	*~ 1.4 um band minimum location (μm)*	*"Center of gravity" wavelength (μm)*
Isidis Basin 2	1.125	1.415	9.87
Juventae Chasma	—	—	9.96
Melas Chasma	1.340	1.388	—
N. Syrtis Major	0.806	1.432	9.56
Nili Patera 2	1.149	1.391	9.86
Noctis Labyrinthus 1	1.425	1.403	—
Noctis Labyrinthus 2	1.423	1.411	—
Terra Sirenum 1	1.348	1.402	9.68
Terra Sirenum 2	—	—	9.77
Toro Crater 1	1.171	1.430	—
Toro Crater 2	1.232	1.418	9.94
Western Hellas	1.064	1.415	9.27

Figures for Chapter 4

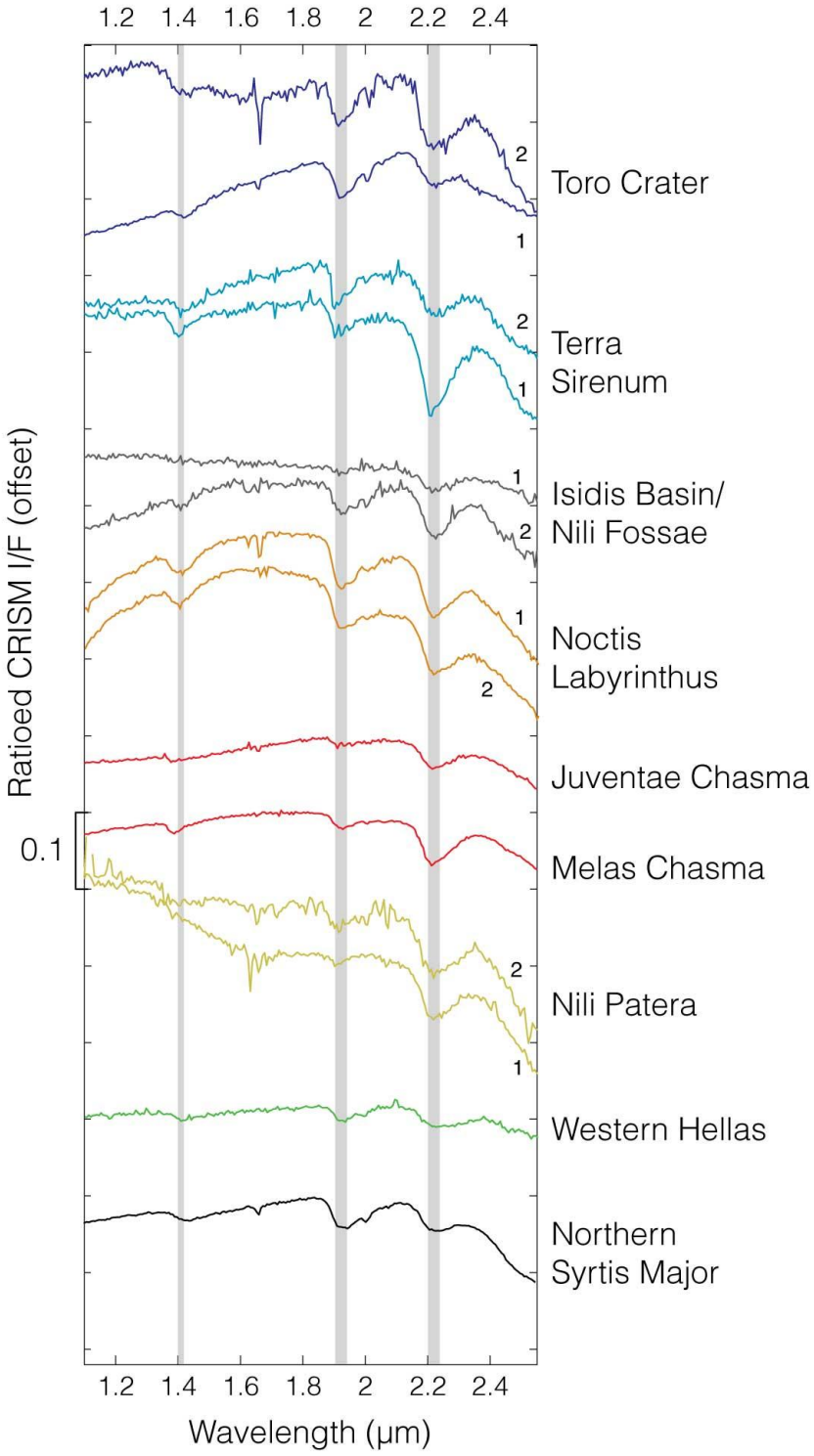

Figure 4.1 — CRISM spectra for all resolvable deposits of hydrated silica listed in Table 1.1.

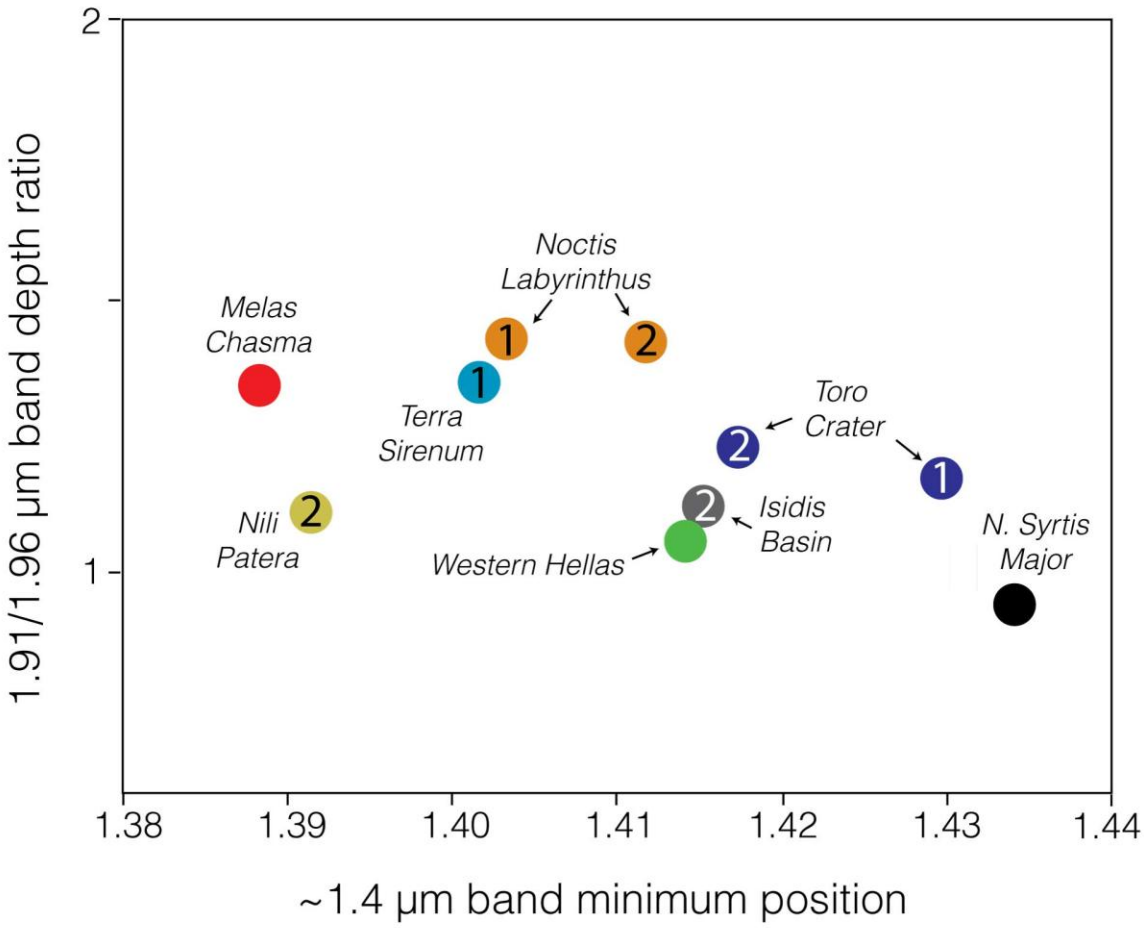

Figure 4.2 — Parameters describing the relative degree of crystallinity of Martian silica. Terrestrial silica increases in crystallinity from lower right to upper left in this same plot, suggesting that N. Syrtis Major is the most crystalline of these deposits. N. Syrtis Major has been independently determined to be the only detection of crystalline quartz, consistent with these findings.

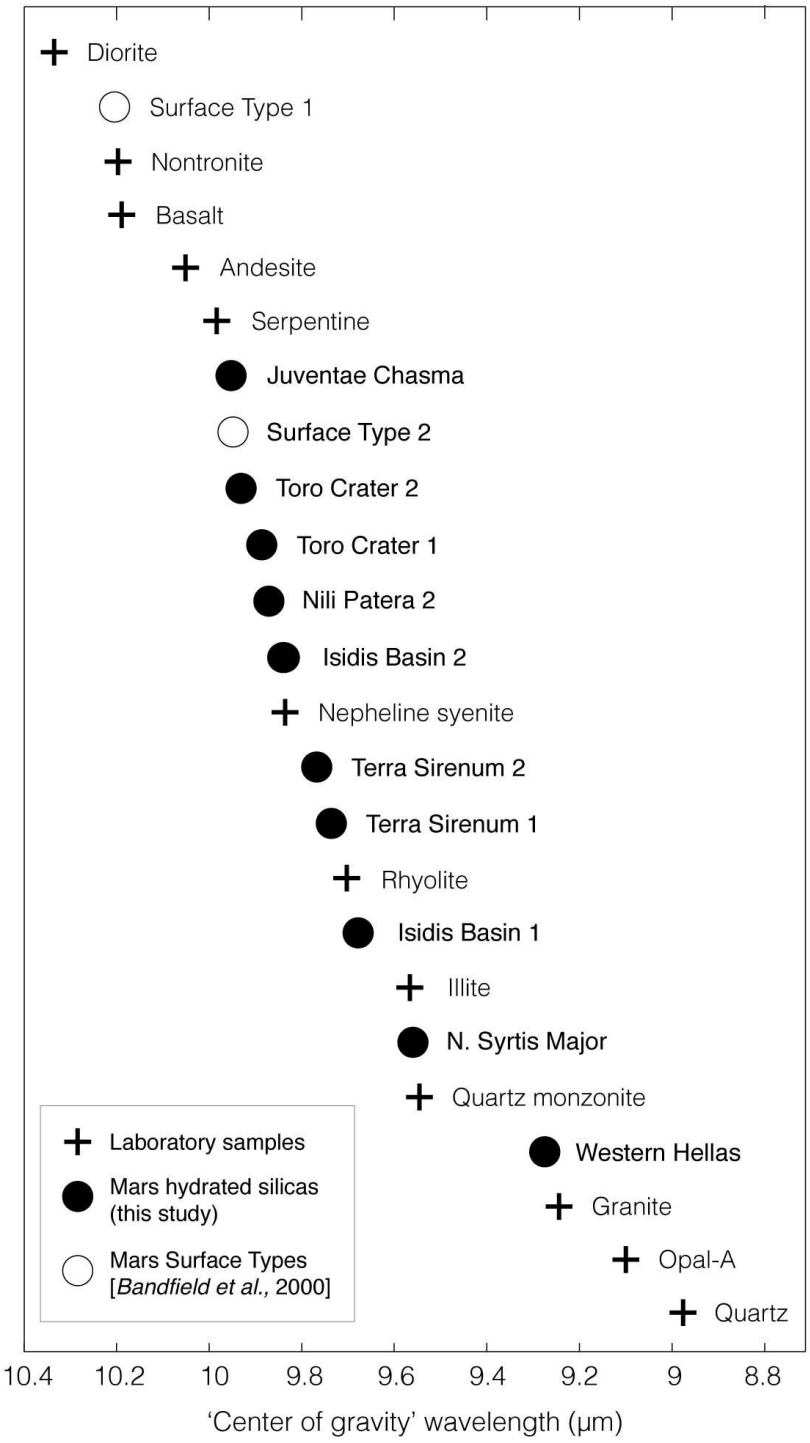

Figure 4.3 — 'Center of gravity' wavelengths for Martian hydrated silica deposits, compared with Mars Surface Types 1 and 2 and several lab samples of common rock-forming minerals. The 'center of gravity' of a thermal spectrum is illustrated in Figure 3.2 and is a measure of the bulk SiO_2 abundance of the surface. Other minerals (illite, serpentine, nontronite) also have TIR absorptions in this region and are capable of contributing to this signal, but have not been detected with NIR spectroscopy and are unlikely to be affecting these spectra.

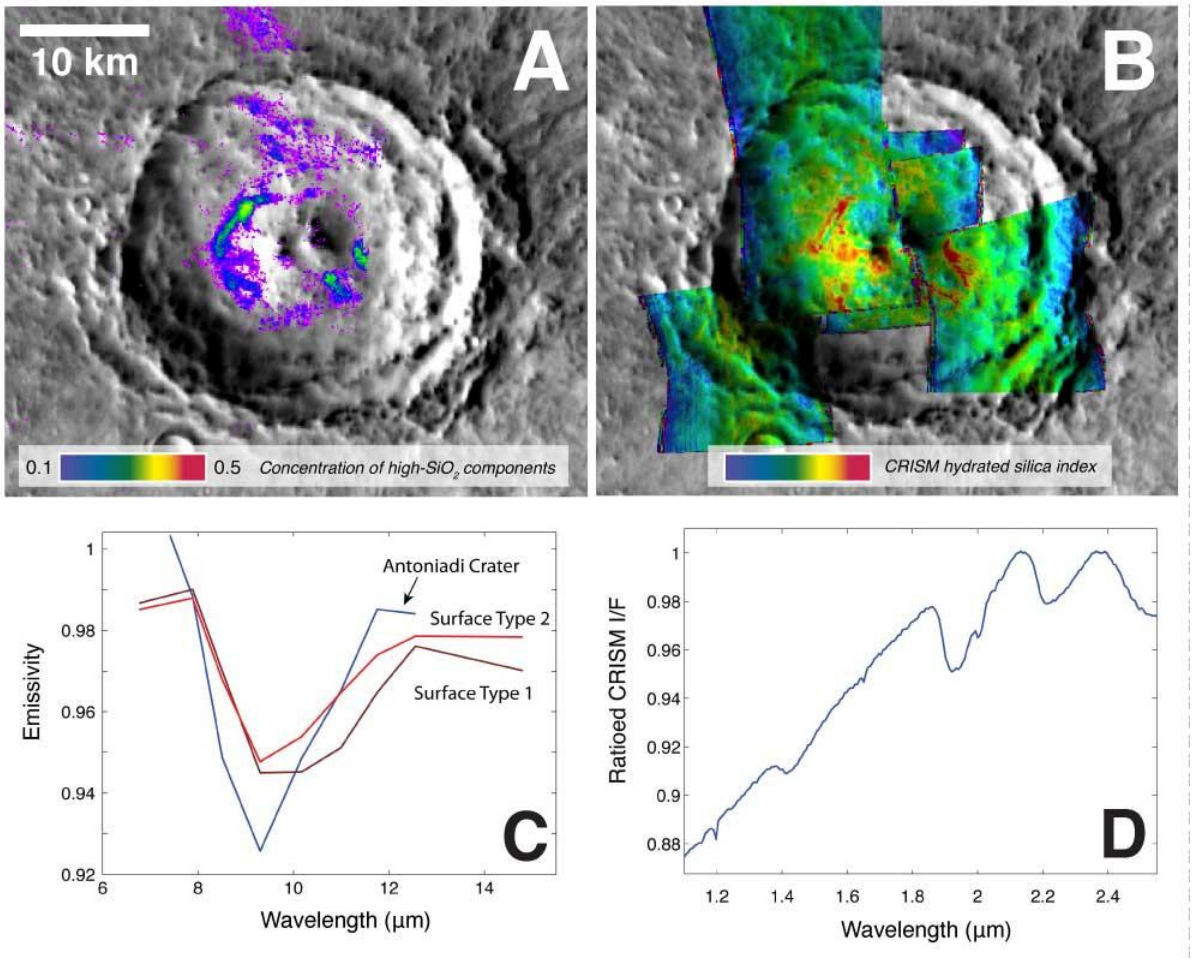

Figure 4.4 — Distribution of silica phases In crater in N. Syrtis Major. A) High-silica phases determined through deconvolution of THEMIS data. B) Hydrated silica index maps overlain on THEMIS mosaic. C) THEMIS spectrum of hydrated silica unit compared with Surface Types 1 and 2. D) CRISM spectrum of hydrated silica.

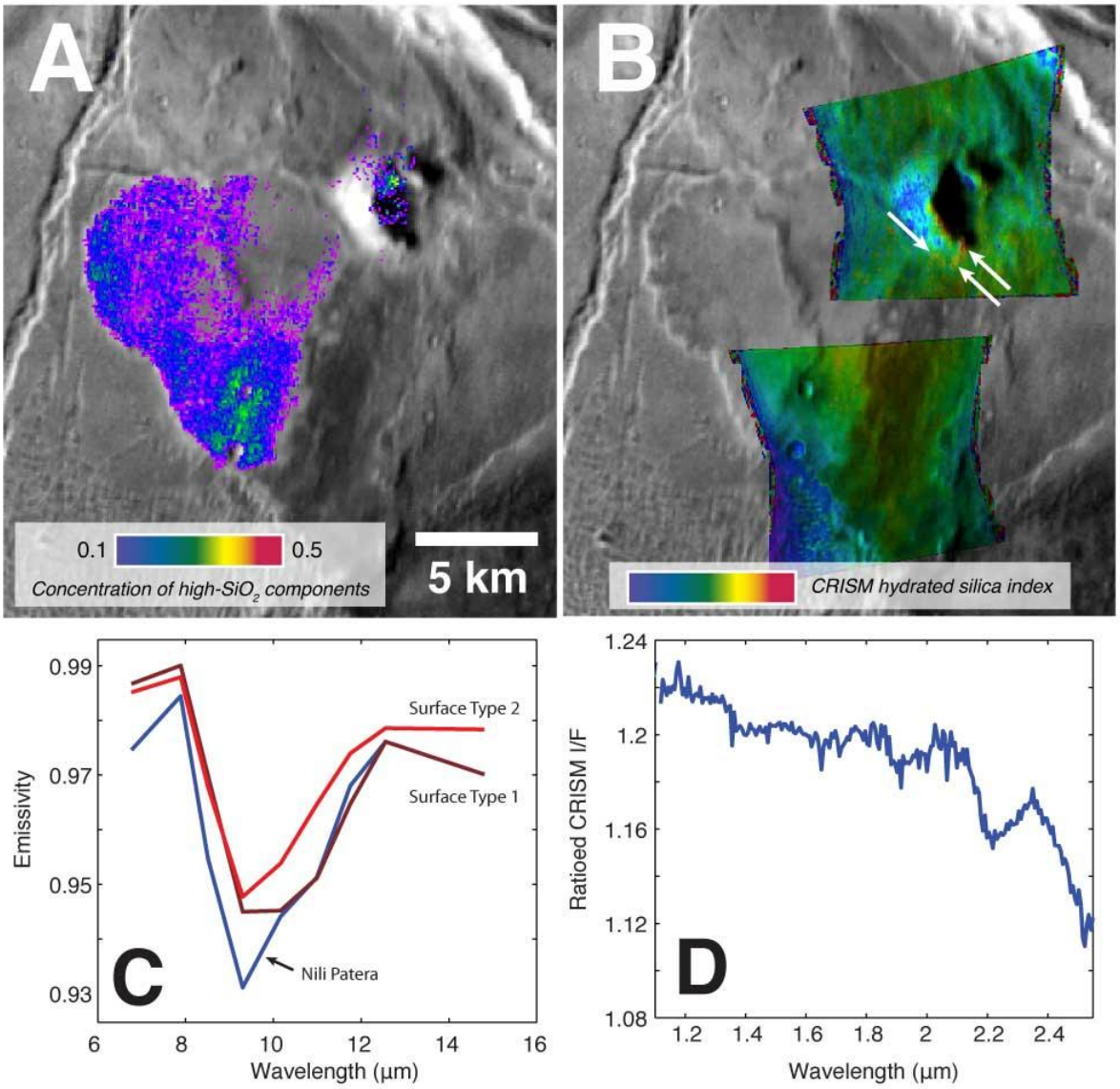

Figure 4.5 — Distribution of silica phases In crater in Nili Patera. A) High-silica phases from THEMIS data. B) Hydrated silica index maps overlain on THEMIS mosaic. White arrows indicate small (~1-2 pixel) locations of elevated hydrated silica deposits C) THEMIS spectrum of hydrated silica unit compared with Surface Types 1 and 2. D) CRISM spectrum of hydrated silica.

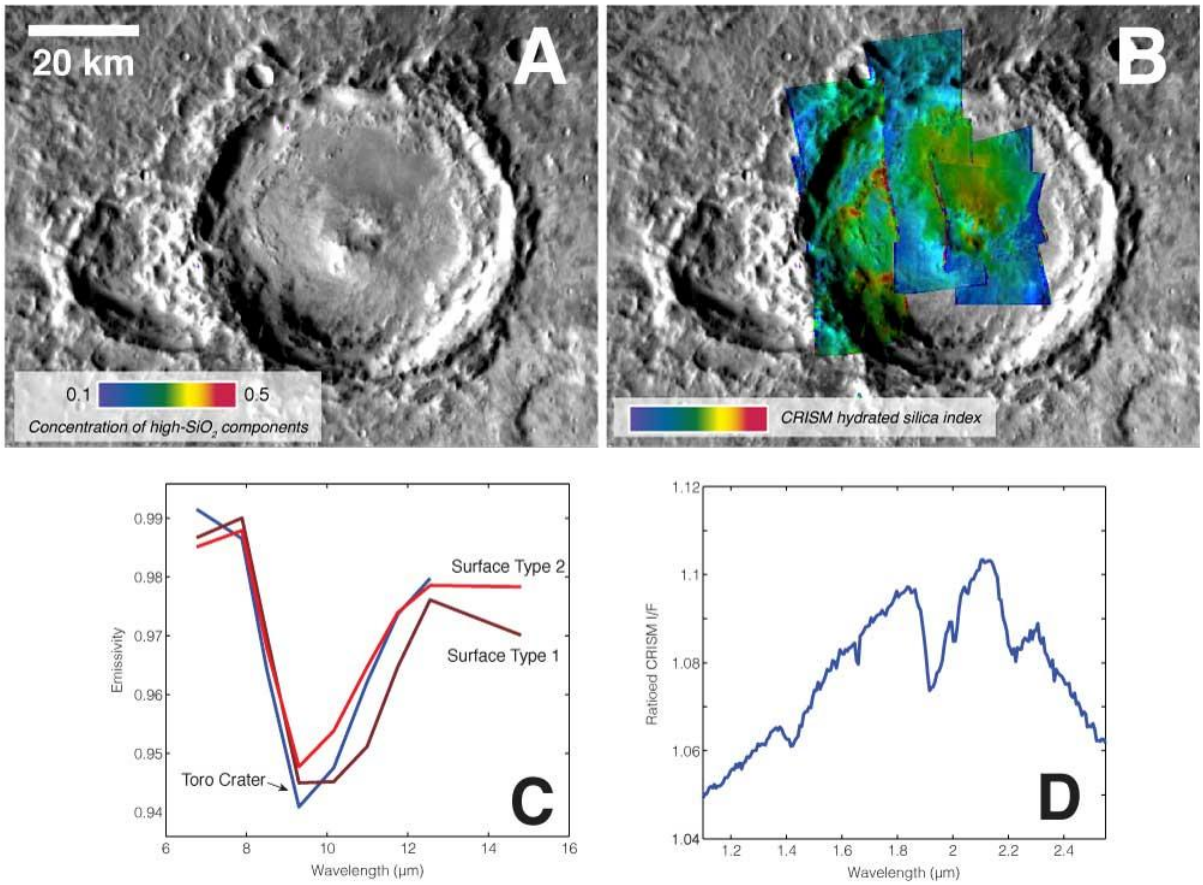

Figure 4.6 — Distribution of silica phases In crater in Toro Crater. A) High-silica phases from THEMIS data. B) Hydrated silica index maps overlain on THEMIS mosaic. C) THEMIS spectrum of hydrated silica unit compared with Surface Types 1 and 2. D) CRISM spectrum of hydrated silica.

Chapter 5 | Geology and spectroscopy of the Antoniadi Crater region

For the second portion of this dissertation, I more intensively study one location of hydrated silica, the N. Syrtis Major deposit near Antoniadi Crater (hereafter referred to as the Antoniadi Crater region). Here, the Antoniadi Crater region has been divided into four provinces that contain all exposures of quartzofeldspathic material (Figure 5.1): Large Elliptical Depression, Small Elliptical Depression, Rim Crater Ejecta, and Syrtis Craters. Each province has surfaces with distinct mineralogic compositions and geomorphic features, and contributes to the interpretation of the geologic and aqueous history of the region. Geologic and spectral observations of each one is described in detail, followed by a synthesis of pertinent information.

5.1 Large Elliptical Depression

5.1.1 Geologic context

The Large Elliptical Depression province is located on the floor of southeastern Antoniadi Crater, ~65 km from the crater rim (Figure 5.2). The depression is 12 × 3 km and lies ~50 m below the surrounding terrain, trending northeast-southwest. It contains two large hills in the southwest (50 m and 350 m above the depression floor, as determined by MOLA [*Smith et al.*, 2001b]), which are dissected along their eastern flanks and show prominent bench-and-cliff morphology with many meter-scale sub-

horizontal layers (Figure 5.3A). On the floor of the depression, large portions are covered by breccias with many large (10 – 1000 m) clasts (Figure 5.4A). Some brecciated units appear mottled and aqua-colored in HiRISE IRB color images (Figure 5.4B), corresponding to greater reflectivity between 400 and 850 nm (projected as green and blue in Figure 5.4) than between 800 and 1000 nm (red) compared with the surrounding terrain. Greater absorptions between 800–1000 nm than 400–850 nm are commonly exhibited by ferrous minerals (e.g. olivine, pyroxene), which exhibit crystal field effects near 1000 nm, but lack the charge transfer at 400–600 nm exhibited by ferric minerals [*Hunt*, 1977].

Lighter-toned sediment appears to originate from nearby breccia units and accumulate in local basins, and forms ripple-forming deposits in the lowest parts of the basin, though not in all lighter-toned deposits (Figure 5.4). The most extensive example of these light-toned deposits is located along the northwestern rim, which is the deepest area in the depression (97 m above datum). The Large Elliptical Depression is surrounded, but not buried, by Late Noachian–Early Hesperian flood basalts that have resurfaced most of the crater floor, sourced from both Syrtis Major and proximal sources within Antoniadi Crater [*Hiesinger and Head,* 2004]. Because the Large Depression pre-dates these basalts, then the units that have a stratigraphic relationship with the flood basalts (i.e., the brecciated units, and layered knobs beneath the brecciated units) must have formed before the Early Hesperian. The ripple-forming units cover the brecciated units and likely formed more recently.

There are spatial correlations between the Large Depression geomorphic units and their thermal-inertia values, calculated using nighttime THEMIS IR data. The layered knobs and breccia units have the highest thermal-inertia values in the depression: 350–500 J m^{-2} K^{-1} $s^{-1/2}$; the unit labeled 'brecciated unit' in Figure 5.3B has a calculated range of TI values between 350 and 450 J m^{-2} K^{-1} $s^{-1/2}$. These values indicate that the surface is mildly indurated, or comprised of a mixture of unconsolidated sediment and competent rock at subpixel scales (surfaces dominated by high-strength rocks would have thermal-inertia values of >~1000 J m^{-2} K^{-1} $s^{-1/2}$). These values are too low for an outcrop of competent breccia, and it does not appear that a low-inertia dust or sediment mantle is cloaking the underlying breccia because individual breccia blocks are clearly visible in high-resolution images. Instead, the breccias themselves are likely to be poorly lithified and may be an agglomeration of weakly indurated blocks. Elsewhere, the silica-bearing mobile sediments have low thermal-inertia values of 200–250 J m^{-2} K^{-1} $s^{-1/2}$, in accordance with the interpretation of these materials as wind-blown fine particulate sediments. For comparison, the aeolian bedforms at both MER landing sites were found to have thermal-inertia values of ~200 J m^{-2} K^{-1} $s^{-1/2}$, which is consistent with a surface comprised of fine sand and a modeled mean particle size of 160 μm [*Fergason et al.,* 2006b]. Additionally, the very silica-rich soils unearthed at the Spirit landing site have a heterogenous distribution of grain sizes but are similarly dominated by sand-sized grains [*Ruff et al.,* 2011], although thermal inertia values have not been calculated there.

5.1.2 Spectral identifications

Thermal spectral analysis shows that the predominant regional surface composition near the depression is basaltic, dominated by the presence of plagioclase and pyroxene. Additionally, most of the depression floor, walls and knobs are consistent with a surface of basaltic composition based on interpretation of THEMIS spectral data. There are also isolated plagioclase- and quartz-bearing mineral exposures in units previously described and interpreted as granitoid/quartzofeldspathic [*Bandfield et al.* 2004a; *Bandfield,* 2006]. The specific identification of crystalline quartz has been positively identified with TES by observing a diagnostic absorption feature at 20 μm that uniquely matches the position and shape of quartz, instead of the more poorly crystalline silica polymorphs (opal-A and opal-CT) [*Bandfield et al.,* 2004a]. The quartz-bearing surfaces are spatially coincident with light-toned deposits along the northwestern rim of the depression and within isolated locations on the depression floor.

In addition to thermal spectroscopy, the province was also analyzed in the near-infrared with CRISM. The spectra display clear absorptions at 1.4 and 1.9 μm, and a broad 2.21 μm feature associated with deposits on the floor of the depression. These features are most consistent with the presence of hydrated silica, such as opal (Figure 5.3C). Previous work on Martian hydrated silica have noted that the location of the 1.4 μm band will shift to 1.38–1.39 μm as water is lost under desiccating conditions

[*Milliken et al.,* 2008] or that the location of the 1.4 μm band will shift to longer wavelengths for more crystalline phases [*Rice et al,* 2012]. Because the band centers of the 1.4 μm feature are located at ~1.42–1.43 μm, this would suggest that either this silica is more hydrated or crystalline than elsewhere on the planet. In this spectrum, and many other spectra collected for this study, there is also an absorption at 2 μm that is attributed to an incomplete removal of atmospheric CO_2 during the correction; because of this, this feature is ignored in all of the analyzed spectra. There is also a separate mineral phase detected in small exposures (5 –10 pixels) within the layered knobs in the southwest, with absorption features at 1.4 and 1.9 μm, and additional features at 2.31 and 2.39 μm, consistent with a Mg-bearing clay, possibly saponite (Figure 5.3D). The phyllosilicate exposures are not resolvable with visible imagery, because there is no HiRISE coverage over the layered knobs. CTX images are available over the knobs, but do not offer sufficient resolution to resolve individual exposures.

The CRISM detections of hydrated silica have identical distributions as the plagioclase and quartz-bearing surfaces that were identified by TES–THEMIS [*Bandfield,* 2006] (Figure 5.5). The coincident quartz and hydrated silica-bearing exposures (hereafter referred to as 'high-silica deposits') are found concentrated in the lowest points of the depression along the northwestern rim. The sources of high-silica deposits are not obvious and not discrete, with no source rock that has a strong concentration of high-silica materials in CRISM or THEMIS/TES.

5.2 Small Elliptical Depression

5.2.1 Geologic context

Ten km to the west of the Large Elliptical Depression exposures there is a 2-km-wide elliptical depression, also on the floor of Antoniadi Crater (Figure 5.6). The depression is ~15 m deep, considerably shallower than the Large Depression. As with the Large Depression, the Small Elliptical Depression is surrounded on all sides by the flood basalts that have resurfaced the floor of Antoniadi Crater. A large portion of the floor is covered by variably thick sediments in the broad western portion of the depression, and the sediments can accumulate in basins to form ripples.

The thermal inertia of the Small Elliptical Depression is relatively low everywhere, reaching its highest values of 300–370 J m^{-2} K^{-1} $s^{-1/2}$ near the central peak. As with the Large Depression, there are no thermal-inertia values suggestive of competent rock, and the entire surface has a thermal inertia indicative of a poorly indurated material. Within the thickest concentrations of light-toned sediment along the western edge of the depression, there are thermal-inertia values consistent with its apparent aeolian morphology: 200–250 J m^{-2} K^{-1} $s^{-1/2}$.

5.2.2 Spectral identifications

Data from TES-THEMIS show that the floor of Small Elliptical Depression is composed of predominantly quartzofeldspathic material (Figure 5.5). This pattern is similar to the Large Depression exposures, and the quartz-rich detections occupy a larger proportion of the surface, and are correlated with thicker and more continuous deposits of light-toned sediments. The depression walls and surrounding plains appear to be basaltic based on THEMIS data.

There are also detections of hydrated silica within the Small Depression using CRISM observations (Figure 5.6). As with the Large Elliptical Depression exposures, the hydrated silica is not tied to an obvious source rock, but instead found within wind-blown, light-toned sediments. The hydrated silica detections of CRISM are also spatially coincident with quartzofeldspathic materials identified using TES and THEMIS data (Figure 5.5). The more prominent hydrated silica spectral features are found within the continuous light-toned mobile sediments. The silica-rich sediments are consistently adjacent to exposures of the mottled aqua unit (Figure 5.7C), despite the absence of detectable hydrated silica in the aqua unit. Otherwise, there are no detections of phyllosilicates or other hydrated minerals besides hydrated silica within the Small Elliptical Depression.

5.3 Rim Crater Ejecta

5.3.1 Geologic context

The next region to be investigated is highly fractured terrain that lies within the proximal ejecta blanket of a 70 km impact crater found on the rim of Antoniadi Crater (this crater is referred to in this study as 'Rim Crater'). The Rim Crater ejecta have been highly modified since impact, both by the coarse-scale dissection, possibly by faulting or aeolian processes, and by extensive burial from Syrtis Major lavas that have also buried the Rim Crater floor. Thus, the exposed ejecta here are restricted to within ~15 km of the crater rim (Figure 5.8). Fine-scale geologic structure is rare within this region and limited to small isolated exposures of breccia blocks (Figure 5.9A) and mesas topped with a heavily pitted surface (Figure 5.9B). There are also local accumulations of light-toned sediment in topographic lows. Otherwise, the surface appears heavily disrupted as a result of the process of ejecta emplacement.

The thermal inertias within the Rim Crater Ejecta province show patterns similar to those in the Large and Small Depressions. The regions with visible breccia blocks and boulders in HiRISE have moderate thermal-inertia values relative to other surfaces in the scene (e.g. 310–360 J m^{-2} K^{-1} $s^{-1/2}$for brecciated unit in Figure 5.9A). The light-toned sediments possess similar thermal inertias as in the Large and Small Depressions: 200–250 J m^{-2} K^{-1} $s^{-1/2}$.

5.3.2 Spectral identifications

The spectral observations of Rim Crater and its ejecta are similar to those within the Large Elliptical Depression. The floor and ejecta of Rim Crater are predominantly basaltic, with limited exposures of silica- and phyllosilicate-rich deposits identified in CRISM data. The silica-rich deposits are associated with sediments found in the lowest areas, with no clear or discrete sediment source. There are only two HiRISE images that cover these exposures, precluding thorough description of rock units and determination of a detailed association between source and sediments. However, in one of the available HiRISE images, the phyllosilicates are found in limited exposures, spatially correlated with surfaces with a large number of breccia clasts (Figure 5.9A,C). These phyllosilicates have an absorption at 2.3 μm, consistent with a smectite such as saponite, but the asymmetric drop-off at long wavelengths may be more consistent with a mixed-layer chlorite/smectite clay [*Milliken et al.,* 2010] or vermiculite [*Noe Dobrea et al.,* 2010].

5.4 Syrtis Craters

5.4.1 Geologic context

To the southeast of Antoniadi Crater, two ~30 km diameter craters located on the distal northern flanks of Syrtis Major were examined (Figure 5.10). The ejecta of the two craters are emplaced on top of Syrtis Major lava flows, formed after the cessation of Syrtis Major volcanism (Late Noachian–Early Hesperian; *Hiesinger and Head*, 2004).

The two craters have a complex shape, with slumped terraces along their crater walls and pronounced central peaks. Portions of the central peaks are dissected and exhibit large-scale layering. The crater walls appear massive and blocky, with no apparent layering, and the central peaks and surrounding annular troughs of both craters contain apparent mega-breccia blocks, which may have formed as a result of this impact event or as a pre-existing breccia exposed by this impact. In both craters, the annular troughs surrounding the central peaks are commonly filled with light-toned sediments that form ripples on the crater floor. Although the source of the sediment is not obvious, many light-toned streaks are observed on the crater walls and peaks (Figure 5.11D,E; Figure 5.13C,D), and grade into dunes further onto the floor of the crater (Figure 5.11D; 13C).

Thermal-inertia values indicate regions with elevated inertia values (300–400 J m^{-2} K^{-1} $s^{-1/2}$) near the central peaks of the craters and are largely correlated with exposed mega-breccias observed in HiRISE images. These values of thermal inertia indicate that the observed surface may be poorly consolidated, or a mixture of more competent rock and unconsolidated material at sub-pixel scales. In the crater troughs, calculated thermal-inertia values are lower (100–200 J m^{-2} K^{-1} $s^{-1/2}$), in agreement with their morphologic interpretation as unconsolidated particulates. This is consistent with other exposures on the floor of Antoniadi Crater: the Large and Small Elliptical Depressions, and the Rim Crater Ejecta.

5.4.2 Spectral identifications

TES and THEMIS data were used to detect surfaces of basaltic and quartzofeldspathic composition within these craters. The predominant spectral signature of the walls and central peaks of the craters is basaltic, and similar to the plains surrounding the craters. Large portions of the base of crater floors show significant quartz- and plagioclase-rich compositions using TES spectra, which is confirmed using higher spatial resolution THEMIS data (Figure 5.5). These quartzofeldspathic deposits are only found within the craters, and not within their ejecta.

CRISM mineralogical identifications within these craters are similar to those found within the other provinces described here. Phyllosilicates are found predominantly within breccia blocks within the central peaks and the crater floors. There are many examples of large breccia blocks and fractured rocks, resolvable within CRISM scenes, containing discrete phyllosilicate signatures (Figure 5.12). Phyllosilicate detections here show strong 2.31 μm absorptions, most consistent with iron- and magnesium-bearing smectites (e.g., nontronite, saponite). Phyllosilicate-bearing exposures are not correlated with surfaces with obviously pyroxene- or olivine-rich compositions using CRISM spectral index maps, and are too small to be spatially resolvable in THEMIS. Silica-rich deposits, detected using both TES/THEMIS and CRISM data, are most commonly found in the annular troughs surrounding the central peaks of the craters, which are the local topographic minima. The silica-rich deposits are most commonly associated with light-toned deposits on the floors, which appear to be fed by aeolian transport from nearby crater walls (Figure 5.11D,E). This sediment-transport pathway

is most apparent within the southeastern crater wall of the NE crater where sediment sources and sinks are most clearly visible (Figure 5.11). HiRISE color images show that the sediment is sourced from knobs and wall units and transported downhill along streaks which divert along local topography (Figure 5.11D). On the floor of the crater, streaks become less prevalent and light-toned dunes appear and become increasingly more common at lower elevations. Along the apparent sediment pathway, the depth of the 2.21 μm band in CRISM, which indicates the presence of hydrated silica increases downslope and intensifies in areas where the sediment appears to concentrate. This progression is also visible in the SW crater, where silica detections intensify along the direction of wind as indicated by aeolian dunes and streamers (Figure 5.13). High-silica regions also generally have low pyroxene and olivine index values in CRISM data. The lack of identifiable mafic materials with CRISM is in agreement with the lack of pyroxene and olivine detected using the TIR datasets. The apparent source regions for high-silica sediments appear to be compositionally similar to the basaltic plains material in both TIR and VNIR datasets.

5.5 Summary of observations

Within the provinces described above, there are many commonalities that can be used to reveal their formation history and environment:

1) Quartz (TES/THEMIS) and hydrated silica (CRISM) are always found coincidentally.
2) Hydrated phases (hydrated silica and phyllosilicates) are found within or in close association with breccias.
3) Phyllosilicates and high-silica material are not sourced from the same rock units.
4) Phyllosilicates are identified within some, but not all, breccia blocks, and are not identified in the breccia matrix.
5) The source of high-silica material is not found within a discrete source rock or breccia blocks, with the exception of a smooth unit within a Syrtis crater wall. Instead, silica is detected within unconsolidated light-toned units, and the nearby poorly lithified rock units from where the light-toned sediment appears to originate has no detectable hydrated silica or quartz.
6) All breccias are stratigraphically beneath the Syrtis Major lavas, and therefore formed prior to the flood volcanism of the Late Noachian–Early Hesperian.

Figures for Chapter 5

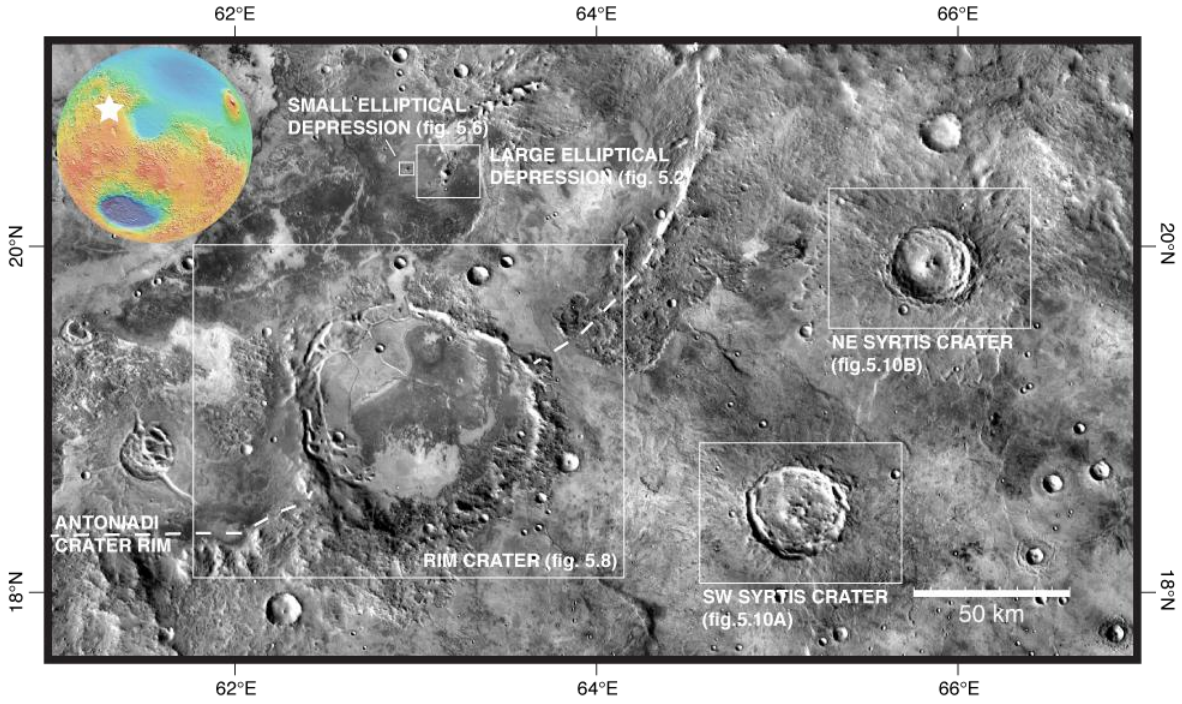

Figure 5.1 — Antoniadi Crater region study area with labeled provinces defined for this study: Small Elliptical Depression, Large Elliptical Depression, Rim Crater Syrtis Craters. For reference, the southeastern rim of Antoniadi Crater is marked in the upper left quadrant of the image.

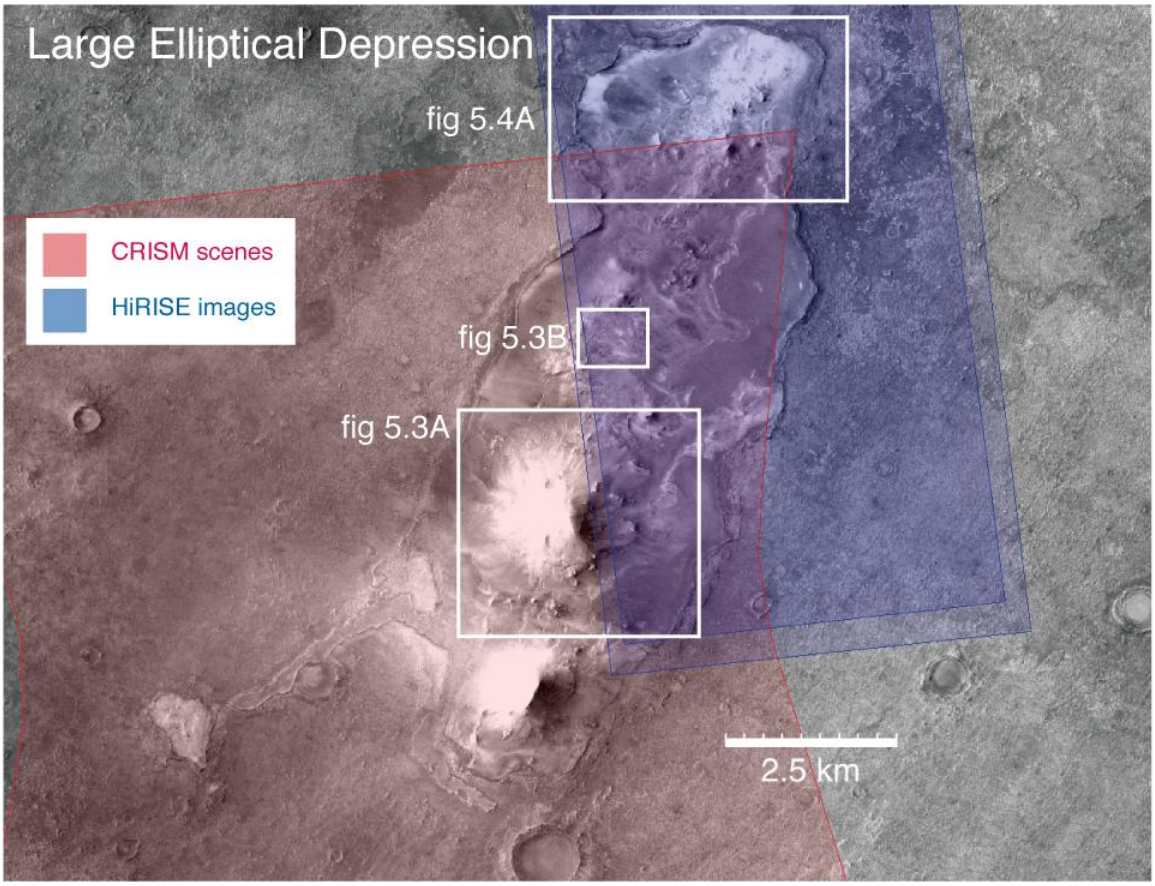

Figure 5.2 — Large Elliptical Depression province (location shown in Figure 5.1). Background CTX image: P17_007676_2019.

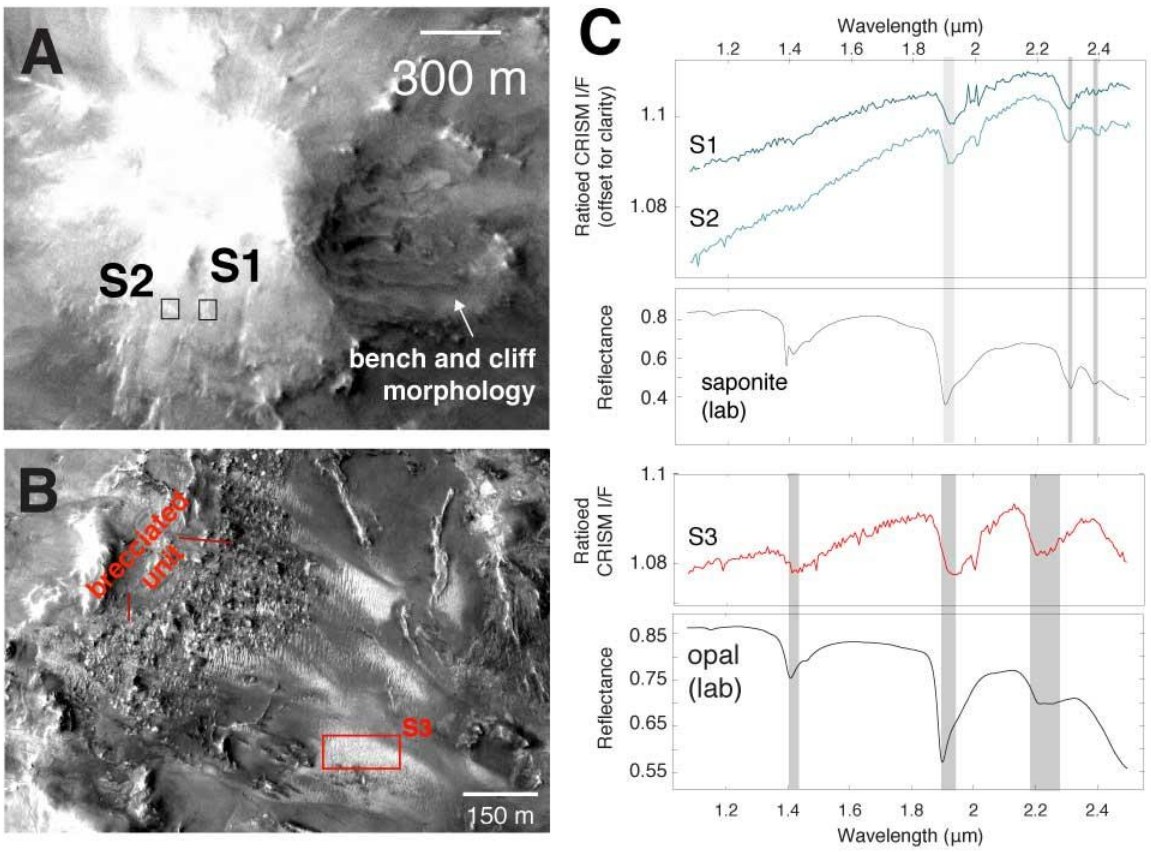

Figure 5.3 — Geomorphologic units and spectra of Large Elliptical Depression (image locations in Figure 5.2). A) Northeastern knob displaying bench-and-cliff morphology along its dissected eastern flank. Phyllosilicates, spectrally resembling saponite, are detected in limited exposures along the south side – spectra S1 and S2. B) Brecciated unit adjacent to silica-bearing sediment, which forms dunes nearby, identified using spectrum S3; C) Ratioed CRISM spectra; locations for S1–3 are shown in panels A and D; for specific location details, see Table 2. Images: A – P17_007675_2019, B – ESP_019305_2010_RED; Lab spectra: saponite — *Baldridge et al.* [2009]; opal — courtesy of E. Cloutis, University of Winnipeg.

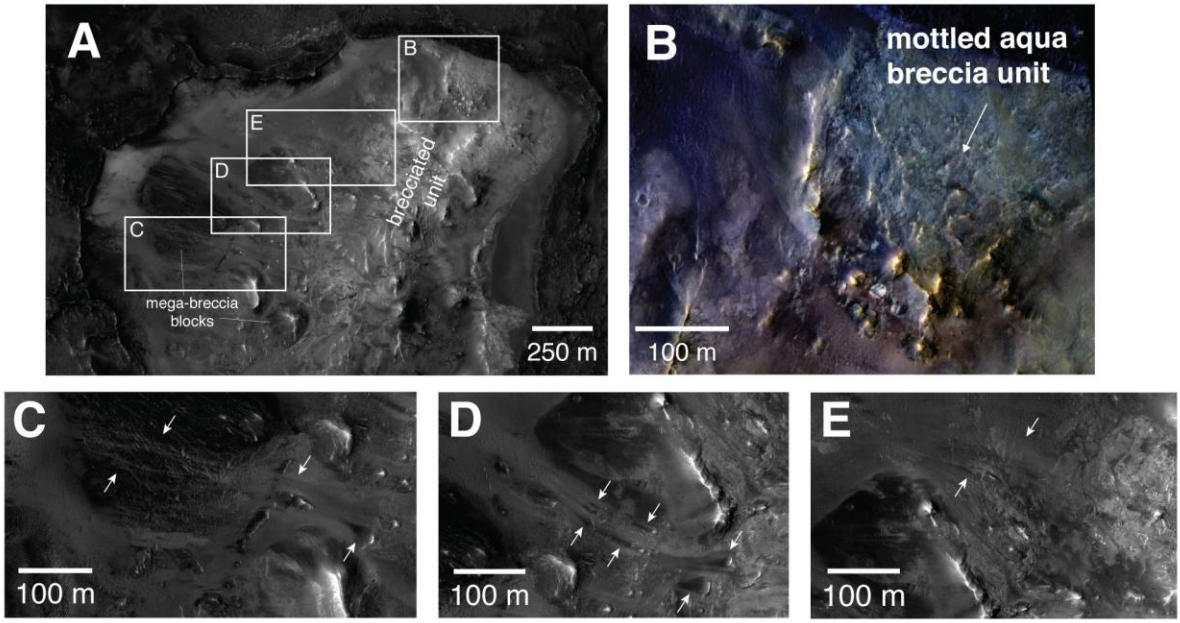

Figure 5.4 — Wind-blown light-toned sediment in the Large Elliptical Depression. Light-toned material appears to be emerging from units on the eastern side of the depression, which are brecciated (Panel B). Sediment moves toward the west, as indicated by dune morphology, widening streamers, and teardrop-shaped diversions around topographic obstacles (marked with white arrows in Panels C-E). Images: A, C, D, E – ESP_018883_2010_RED, B – ESP_018883_2010_COLOR. Location of Panel A shown in Figure 5.2.

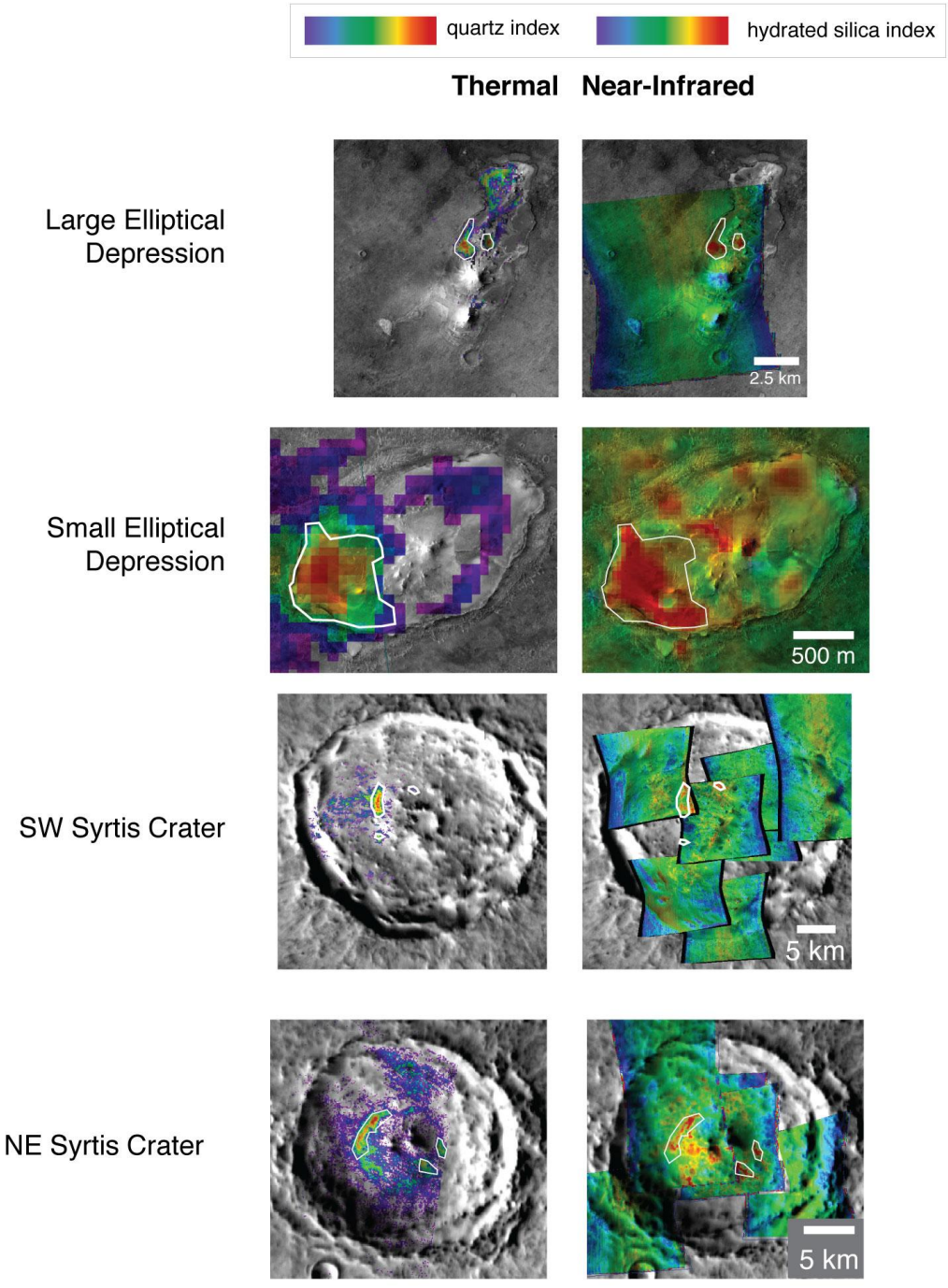

Figure 5.5 — Co-location of quartz-bearing surfaces (as detected using thermal spectra) and hydrated silica-bearing surfaces (detected with near-infrared spectra) in several provinces. Quartz-bearing surfaces are calculated using a THEMIS band 8/5 ratio, isolating quartz TIR absorption features between 8 and 10 μm; hydrated-silica-bearing surfaces appear red or yellow in the CRISM hydrated silica index images. THEMIS IR DCS images (top to bottom): I36289029, I38660006, I334456008, I07887026.

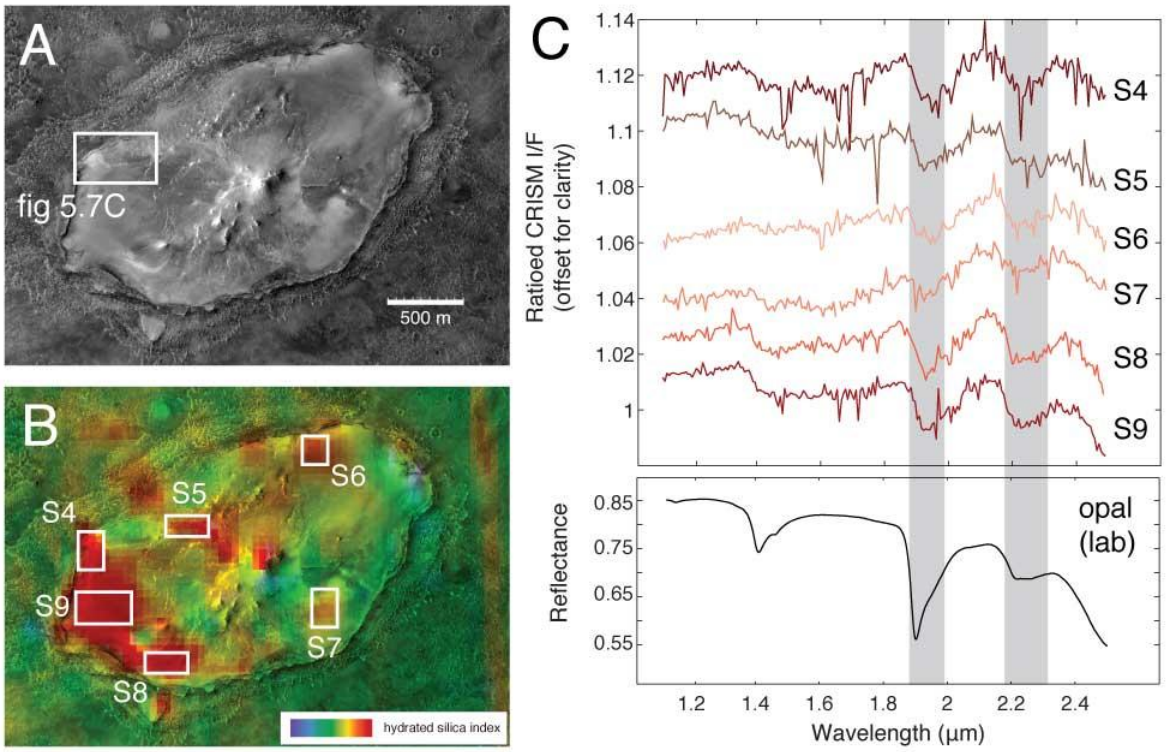

Figure 5.6 — Widespread hydrated silica detections within the Small Elliptical Depression. A) HiRISE image ESP_016048_2005_RED, B) HiRISE image overlain with the hydrated silica index from CRISM image HRL0001330D. C) CRISM spectra of hydrated silica found distributed within the floor of the Small Elliptical Depression [lab opal spectrum provided by E. Cloutis, University of Winnipeg].

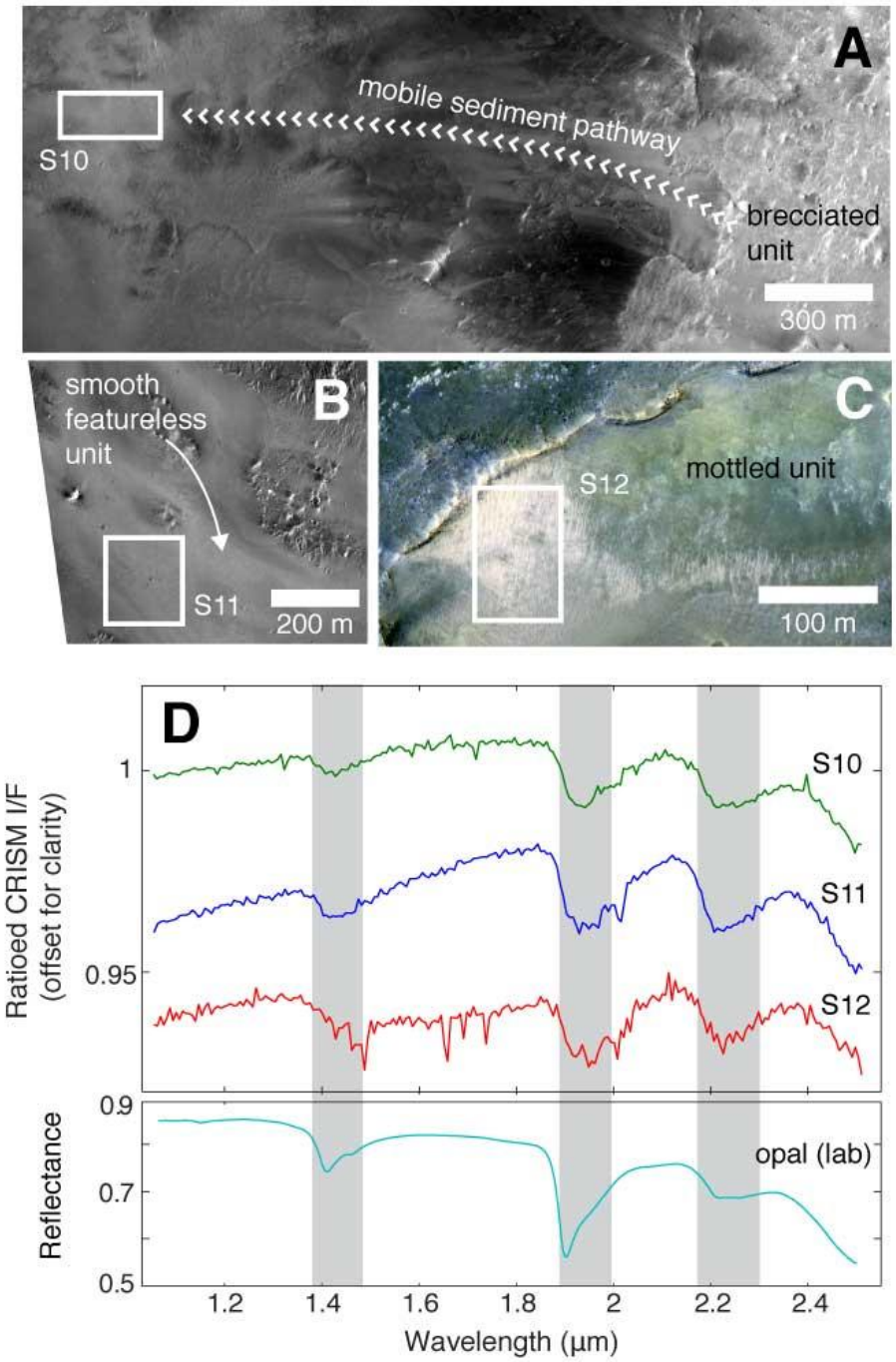

Figure 5.7 — Possible sources of high-silica sediment. A) Pathway of silica-bearing sediment from breccia unit within the central pit of SW Syrtis Crater. As the sediment moves downslope, the high-silica fraction concentrates at the bottom of the basin. Location shown in Figure 5.10 (HiRISE image: PSP_007464_1985_RED). B) Smooth, featureless unit found to be associated with high silica detections using CRISM data; location shown in Figure 5.10. (HiRISE image: PSP_007253_20000_RED). C) Silica-bearing sediments are often found adjacent to this aqua mottled unit, shown here in the Small Elliptical Depression; location in Figure 5.6 (HiRISE image: ESP_016048_2005_COLOR). Another example of the aqua mottled unit–silica relationship can be seen in Figure 5.4B, C.

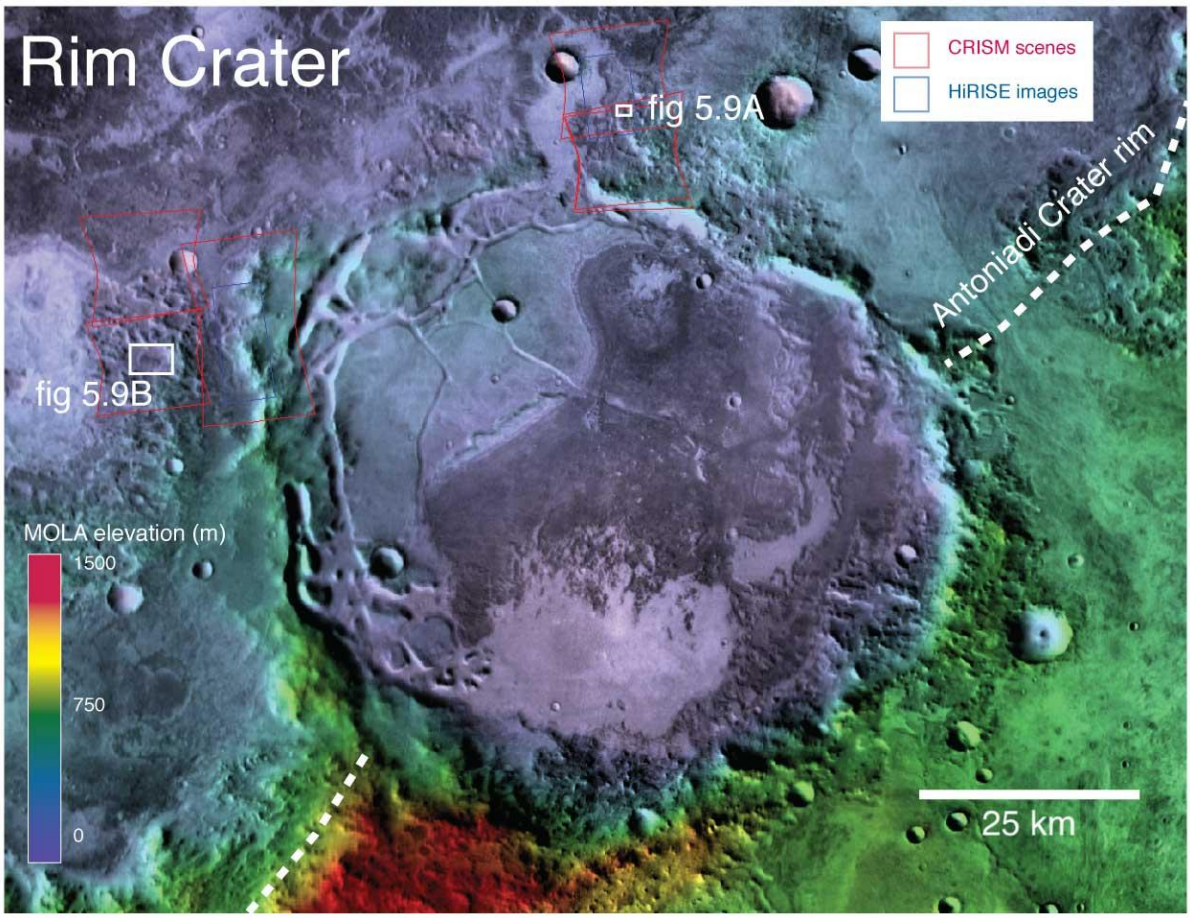

Figure 5.8 — Rim Crater province (location shown in Figure 5.1). Image: Colorized MOLA elevation overlain on THEMIS daytime IR mosaic.

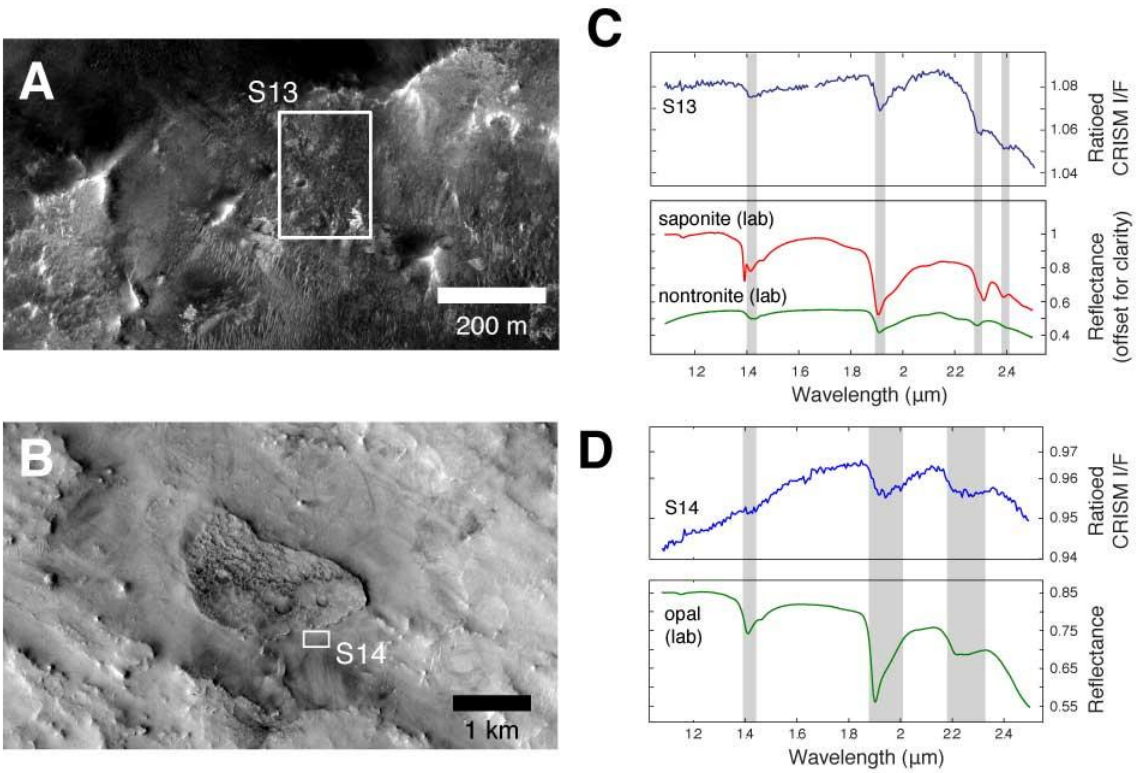

Figure 5.9 — Units and spectra from within the Rim Crater ejecta (locations of images in Figure 5.8). A) Small ridge containing large breccia blocks. Phyllosilicate detections are associated with breccia-rich portions of Rim Crater ejecta (HiRISE image: PSP_006673_2000). B) Mesa topped with pitted terrain, surrounded by deposits of hydrated silica (CTX image: P13_006172_2020). C, D) Comparison of ratioed CRISM spectra and laboratory spectra of nontronite and saponite [*Baldridge et al., 2009*] and opal [courtesy of E Cloutis, University of Winnipeg]. Geologic interpretations of Rim Crater units are often ambiguous, due to discontinuous exposures within the ejecta blanket.

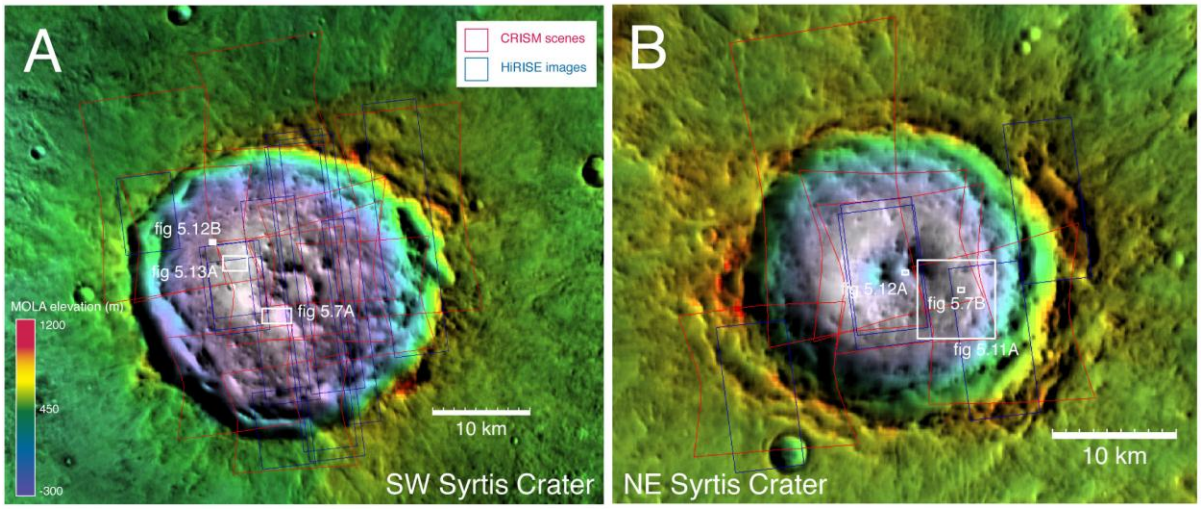

Figure 5.10 — Syrtis Major craters province (locations shown in Figure 5.1). Images: Colorized MOLA elevation overlain on THEMIS daytime IR mosaic.

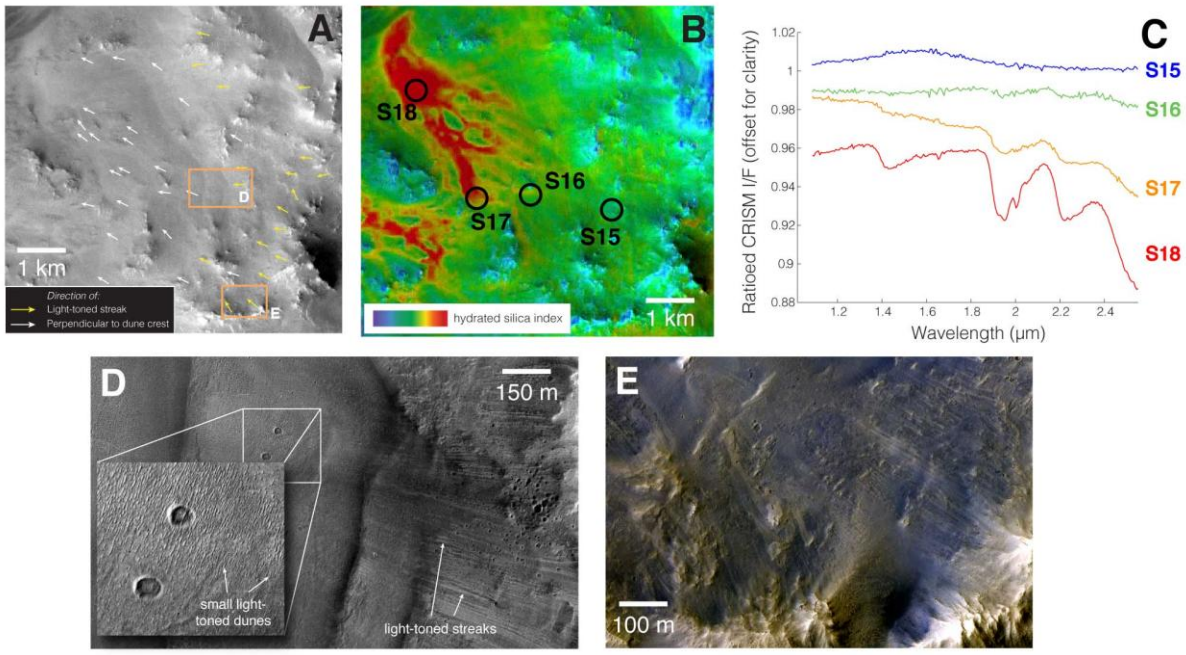

Figure 5.11 — Concentration of silica in sediments moving downslope. A) CTX image of the southwestern wall of the NE Syrtis Crater, with arrows marking the prevailing wind direction as indicated by dune crests and light-toned streaks. B) CRISM hydrated silica index map (FRT00009E5D) overlain on CTX image from Panel A. C) CRISM ratioed spectra taken at locations spaced along the direction of wind. As the sediment is transported, the detection of silica intensifies as demonstrated by the spectral change in Panel B. This intensification along the direction of sediment transport requires a mechanism to concentrate the silica-bearing portion of the sediment. D) HiRISE image PSP_007253_2000_RED showing light-toned streaks (right half of image) grading into light-toned dunes (left half). E) HiRISE image PSP_007253_2000 showing light-toned (brownish) streaks moving toward the upper left. Locations of D and E are shown in Panel A.

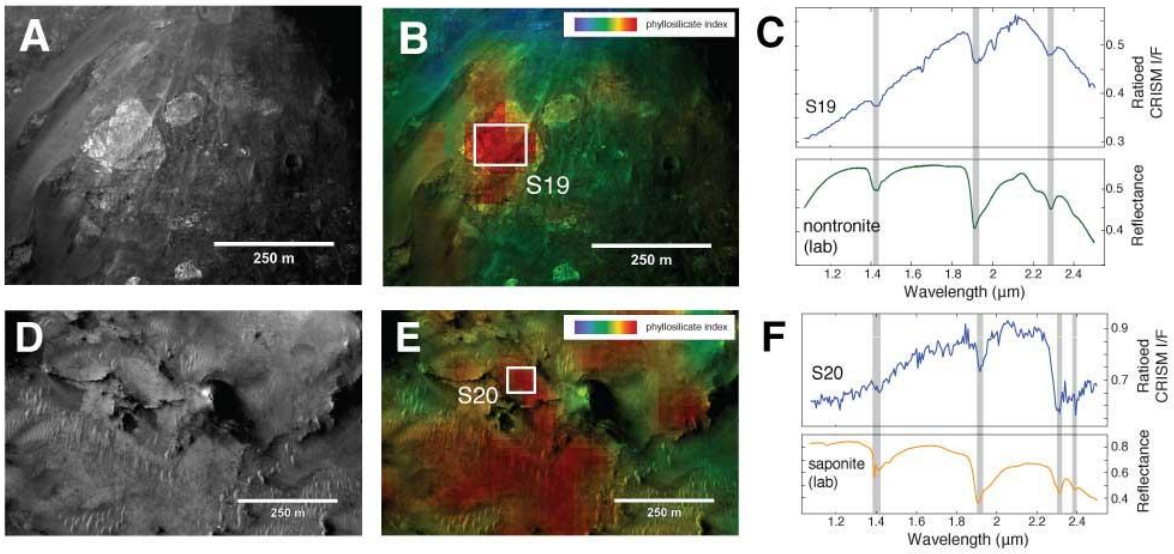

Figure 5.12 — Locations of phyllosilicate-bearing surfaces in Syrtis Craters (locations of images shown in Figure 5.10). HiRISE image (A) and HiRISE overlain with CRISM phyllosilicate index (B) of phyllosilicate-bearing large breccia block found on the central peak of NE Syrtis Crater (HiRISE image: PSP_003205_2000). HiRISE image (D) and HiRISE overlain with CRISM phyllosilicate index (E) of fractured and brecciated phyllosilicate-bearing surface on the floor of SW Syrtis Crater (HiRISE image: PSP_001385_1985). C, F) Comparison of CRISM and laboratory spectra [*Baldridge et al.*, 2009] of phyllosilicates. Phyllosilicates are often found coincident with brecciated and fractured terrains related to cratering.

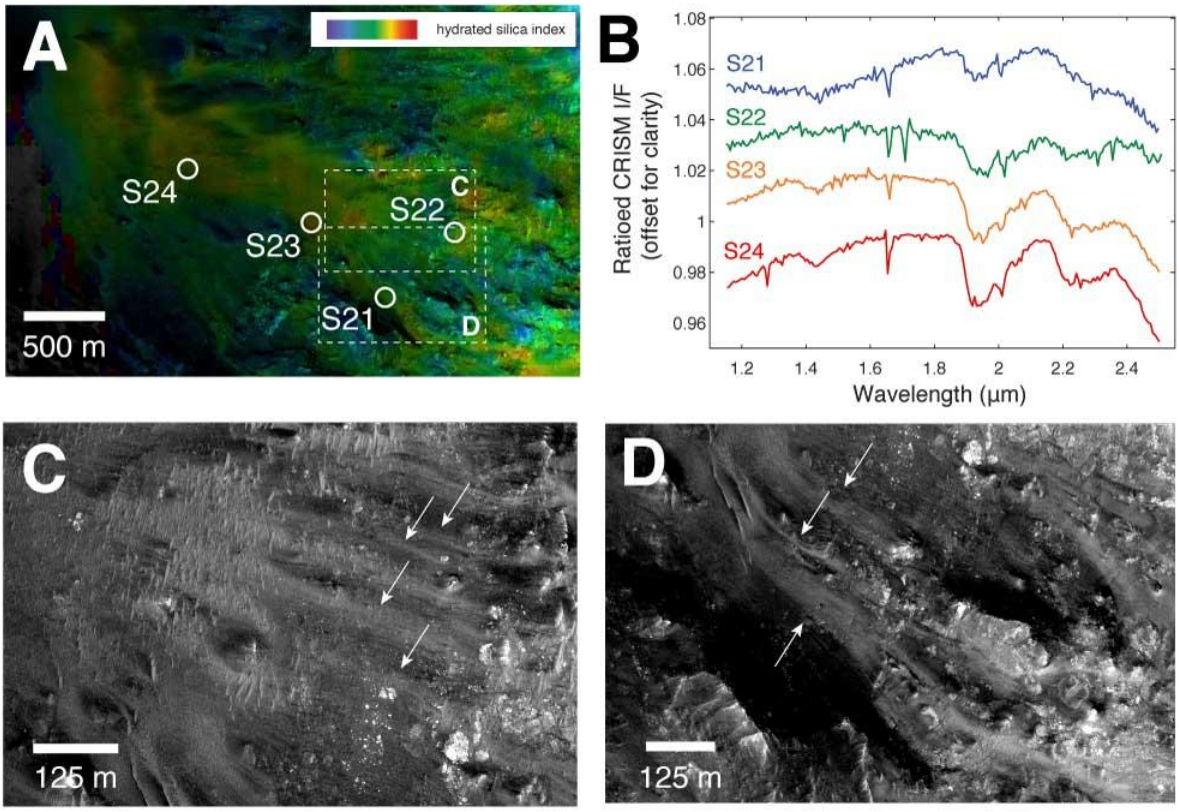

Figure 5.13 — Transport of silica-bearing sediments by wind (location of Panel A shown in Figure 5.10). Aeolian features (white arrows in Panels C and D), show movement of light-toned sediment downslope (toward the upper right in Panel A). When sediment is less concentrated (S21 and S22), CRISM spectra show a less intense detection of hydrated silica than when it is concentrated in ripple-forming locations (S23 and S24). Images: Panels C, D – HiRISE image ESP_022074_1985_RED.

Chapter 6 | Discussion and implications for the Antoniadi Crater region

6.1 Geologic and aqueous history of the region

From the observations of these deposits, specifically the phyllosilicate- and high-silica-bearing units, we seek to describe their larger geologic context, ascertain their aqueous history, and determine the unique contribution of these deposits to the understanding of Martian geological history.

6.1.1 Age of the deposits

All exposures of phyllosilicates and high-silica units have been exposed in impact-related terrain, and their original age and depositional environment are unclear. Furthermore, the silica-bearing units are in unconsolidated sediments, though they appear to originate from brecciated units that outcrop on the floor and walls of the depressions. On the basis of the relationship of these impact-related and brecciated units to better-exposed units constraints may be placed on their formation age. The clearest relationship is that these deposits pre-date the emplacement of Syrtis Major lavas. In all cases, the exposures outcrop from beneath Syrtis flood basalts: within windows to pre-existing crust beneath flood basalts, and on crater floors that have impacted into and exposed material from beneath Syrtis basalts. Alteration of the deposits must have occurred before the end of Syrtis volcanism, which has been dated using crater abundances of the lava plains as Late Noachian to Early Hesperian

[*Hiesinger and Head*, 2004]. Also of note is that exposures of phyllosilicates and high-silica units appear to be sourced in brecciated terrain and may be many steps removed from their initial alteration.

6.1.2 Regional extent of alteration

Because phyllosilicate and high-silica phases are found in many separate exposures, there are two possible descriptions of the extent of alteration: (1) each exposure constitutes one part of a regional-scale alteration event, and the provinces described in Section 3 are merely windows to a relatively contiguous altered crustal unit, or (2) each exposure represents a local alteration event, and the provinces are not interconnected. Explanation #1 is more plausible because of two pieces of evidence. First, within the Antoniadi Crater region, all windows through younger Syrtis lavas to older crust correlate with detections of phyllosilicate/high-silica phases within the limits of the orbital data coverage. Because these phases are found in all imaged locations that have not been buried by Syrtis Major flood basalts, this would suggest that the subsurface unit is more spatially extensive. A more limited spatial extent of these materials would require a highly fortuitous series of events to uncover the exposures. Second, despite the provinces' spanning an area of 10,000's of square kilometers, their spectral and morphological characteristics (e.g. phyllosilicates in layered and brecciated knobs, correlated quartz and hydrated silica detections in colluvium) are largely consistent, more suggestive of a consistent regional unit, rather than a local unit. Whether this unit is more spatially extensive or not, these different exposures all contain similar mineral phases, and represent a relatively uncommon set of formation processes and source

lithologies. Because of this, these observations of the full suite of exposures may be used to construct a single history of the region.

6.1.3 Geological sequence

By combining the various spectral and imaging datasets, the major regional geologic events may be placed in relative chronological order, supported by observational evidence.

The only event that cannot be placed into a clear chronological context is the formation of Antoniadi Crater, since many of the phases on the crater floor are surrounded by flood basalts, and their relationship to Antoniadi Crater is unclear. Because of this, the formation of Antoniadi Crater cannot be confidently placed in the following sequence.

1: Aqueous alteration and phyllosilicate formation

Within the limits of detectability, the high-silica units are found to be distinct from the phyllosilicate-bearing unit, suggesting that the high-silica materials and phyllosilicates formed separately either in space or time. Phyllosilicates are identified within breccia clasts within central peaks of craters, which are the locations of the most deeply excavated pre-existing units within an impact crater [*Melosh*, 1989]. In addition, phyllosilicates are not detected within the Small Elliptical Depression, the most shallow exposure of hydrated phases. This suggests that the phyllosilicate-bearing units are deeply buried and not exposed in the Small Elliptical Depression due to an insufficient depth of excavation. Because phyllosilicates are associated with the deepest

sedimentary units, it may be assumed by the principle of superposition that the phyllosilicate-bearing units formed earliest.

The phyllosilicate detections are associated with impact-related terrain, and recent debate has been concerned with whether hydrated minerals within impact craters existed before the impact and are excavated, or formed as a result of a post-impact hydrothermal system [e.g., *Barnhart et al.,* 2010]. The excavation hypothesis is favored here, because phyllosilicate detections are restricted to breccia clasts in impact craters, and not within the surrounding breccia matrix, suggesting that there was a pre-existing phyllosilicate-bearing unit that was reworked by impacts. As a result, the observed hydrated phases were likely not altered in their present configuration, and the phyllosilicates pre-date the formation of the breccia and were exposed by a subsequent process. It may also be noted that because only the relative age of the phyllosilicate-bearing breccias is constrained and not the formation of the phyllosilicates themselves, the age of the alteration to phyllosilicates may be much earlier than the breccias that contain them.

2: Second pulse of aqueous alteration and silica formation

The spectral and geomorphic evidence is less clear for the method and timing of silica formation. The problem arises from the observation that nearly all silica-bearing deposits are found within unconsolidated sediments at topographic lows in craters and depressions, though the presumed sources of these light-toned sediments have no detectable silica.

The sources of the silica-bearing light-toned sediments appear to be local. This is because sediment pathways that lead to the silica-bearing units are marked by dunes, streamers, and elongated teardrop-shaped diverting around topographic obstacles (Figure 5.4C-E, Figure 5.13C-D). Furthermore, there is spectral evidence to support this migration and concentration of silica-bearing sediments along the direction of sediment transport, shown in Figure 5.11 and Figure 5.13, where the intensity of hydrated silica detection increases along the preferred wind direction and suggests that silica-bearing portion of the sediment concentrates as it moves downslope.

Because only hydrated silica and quartz are observed in the unconsolidated sediments and not in the putative sediment source, an alternate explanation for the observations would be that the sediments were altered in situ. However, these explanations are unlikely because of the observed gradual increase in silica concentration along the observed sediment transport pathway (Figure 5.11; Figure 5.13). This observation is more difficult to explain if the sediments were altered in place after they were deposited. In this case, the sediments would need to have been altered to varying degrees along slopes, then re-transported downslope by wind. Alternately, the sediments could also be progressively altered as they were transported by wind. This is also difficult to explain, because this would necessitate preferential alteration of the light-toned sediment, and not the surrounding surfaces. Therefore, this process does not appear to be controlling the distribution of observed silica, but instead that silica formation occurred prior to the formation of Syrtis Major.

The light-toned sediments emerge from units found stratigraphically beneath the Syrtis Major basalt flows, and are found associated with distinct units that are shallower than the layered phyllosilicate-bearing breccias in all cases: mottled and brecciated units, impact breccias that cover floors and central peaks of impact craters, and smooth and featureless units in crater walls (Figure 5.7). Because they are more shallowly buried, the silica-bearing deposits are presumably younger and represent a more recent episode of alteration.

Because the silica is only detected within sediments, and not within their source, it is not clear whether the alteration of these source units is pervasive or restricted to the clasts/matrix of a breccia. It is possible that the silica-bearing breccias were altered *in situ*, or the silica formed earlier and was reworked by impacts.

3: Formation of Rim Crater

Following the aqueous alteration that formed the silica- and phyllosilicate-bearing phases, a large impactor collided into the altered crust and formed Rim Crater. Because Rim Crater is superposed on the rim of Antoniadi Crater, it is clear that it post-dates the Antoniadi impact; however, it is unclear whether Antoniadi Crater formed before, during, or after the alteration that resulted in the phyllosilicate and high-silica units. Evidence of the timing of the Rim Crater impact is the identification of a brecciated phyllosilicate unit and silica phases in the Rim Crater ejecta blanket. As will be discussed in Section 4.1.3, the formation of these altered phases requires sustained

water-rock contact, and post-impact hydrothermally formed minerals do not commonly form in ejecta blankets nor in terrestrial craters that lack post-impact lakes [*Osinski*, 2005]. Therefore, the alteration likely occurred prior to the Rim Crater impact, and those units were excavated as a result of the cratering process.

4: Syrtis Major and Antoniadi lava flows

Following the Antoniadi and Rim Crater impacts, the floors and ejecta blankets of both craters were buried by lava flows sourced from Syrtis Major and locally within Antoniadi Crater [*Hiesinger and Head*, 2004]. The Large Elliptical Depression, Small Elliptical Depression, and Rim Crater provinces all represent incomplete burial by Syrtis Lavas or erosional windows beneath them, leaving the underlying older crust exposed.

5: Formation of Syrtis Craters

The two Syrtis Craters to the southeast of Antoniadi Crater impacted into the Syrtis Major lava flows, with intact ejecta blankets still present covering the local basaltic crust (Figure 5.10).

6: Aeolian surface modification

Following the formation of the Syrtis Major shield volcano complex, very little geological activity has taken place. Slow degradation of the crust by aeolian processes continues to occur, as meter- and decameter-scale ripples are prevalent. Aeolian transport has moved light-toned sediment to local basins. This transport appears to

have concentrated the siliceous component of the sediments as it moves downslope. This could be accomplished by either winnowing away more mobile mafic materials, or by preferentially eroding the silica-rich fraction and leaving behind the mafic component (Figure 5.11). Because the high-silica units are sourced from units that appear predominantly basaltic using TES/THEMIS data, the more mafic minerals within the source rock (e.g. pyroxenes and olivine) must have been removed or left behind by this process.

This relative geologic sequence describes the timing of large events, but is unable to constrain the duration of any of these episodes by stratigraphic evidence alone. In the next section, the implications for the length of alteration of the high-silica units are described, as constrained by the mineralogical evidence.

6.2 Silica: Diagenesis, terrestrial examples and implications for the duration of water

A unique characteristic of this study region is the identification of crystalline quartz and plagioclase feldspar using TES/THEMIS data, which are both consistently co-located with hydrated silica identified using CRISM data (Figure 5.5). Because this region contains the only currently known detection of quartz on Mars, a brief recap of quartz formation is described here and a discussion of the possible mechanisms and implications of its origin and its relationship with hydrated silica and plagioclase.

In terrestrial settings, co-located quartz and hydrated amorphous silica (opal-A) or paracrystalline silica (opal-CT) are found within units that are formed by multiple processes: diagenesis or other low-grade metamorphosis of opaline silica deposits [*Hesse,* 1989], or primary precipitation of microcrystalline quartz (e.g. chert) and opal from saturated solutions in sedimentary rocks [*Knauth*, 1994]. Amorphous, hydrated opaline silica is formed on Earth in many settings, both biotic and abiotic in origin.

Abiotic opal-A will undergo diagenesis to paracrystalline and crystalline phases (opal-CT, then microcrystalline quartz) in the presence of water [*Hesse,* 1989]. The rate of this reaction is dependent on temperature and water availability, ranging from a few thousand years [e.g. *Lynne et al.,* 2005] to an estimated 400 Ma in a hypothetical water-rich Martian environment at 0°C [*Tosca and Knoll,* 2009]. The diagenetic transition from opal-A to quartz represents a continuum, and multiple phases will appear in a single deposit undergoing diagenesis.

The diagenetic transition from opal-A to quartz may be tracked with TIR spectroscopy [*Michalski et al.,* 2003; *McDowell,* 2009]. In the TIR, quartz is identifiable with several diagnostic features, including one at 21 μm (470 cm^{-1}) and a doublet at 9.1 μm (1100 cm^{-1}). These features are distinct from those of opaline silica, which do not display the 21 μm feature, but instead have one broad short-wavelength feature centered at 8.3 μm (1200 cm^{-1}) and a diagnostic asymmetric feature at 20 μm (500 cm^{-1}). TES spectra of the quartzofeldspathic deposits that were used for this study do not preclude the presence of a substantial amount (10–20%) of amorphous phases, and a mixed opal-

A/quartz deposit is consistent with the observations. By contrast, TES studies of other silica exposures [e.g. W. Hellas Basin; *Bandfield,* 2008] show strong detections of amorphous silica and no quartz detections in the TIR. Therefore, the TIR evidence of quartz at this site may indicate a greater degree of alteration than at other exposures of hydrated silica, suggesting either a greater persistence of liquid water and/or higher temperatures at this site.

Silica phases are also distinguishable using their near-infrared spectra, as discussed in Chapter 4. The relative crystallinity of all silica detections was determined using the band indices of *Rice et al.* [2012], and shown in Figure 6.1 relative to global Martian silica deposits. From this, two things are observed. First, the crystallinity of these deposits is similarly consistent, despite ~100 km between exposures. Second, all silica within the Antoniadi Region is more crystalline than other deposits elsewhere on the planet, suggesting pervasive and large-scale alteration of the region.

Instead of a diagenetic origin, microcrystalline quartz may also form as a direct precipitate from solution without an opal-A precursor phase. Primary microcrystalline quartz precipitation has been found in many terrestrial settings: the replacement of the sodium-silicate mineral magadiite in tertiary alkaline lakes in Kenya [*Eugster,* 1967; 1969; *Sebag et al.,* 2001] and Oregon [*Rooney et al.*, 1969]; near-surface pedogenic formation in silcretes [*Summerfield*, 1983; *Dixon and McLaren,* 2009], and as a minor phase in hydrothermal-volcanogenic deposits [*Rimstidt and Cole*, 1983; *Leatherman*, 2010]. Chert contains 0.2 – 2.0 wt % water [*Knauth*, 1994] and forms Si–OH bonds

along dislocations and in pore space [*Graetsch,* 1994]. Some laboratory cherts do display the visible and near-infrared spectral absorption features used to identify hydrated silica — at 1.4, 1.9, and 2.21 μm — though others do not [*McDowell,* 2009]. Furthermore, chalcedony, a fibrous variety of microcrystalline quartz commonly precipitated in small voids of igneous rocks or through recrystallization of amorphous silica, also exhibits these same 1.4, 1.9 and 2.21 μm spectral features indicative of hydrated silica [*Florke et al.,* 1982].

Of the terrestrial settings that may contain sedimentary quartz, both the diagenetic or silcrete origins for the high-silica deposits are most consistent with the observations for the following reasons. First and most importantly, all detections of silica are found coincident with plagioclase which precludes those sedimentary settings where all minerals are formed authigenically (newly formed in place): magadi-type cherts and hydrothermal deposits. Plagioclase is only rarely formed as an authigenic precipitate in sedimentary environments [e.g. *Turner and Fishman,* 1991], but instead is most often formed as a primary mineral in igneous rocks and volcanigenic sediments. When precipitated authigenically, plagioclase directly replaces zeolites or is found in close association with them, most commonly analcime [*Hay, 1966*]. Analcime was detected as a minor phase within the central peaks of the two Syrtis Craters by *Ehlmann et al.* [2009], but not with any other exposures in or around Antoniadi Crater. Therefore, it is unlikely that this feldspar formed as an authigenic diagenetic mineral, but instead formed as a primary igneous mineral. A situation where quartz can form authigenically while feldspar is able to avoid weathering is in an sodium-rich alkaline environment,

such as in low-temperature hydrothermal alteration of seafloor basalts [*Humphris and Thompson*, 1978]. In this case, albitization of feldspars dominates, and formation of clays and zeolites is minor. This scenario is plausible, as early Mars has been assumed to have been alkaline [*Bibring et al.*, 2006] and saline [*Fairen et al.*, 2009]. Because of this, the scenario that is the best fit with these observations is a protolith — crystalline or glassy — was weathered to produce a plagioclase and quartz-rich alteration product, such as in the case of diagenetic and silcrete-formed quartz. Furthermore, hydrothermal quartz is mostly deposited as chalcedony in fractures and vugs, which tends to be durable and resistant to erosion and does not easily erode to form aeolian features [*Maher and Shuster*, 2012], making this formation mechanism less likely.

Chalcedony also fits with the spectral observations, exhibiting features of both crystalline quartz in the TIR and hydrated silica in the NIR. However, of the two main pathways to chalcedony formation — primary deposition from hydrothermal fluids and diagenetic alteration of opaline silica or silica glass — the diagenetic transformation of amorphous/glassy silica is more likely based on the petrology of primary chalcedony, which tends to form very hard and durable veins and vug-fills in pre-existing rocks that are relatively difficult to erode and transport compared to their surrounding rocks [*Maher and Shuster*, 2012]. Chalcedony only rarely forms aeolian bedforms on Earth, and forms due to reworking by a combination of erosional processes (water, wind, ice) [e.g., *Evans*, 1962]. However, diagenetic transformation of opaline silica to chalcedony is very plausible and is concordant with all observations.

One obvious scenario for producing quartz on Earth that has not yet been discussed is as a primary igneous mineral. Quartz is a minor component (0–5%) of basalt and Martian meteorites [*McSween,* 1985], indicating that unaltered basalt is an unlikely source rock for these quartz-rich sediments. Thus, this scenario would require a more felsic igneous protolith to produce the observed mineral suite, and some degree of aqueous alteration to produce hydrated silica. However, this explanation is unlikely, despite intermediate volcanic units having been detected locally near Nili Patera in isolated flows and deposits [*Christensen et al.*, 2005]. There is no spectral evidence for a felsic protolith near Antoniadi Crater, nor is the source rock for these sediments obviously quartz-rich within the spatial resolution of TES/THEMIS data. This would suggest that authigenic precipitation of quartz as chert is a more plausible scenario for quartz formation here, instead of as a primary volcanic mineral. A glass-rich precursor is the most likely candidate to fit the observations, since the glassy fraction is more susceptible to alteration and quickly alters to phyllosilicate- and silica-rich phases in terrestrial examples [*Hay and Iijima,* 1968; *Staudigel and Hart,* 1983] leaving behind the plagioclase that is observed. This glassy precursor may have been felsic (e.g. rhyolitic tuff), which is consistent with the observations of quartz and plagioclase, and with the lack of observations of minerals that would have been formed through alteration of a mafic protolith. Or, the protolith may have been basaltic and altered to form secondary authigenic quartz, and the iron-, magnesium-, and calcium-bearing alteration products were winnowed away or left behind during transport of quartz- and plagioclase-rich sediments. Once the deposit has been altered, subsequent aeolian mechanical sorting would concentrate the larger-grained quartz/hydrated silica and plagioclase, and

remove finer-grained products of alteration of basalts (phyllosilicates and zeolites), as observed in terrestrial siliciclastic sedimentary deposits [*Argast and Donnelly,* 1987]. The increase in spectral features may also attributed to the effect of increasing grain size along the sediment transport, as spectral contrast may also be increased with larger grain sizes [e.g. *Hapke,* 1993]. Although possible, increased grain size is probably not contributing to the observed increase in spectral features, primarily because the increased detections are spatially correlated with a concentration of lighter-toned sediments along sediment transport, and coarser sediments more commonly darken surfaces due to increased volume interactions [*Hapke,* 1993]. It may be possible, however, that there is a combination of increasing grain size and mineral concentrations that are resulting in the observed signal. At minimum, the detections of quartz are spatially linked with both the identification of hydrated silica and plagioclase feldspar, and are found associated with mobile fine-grained material that has been transported from a source that has no discernibly elevated quartz, plagioclase, or hydrated silica components. Because of this, all observed mineral phases appear to have begun as constituents of the source rock and were less mobile than the other surrounding mafic minerals, or eroded out preferentially.

An important note in this discussion is that this study is able to demonstrate a useful application of the combination of spectral ranges provided by CRISM and TES/THEMIS. The complementary sensitivities of the two wavelength ranges allow for the independent detections of hydrated silica and quartz that, when combined, reveal that the quartz is likely authigenically precipitated, instead of a primary igneous mineral.

Surfaces with a bulk basaltic composition are also detected within the phyllosilicate-bearing units and for the source rocks of the quartzofeldspathic sands, placing further constraints on the formation mechanisms for these hydrated minerals. The application of this technique illustrates the use and need for the combined analysis of both datasets.

6.3 Broader geologic context

6.3.1 Other exposures in the Syrtis Major region

Several recent studies have described the types and distribution of hydrated silicates in locations hundreds of kilometers to the east of the study area: the greater Isidis Basin/Nili Fossae region, and within Toro Crater (Figure 6.2). These mineral assemblages share many common characteristics with those near Antoniadi Crater, and raise the following questions:

How are these mineral assemblages similar to and different from those in the Antoniadi region?

Do the exposures in Antoniadi, Nili Fossae, and Toro Crater exhibit common episodes of alteration, or are they unconnected from one another?

Can the information from each region (Antoniadi, Nili Fossae, and Toro Crater) be used to help inform the study of the others?

Isidis Basin. Isidis Basin, an ancient 1900-km-diameter impact crater ~850 km to the east of Antoniadi Crater, and Nili Fossae, a series of narrow valleys (~600 m deep) west

of Isidis that formed as a result of the impact, have been the subject of much study since they were first identified to contain regions with high olivine abundance [*Hamilton et al.*, 2003; *Hoefen et al.*, 2003, *Hamilton and Christensen*, 2005; *Mustard et al.*, 2005; *Tornabene et al.,* 2008], and subsequently targeted with CRISM as containing a unique and diverse suite of hydrated silicates [*Ehlmann et al.,* 2009], magnesium carbonate [*Ehlmann et al.,*2008], and serpentine [*Ehlmann et al.,* 2010a]. A detailed morphological and mineralogical study performed in companion papers by *Ehlmann et al.* [2009] and *Mustard et al.* [2009] revealed that hydrated minerals in Nili Fossae were found in a vertical sequence (Figure 6.3B). The lower-most section consists of phyllosilicates, predominantly Fe- and Mg-smectites, located within the brecciated clasts and matrix in the lowermost Noachian crust. Phyllosilicate-bearing clasts are found adjacent to unaltered mafic clasts and matrix, and associated with basaltic mineral signatures in THEMIS spectra [*Mustard et al.,* 2009]. The phyllosilicate-bearing breccia layer is sporadically overlain by an olivine-bearing layer interpreted to be the Isidis impact melt sheet, covered by a draping layer containing either kaolinite (over phyllosilicate-bearing terrain in western Nili Fossae) or magnesium carbonate (over olivine-rich deposits in eastern Nili Fossae), and capped with an anhydrous mafic unit.

How does the Isidis stratigraphic sequence correlate with the exposures within the Antoniadi Crater region? Both contain a similar lowermost layer comprised of a Noachian-aged Fe- and Mg-smectite-bearing brecciated unit, with clasts of similar size (up to hundreds of meters). The Antoniadi assemblage lacks the high-olivine layer and

its alteration product magnesium carbonate, consistent with the interpretation of Nili Fossae as containing impact melt, not expected in the Antoniadi Crater region.

In addition to the lack of olivine and carbonate, a major difference between the Antoniadi Crater region and Nili Fossae is the presence of a kaolinite-bearing layer draping the brecciated phyllosilicate-bearing crust in several locations in Nili Fossae, but not in Antoniadi. Kaolinite forms terrestrially as either a primary precipitate or as a product of chemical weathering [*Murray*, 1988]. In all cases, kaolinite tends to be associated with relatively large volumes of water that weather rocks and remove cations in an open system. In stagnant systems with reduced water flow, cations (e.g. potassium) are conserved and the formation of illite is thermodynamically favored over kaolinite [*Murray*, 1988], though this process may not hold in a potassium-depleted environment such as Mars.

The presence of authigenic quartz in the Antoniadi Crater deposits (as explained in Section 4.1.3) also suggests persistent water at the site, but not an equivalent formation mechanism. The biggest difficulty with linking the two formation sequences is the presence of plagioclase feldspar within the Antoniadi deposits. Kaolinite most often forms terrestrially from the aqueous alteration of feldspars, resulting in an antithetical relationship in weathering environments [*Nesbitt and Young*, 1989]. Assuming similar weathering histories between Antoniadi Crater and Nili Fossae, it is expected for feldspars to have been at least partially altered to kaolinite in the Antoniadi deposits,

which is not observed. Second, the role of water in the two environments differs. For kaolinite to form, one of the following must occur [*Murray,* 1988]*:*

- kaolinite may precipitate from acidic hydrothermal fluids, which are commonly sulfurous [e.g. *Dekov et al.*, 2008];
- feldspars or phyllosilicates may be leached by fluids to remove cations and alter to kaolinite [e.g. *Nesbitt and Young*, 1989].

For authigenic quartz to form in the possible scenarios, it would require either: (1) persistent water to drive the diagenetic transformation from opal to quartz [*Herdianita et al.,* 2000] or (2) mixing of alkaline waters saturated with dissolved silica with acidic fluids to precipitate authigenic opal-CT/quartz as silcretes [*Smale,* 1973]. Since neither aqueous regime mimics that which is predicted for the Nili Fossae kaolinite formation, the aqueous histories of these two deposits are not directly equivalent, though they may share similar timing of their wet periods.

Toro Crater. *Marzo et al.* [2010] investigated the mineralogy and geologic history of Toro Crater, a 40 km impact crater ~500 km to the east of Antoniadi Crater. Toro contains a suite of hydrated silicate minerals — hydrated silica and phyllosilicates, including prehnite — that are commonly found within impact breccia clast-rich regions and the sediments derived from them. Prehnite is a low-grade metamorphic phyllosilicate mineral typically found in hydrothermal systems. Prehnite forms on Earth in a narrow set of environmental conditions (200–350°C, pressures < 3 kbar, and

low partial pressures of CO2 — $X_{CO2} < 0.004$ at 1.5 kbar [*Schiffman and Day*, 1999]) and has been assumed to have formed in the Martian subsurface out of contact with the Martian atmosphere, and later exposed through impact excavation. The formation temperatures of prehnite are much higher than those associated with hydrated silica and phyllosilicates and, as a result, an elevated temperature gradient and/or depth of alteration must have existed for at least some of the exposures at Toro Crater. A modified interpretive cross-section of the crater is shown in Figure 6.3C.

Marzo et al. [2010] interpret the hydrated mineral suite in Toro Crater to have formed as a result of a post-impact hydrothermal system, having identified putative hydrothermal mounds on the central peak. However, a difficulty of this model is the fact that the hydrated minerals are located within relatively light-toned fractured bedrock on the central peak and light-toned breccia clasts in the impact melt sheet, but not within the melt sheet itself. On Earth, melt sheets commonly weather more easily than brecciated clasts within the same rock because the melt sheet is typically comprised of a fine-grained glassy matrix that is more chemically reactive than crystalline rock [*Newsom et al.,* 1986]. *Marzo et al.* [2010] do not preclude the possibility that hydrated mineralogies formed prior to and were excavated by the Toro impact, which appears to be more consistent with the observations.

Assuming that the Toro impact excavated the observed hydrated phases, the portions of the crater corresponding to exposures of the most deeply excavated layers, the central peaks and their flanks, contain fractured bedrock and breccia clasts containing

phyllosilicate (prehnite, smectite, and chlorite) signatures. Farther onto the flanks of the central peak and onto the crater floor, opaline silica is detected within breccia clasts, suggesting that the clasts have been excavated from a more shallowly buried layer. This stratigraphy — silica-bearing layers overlying phyllosilicate-bearing brecciated units — is consistent with the observations in the Antoniadi region. However, there are no detections of quartz associated with these deposits, suggesting some differences in protolith composition or alteration environment. Despite these differences, the shared history of two distinct pulses of aqueous alteration suggest that it is possible that the hydrated mineral assemblage in Toro Crater formed as part of a similar, if not the same, sequence that altered the Antoniadi deposits.

Summary of regional exposures. Because there are similar morphologic and mineralogic characteristics between Syrtis Major, Nili Fossae, and Toro Crater, it is possible that they may be linked. The evidence of this linkage is that they all share a similar stratigraphy, where a phyllosilicate-bearing basement layer is overlain by minerals that indicate subsequent aqueous alteration: crystalline quartz at Syrtis Major, kaolinite and magnesium carbonates at Nili Fossae, and opaline silica at Toro Crater (Figure 6.3). Furthermore, in all locations, phyllosilicates and some other hydrated phases are associated with Noachian breccias within excavated terrains. Because there is a shared phyllosilicate-bearing basement layer directly overlain by mineral phases suggesting subsequent aqueous activity, it may suggest the possibility of common region-wide events.

However, despite the similarities among these sites, each is partially distinguished by its own unique mineralogy. Nili Fossae, unlike other locations, has extensive exposures of a kaolinite-bearing layer that suggests both a considerable amount of water and a well-drained regolith to alter local rocks and remove cations to form kaolinite. Also, Toro Crater contains the mineral prehnite, suggestive of higher temperatures and formation at depth. The differences between Nili Fossae, Toro Crater, and Antoniadi Crater demonstrate that, despite some similar conditions required for early phyllosilicate formation and subsequent aqueous alteration, other formation conditions must have varied considerably among these locations.

6.3.2 Global context

Elsewhere on Mars, there are several exposures of hydrated silica and/or amorphous silica in a variety of geologic settings: "Home Plate" at Gusev Crater [*Squyres et al.* 2008, *Ruff et al.*, 2011], Meridiani Planum [*Glotch et al.,* 2006], and Valles Marineris [*Milliken et al.,* 2008]. Of these exposures, the Valles Marineris and Meridiani Planum deposits are found in close association with sulfate and iron-oxide minerals, including jarosite, and are thought to have formed under acidic-sulfate leaching conditions. Because of this, these silica deposits do not appear similar to those near Antoniadi Crater, which are not found in conjunction with sulfates. In Gusev Crater, high concentrations (65–92 wt %) of opaline silica have been found in bright white soils and attributed to acid-sulfate leaching of the surface, citing an enrichment of titanium and close association with sulfates as evidence of its formation environment [*Squyres et al.,* 2008]. However, recent reanalysis by *Ruff et al.* [2011] has argued that at least some of the Gusev silica is

more likely formed through silica sinter precipitation from hot, neutral-to-alkaline waters in a hydrothermal system, as evidenced by morphologic and mineralogical constraints, including the recent identification of nearby carbonates [*Morris et al.,* 2010] which indicate that neutral-pH waters also existed locally. If Gusev Crater represents a region of silica precipitation under neutral-to-alkaline conditions, this may provide an analog for the original deposition of high-silica phases, though the maturation of the opaline silica to quartz has not been observed by Spirit [*Ruff et al.,* 2011].

Mineral assemblages elsewhere on Mars also exhibit combinations of phyllosilicates and hydrated silica in a vertical sequence. An example is the exposures of silica within Mawrth Vallis, found to contain both iron and magnesium smectites in thick, fractured sections of bedrock [*Wray et al.,* 2008] draped by hydrated silica- and kaolinite-bearing units [*Bishop et al.,* 2008]. However, hydrated silica within these deposits is not essential to the observed spectral shape at 2.2 μm, which has been successfully modeled requiring only a mixture of phyllosilicates and no hydrated silica phases [*McKeown et al.,* 2011]. An opaline-silica-bearing mound in Terra Sirenum (near Columbus Crater) has also been observed to be in close association and with kaolinite-bearing units [*Wray et al.,* 2011]. The formation of kaolinite and silica have been attributed to two possible processes: (1) sustained leaching of existing phyllosilicates through acidic pedogenic processes, forming a kaolinite/silica assemblage commonly observed in terrestrial altered basalts [e.g. *Bishop et al.,* 2007], or (2) leaching of phyllosilicates to form kaolinite, and alteration of a different, more silicic protolith to form opaline silica [*Bishop et al.,* 2008].

In addition, there are many global exposures of mineral assemblages akin to those found in Nili Fossae exhibiting phyllosilicate-rich basement rocks draped by a kaolinite-bearing layer of constant thickness: in Valles Marineris [*Murchie et al.*, 2009] and a possible 1000 × 1000 km deposit in the Mawrth Vallis/western Arabia Terra region [*Noe Dobrea et al.,* 2010].

All known exposures of combined phyllosilicates and kaolinite and/or silica, in addition to being morphologically and stratigraphically similar, are also believed to have formed contemporaneously. Antoniadi Crater, Nili Fossae, Mawrth Vallis, Arabia Terra, and Valles Marineris — regions that display evidence of more extensive aqueous alteration — have been temporally constrained as forming near the Noachian-Hesperian boundary, a period on Mars linked with wetter conditions than today as evidenced by fluvial landforms [e.g., *Baker,* 1979; *Carr,* 1979; 1995] and valley network formation [*Pieri,* 1980; *Fassett and Head*, 2008]. The abundance of water at the time helps explain the abundance of hydrated phases detected in units formed near the Noachian-Hesperian boundary, but does not necessarily indicate that all units formed in a similar fashion. As explained in Section 4.3.1, kaolinite formation is commonly linked to acidic hydrothermal precipitation or leaching of cations from feldspars or preexisting phyllosilicates in well-drained soils or regolith. Hydrated silica deposits at Valles Marineris are found in conjunction with jarosite, again suggesting acidic conditions. Though high-silica deposits can form in fluids of variable pH, the deposits at Syrtis Major indicate a sufficiently neutral-to-alkaline environment to dissolve silica into

solution and reprecipitate authigenic quartz. Even when the kaolinite formation is presumed to have occurred in neutral or alkaline conditions, such as Nili Fossae, its formation requires a steady flow of water through the soil in an open system to leach cations and leave behind kaolinite. This is in contrast to the closed system required to diagenetically alter opaline silica to quartz through steady dissolution and reprecipitation. The conditions that formed the deposits at Syrtis Major are different than those elsewhere on the planet, though both were facilitated by the abundance of water at the time.

6.3.3 Geology on a reworked planet

Within the Noachian deposits in Antoniadi Crater, there is a frequent association of high-silica mineral phases with breccias in the floors, central peaks, and ejecta of impact craters. This correlation is not unique to this site, with many ancient global altered mineral exposures found within impact-brecciated terrains regionally (Nili Fossae and Toro Crater) and globally, for example in the Columbia Hills in Gusev Crater [*Arvidson et al.*, 2006] and the walls and ejecta of craters in the southern highlands [*Buczkowski et al.*, 2010; *Ehlmann et al.*, 2010b]. Additionally, there are many Noachian hydrated mineral phases that have been reworked and deposited as detrital sediments, such as the fluvial deposits within Holden Crater [*Grant et al.*, 2008] and deltaic deposits in Eberswalde [*Malin and Edgett*, 2003; *Moore et al.*, 2003] and Jezero Craters [*Fassett and Head*, 2005].

Ancient reworked deposits pose big challenges for determining their geologic history. The most obvious obstacle is finding their age of original formation, since they are observed at least one step removed from where they formed. Commonly, this is at least partially remedied by relative age constraints provided by their location, but numerical crater-count ages are often impossible to discern. The lack of a numerical age makes comparison between different units, and constructing a global picture, difficult without the ability to link geologic exposures in time. The second difficulty with reworked deposits is placing their mineralogy into a broader regional geologic context. When reworked units are not intact or in their original orientation, spatial relationships (e.g., mineral zonation) cannot be determined. Instead, breccia clasts, ejecta, and detrital deposits are analyzed in isolation, without the ability to determine where they formed relative to one another. Recent attempts have been made to utilize the unique information from impact craters by combining modeling and observation of craters of different sizes to determine the depth to a phyllosilicate layer in the Mawrth Vallis region [*Barnhart and Nimmo*, 2011], though application of similar techniques is still in its infancy. Because Noachian deposits have been subjected to >3 Ga of impact erosion and burial, as well as fluvial and aeolian activity, they are inefficient recorders of their geologic environment at their formation, adding significant complications to remote geologic investigations performed on these ancient terrains.

An example of the complications in piecing together a geologic history from Noachian rocks is described by *McCoy et al.* [2008], who encountered similar difficulties when determining the history of Columbia Hills of Gusev Crater with observations from the

Spirit rover. Even with the benefit of *in situ* measurements, the geologic sequence of events — deposition of impact and volcaniclastic sediments, aqueous alteration, erosion, and burial — is unclear, and there is no unique sequence to fit the observations. Instead, the only timing constraints are provided by the burial of Hesperian-aged Adirondack-class lavas, and only relative age constraints may be assigned to the emplacement and alteration of the Columbia Hills units.

In summary, because aqueous phases exposed on the Martian surface are often at least one step removed from their original formation environment, arriving at firm conclusions about timing or formation environment is extremely difficult or completely impossible in ancient reworked surfaces.

6.3.4 Summary and unresolved questions

Placing the Antoniadi Crater region in a broader context, it shares many common aspects with regional and global mineral exposures. In nearby Nili Fossae and Toro Crater, and in distant exposures at Mawrth Vallis and Valles Marineris, there is a similar vertical sequence of phyllosilicate-bearing brecciated basement layers overlain by phases that indicate a separate pulse of more intense aqueous alteration. Because the Antoniadi Crater exposure is heavily reworked, it is doubtful that the Antoniadi Crater exposures reflect the original alteration environment, but may be the result of impacts into the products of sequential alteration events. Furthermore, all of these exposures are likely late Noachian in age, suggesting possible widespread episodic wet events in the Martian past.

Despite these similarities to other regional deposits, many questions about the specific history of the Antoniadi Crater deposits remain unresolved. What is the source of the water that altered these deposits – meteoric, groundwater or hydrothermal? The answer to this question is elusive, because the altered phases are commonly found in reworked terrains, and their current location can give us no information about their original formation environment. Furthermore, neither hydrated silica, quartz, plagioclase nor smectite clays imply a unique method of formation, leaving their depositional or formation environment unknown at Antoniadi Crater.

For the purposes of this study, a more important question might be: why did quartz only form near Antoniadi Crater and apparently nowhere else on the planet? This question is likewise difficult, because the quartz that is observed has been sourced from ancient brecciated units (containing no detectable quartz), eroded and concentrated as it is transported downslope, and deposited in dunes, meaning that its current location is at least twice removed from where it formed. The simplest answer is that there was a greater amount of heat or water in a closed system to facilitate the diagenetic transition of opal to quartz. But why here and not elsewhere, or is this only location where it is exposed at the surface? Was the protolith more felsic? Was alteration to quartz driven by more water or more heat? And how is the quartz and plagioclase distributed in the source rock so that they are able to be concentrated as they are transported, and what was winnowed away? These questions, though important, require more detailed

information than can be supplied by a remote study, and would likely be best answered by *in situ* examination of source rock and sediments.

6.4 Astrobiological implications of the observed mineral phases

The Antoniadi Crater region contains many favorable characteristics for fostering life and preserving biosignatures. First, the waters that formed the observed hydrated phases were likely neutral to alkaline. Smectite clays, similar to those observed here, require neutral-to-alkaline conditions to form terrestrially [*Velde,* 1995]. Similarly, both diagenetic and silcrete-formed microcrystalline quartz form more readily in alkaline solutions; both methods require silica to be dissolved and reprecipitated via irreversible Ostwald ripening [*Morse and Casey,* 1988], and the solubility of silica is strongly dependent on pH, increasing by orders of magnitude for pH>9 [*Williams and Crerar,* 1985]. Moderate- to high-pH conditions have been shown to be more favorable for nascent life because many early biologic reactions, such as the synthesis of early amino acids, occur more rapidly in alkaline waters [*Miller and Orgel*, 1974]. Second, the presence of more highly altered phases, such as paracrystalline or crystalline silica, at Antoniadi may suggest a longer duration of water, greater heat, or higher alkalinity near Antoniadi then for other locations of hydrated phases globally. Finally, phyllosilicates and silica are particularly efficient for the long-term preservation of organic material [*Farmer and Des Marais,* 1999]. Phyllosilicates are capable of sequestering biosignatures within their sheet structure and preserving them through geologic time [*Peeters,* 2007], and silica is shown to precipitate quickly from solution in geologic settings, thereby rapidly entombing biologic material and remaining chemically inert on

geologic time scales [*Farmer and Des Marais,* 1999]. Thus, the Antoniadi region is especially well-suited for both the development and preservation of evidence of life.

Figures for Chapter 6

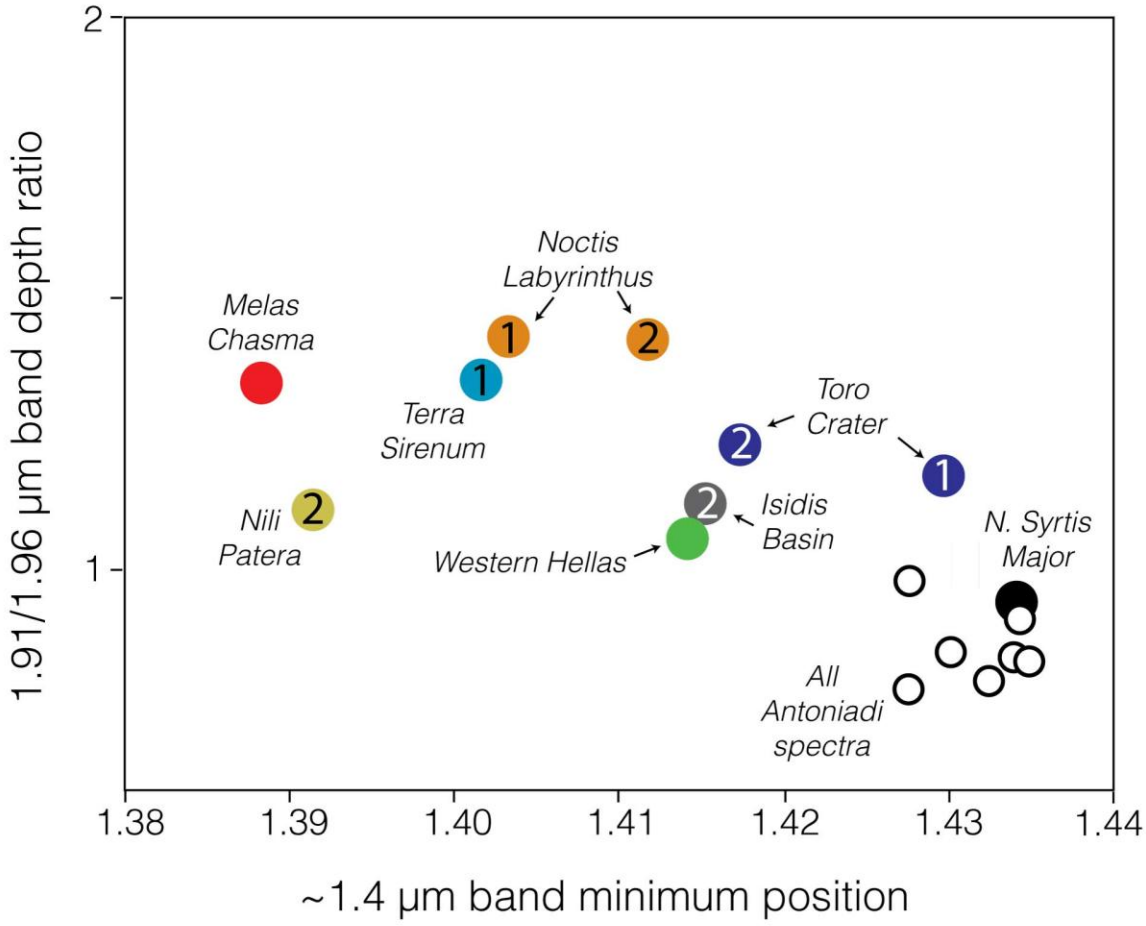

Figure 6.1 — Near-infrared band indices of *Rice et al.* [2012] that are related to the relative crystallinity of the deposits. More crystalline deposits plot toward the lower right of this plot. Hydrated silica detections appear to have a consistently higher degree of crystallinity than other deposits on the planet.

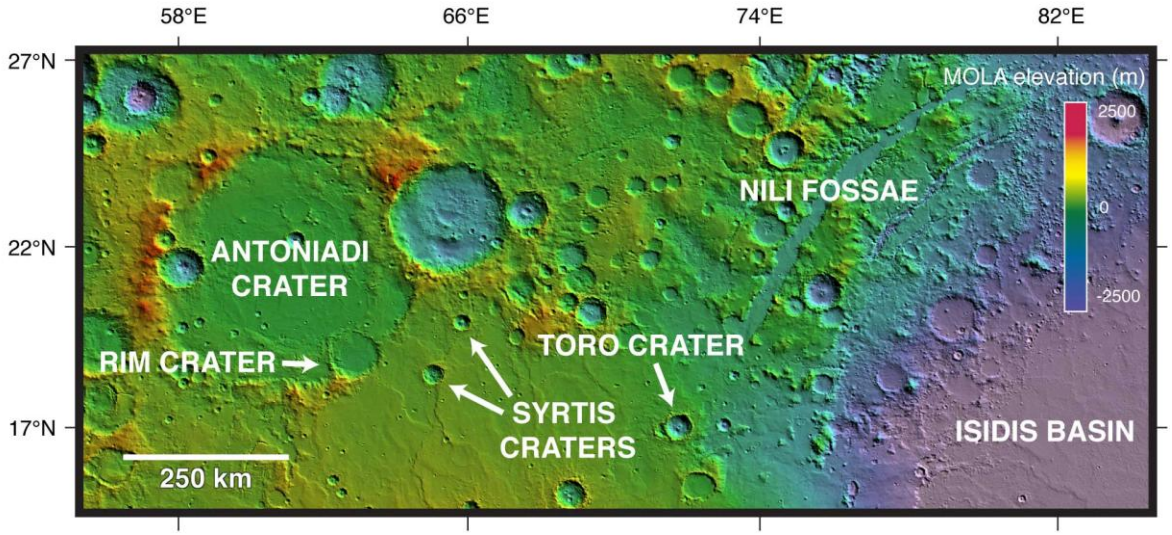

Figure 6.2 — Image of the broader region around Antoniadi, including nearby Nili Fossae and Toro Crater.

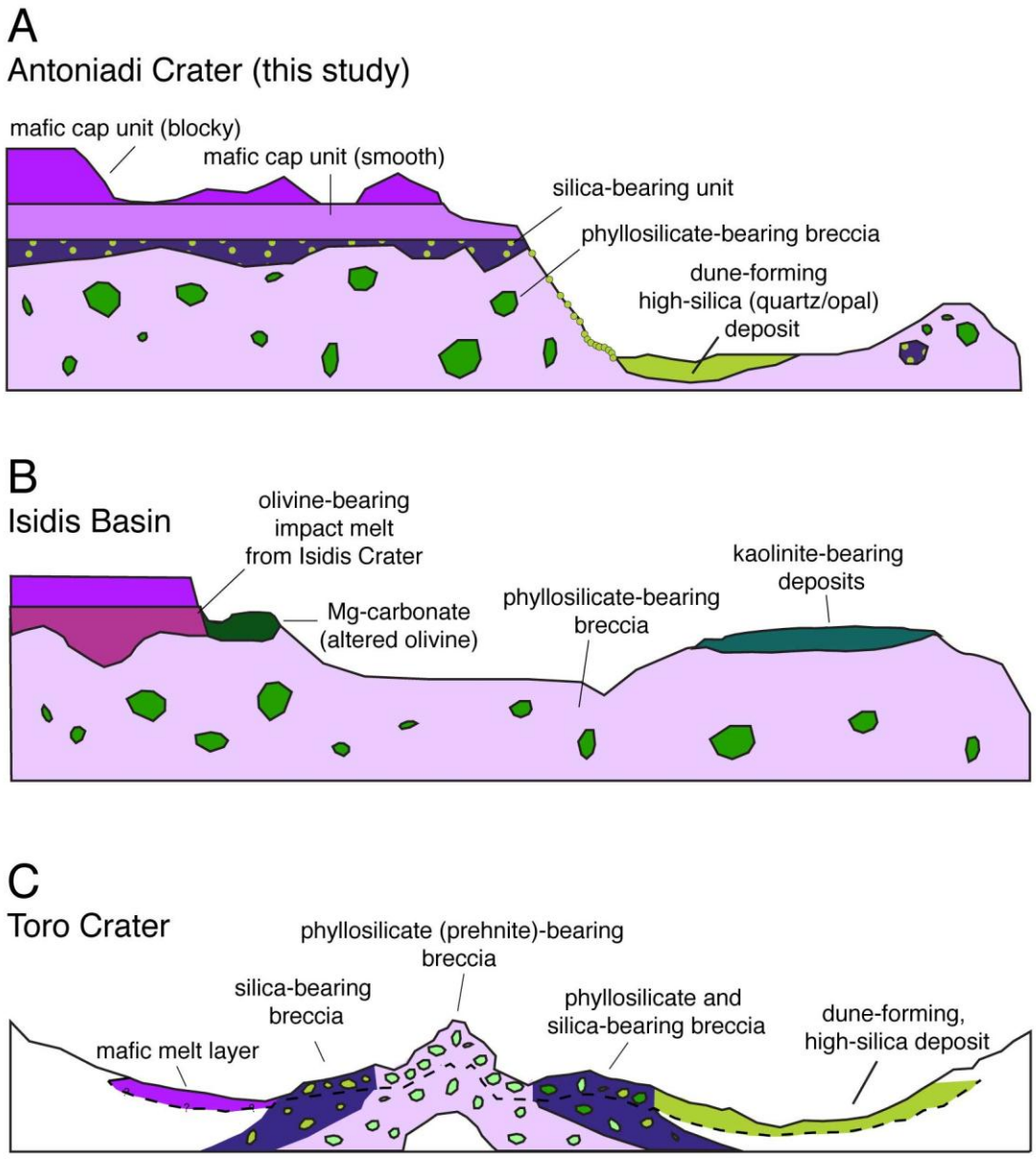

Figure 6.3 — Comparison of geological cross-sections of Antoniadi Crater (this study), Nili Fossae (modified from *Mustard et al.*, 2009) and Toro Crater (modified from *Marzo et al.*, 2010). These areas share a basement layer of a phyllosilicate-bearing breccia overlain by units with minerals that suggest a subsequent pulse of alteration: quartz-bearing units in Antoniadi Crater region, kaolinite and carbonate near the Isidis Basin, and hydrated silica in Toro Crater.

Chapter 7 | Summary and conclusions

Hydrated silica forms easily in nature and is commonly one of the first minerals to precipitate during the aqueous low-temperature weathering of rocks. Because of this, it may be found in a variety of aqueously altered environments on Earth regardless of solution chemistry, temperature, pressure, water availability, or protolith composiiton. It is this indiscriminate formation that makes hydrated silica a useful, yet difficult, mineral for reconstructing the past aqueous histories of Martian surfaces. It is useful because it exists in a variety of deposit types with disparate ages, and within acidic-, neutral-, and alkaline-derived mineral suites. In this capacity, hydrated silica is the only mineral that can be used to directly compare these many aqueously altered Martian deposits with one another. However, it is a difficult mineral to study because of its nonselective formation conditions, so that the presence of hydrated silica alone can reveal very little about the conditions when it was formed. Therefore, the question becomes: what *can* hydrated silica tell us about its past?

It is with this in mind that these studies were performed. The first portion of this dissertation (Chapter 4), analyzed all detections of hydrated silica to determine the relative degrees of silica crystallinity and the SiO_2 abundance of each deposit, both of which were used as proxies for the relative degree of alteration between deposits. The crystallinities of the hydrated silica varied between quartz (N. Syrtis Major/Antoniadi Crater) to amorphous phases (Western Hellas, Isidis Basin, Terra Sirenum, Noctis Labyrinthus, Toro Crater), and possibly to hydrated silicate glass (Melas Chasma, Nili Patera). These crystallinities are indicative of a range in the degree of alteration that

each deposit was subjected to, defined as a combination of water-rock contact, temperature, pH, pressure, and salinity. The silica concentrations of these deposits were mostly near that of Surface Type 2 — a basaltic andesite composition (~58% SiO_2; *Hamilton et al.,* 2001) — although some had elevated compositions that ranged up to granitic (~70%, Western Hellas). If the orbital silica detections are true reflections of the bulk silica of the deposit, those with SiO2 concentrations similar to Surface Type 2 do not indicate high volumes of water-rock contact to alter rock and deposit large amounts of silica.

Combined, the crystallinity and composition data at times are consistent. At both the low and high extremes of crystallinity, there is good agreement with the estimated amounts of silica, suggesting that these deposits are more accurately recording the amount of alteration that they have been subjected to. However, in some of the intermediary cases, there are deposits (Toro Crater, Terra Sirenum) that show discordant silica crystallinities and abundances, suggesting that either additional processes may be affecting the properties of the silica (elevated temperatures, low water-rock contact), or that the silica that may be detected from orbit is not an accurate depiction of the total nature of the deposit, such as the case with silica deposits at Gusev Crater.

The second portion of the dissertation focuses on one specific location of hydrated silica that is also the site of the only detection of quartz on Mars: N. Syrtis Major/Antoniadi Crater. With near-infrared and thermal spectroscopy, the spatial coincidence between

the quartz-bearing and hydrated-silica-bearing units is confirmed, and found distributed in many deposits separated by 100–200 km. Their association suggests a diagenetic origin for the quartz, rather than as an igneously derived phase, as previous studies have assumed. Furthermore, the high-silica units are only associated with mobile, light-toned, dune-forming units in topographic basins. The apparent source rock of the light-toned sediment that comprises the dunes has no detectable silica, which suggests that silica exists as a minor phase in the source rocks, and is concentrated as the rock erodes and sediment is transported. Furthermore, the silica-bearing unit is also stratigraphically above a phyllosilicate-bearing brecciated basement unit that is consistent among many altered mineral suites in the area (Isidis Basin/Nili Fossae and Toro Crater). This may suggest that the Antoniadi Crater region shares a common stratigraphy as these deposits, and that the aqueous event that formed quartz also formed more altered aqueous phases at other sites in the region.

This dissertation demonstrates two final and important points: 1) that the combination of thermal- and near-infrared spectroscopy is a powerful method for providing a more complete picture of planetary geology, and 2) hydrated silica is a potentially useful method for ascertaining the aqueous history of deposits so that we may single out those sites with greater access to water for future landed missions.

Bibliography

Adams, J. B. and A. R. Gillespie (2006), *Remote Sensing of Landscapes with Spectral Images*, Cambridge University Press, UK.

Aines, R. D. and G. R. Rossman (1984), Water in minerals? A peak in the infrared, *J. Geophys. Res.,* 89(B6), 4059–4071.

Amador, E. S. and Bandfield, J. L. (2011) Mars aqueous mineralogy: A comparison of thermal-infrared and visible/near-infrared spectral data, presented at The International Conference: Exploring Mars Habitability, Lisbon, Portugal, June 13–15.

Anderson, J. H. and K. A. Wickersheim (1964), Near infrared characterization of water and hydroxyl on silica surfaces, *Surf. Sci.*, 2, 252–260.

Argast, S. and T. W. Donnelly (1987), The chemical discrimination of clastic sedimentary components, *J. Sediment. Petrol.*, 57 (5), 813–823.

Arvidson, R. E. et al. (2006), Overview of the Spirit Mars Exploration Rover Mission to Gusev Crater: Landing site to Backstay Rock in the Columbia Hills, *J. Geophys. Res.*, 111, E02S01, doi:10.1029/2005JE002499.

Arvidson, R. E. et al. (2008), Spirit Mars Rover Mission to the Columbia Hills, Gusev Crater: Mission overview and selected results from the Cumberland Ridge to Home Plate, *J. Geophys. Res.,* 113, E12S33, doi:10.1029/2008JE003183.

Baker, V. R. (1979), Erosional processes in channelized water flows on Mars, *J. Geophys. Res.*, 84, B14, 7985–7993, doi:10.1029/JB084iB14p07985.

Baldridge, A. M., S. J. Hook, C. I. Grove and G. Rivera (2009), The ASTER Spectral Library Version 2.0., *Rem Sens. Environ.,* 113, 711–715.

Bandfield J. L. (2006), Extended surface exposures of granitoid compositions in Syrtis Major, Mars, *Geophys. Res. Lett.*, 33, L06203, doi:10.1029/2005GL025f559.

Bandfield, J.L. (2008), High-silica deposits of an aqueous origin in western Hellas Basin, Mars. *Geophys. Res. Lett*. 35, 142–147. doi:10.1029/2008GL033807.

Bandfield, J. L. and C. S. Edwards (2008), Derivation of Martian surface slope characteristics from directional thermal infrared radiometry, *Icarus*, 193, 139–157, doi:10.1016/j.icarus.2007.08.028.

Bandfield, J. L. and W. C. Feldman (2008), Martian high latitude permafrost depth and surface cover thermal inertia distributions, *J. Geophys. Res.*, 113, E08001, doi:10.1029/2007JE003007.

Bandfield, J. L., V. E. Hamilton and P. R. Christensen (2000a), A global view of Martian surface compositions from MGS-TES, *Science*, 287(5458), 1626–1630, doi:10.1126/science.287.5458.1626.

Bandfield, J. L., P. R. Christensen and M. D. Smith (2000b), Spectral dataset factor analysis and endmember recovery: Application to Martian atmospheric particulates, *J. Geophys. Res.*, 105, 9573–9588.

Bandfield, J. L., V. E. Hamilton, P. R. Christensen and H. Y. McSween Jr. (2004a), Identification of quartzofeldspathic materials on Mars, *J. Geophys. Res.*, 109, E10009, doi:10.1029/2004JE002290.

Bandfield, J. L., D. Rogers, M. D. Smith and P. R. Christensen (2004b), Atmospheric correction and surface spectral unit mapping using Thermal Emission Imaging System data, *J. Geophys. Res.*, 109, E10008, doi:10.1029/2004JE002289.

Barnhart, C. J. and F. Nimmo (2011), Role of impact excavation in distributing clays over Noachian surfaces, *J. Geophys. Res.*, 116, E01009, doi:10.1029/2010JE003629.

Barnhart, C. J., F. Nimmo and B. J. Travis (2010), Martian post-impact hydrothermal systems incorporating freezing, *Icarus*, 208, 101–117.

Bayly, J. G., V. B. Kartha and W. H. Stevens (1963), The absorption spectra of liquid phase H_2O, HDO, and D_2O from 0.7 μm to 10 μm, *Infrar. Phys.*, 3, 211–223.

Bibring, J.-P. et al. (2006), Global mineralogical and aqueous Mars history derived from OMEGA/Mars Express data, *Science*, 312, 400–404.

Bishop, J. L. and C. M. Pieters (1995), Low-temperature and low atmospheric pressure infrared reflectance spectroscopy of Mars soil analog materials, *J. Geophys. Res.,* 100(E3), 5369–5379.

Bishop, J. L. et al. (2007), Characterization of alteration products in tephra from Haleakala, Maui: A visible-infrared spectroscopy, Mossbauer spectroscopy, XRD, EMPA, and TEM study, *Clays Clay Mineral.*, 55, 1–17, doi:10.1346/CCMN.2007.0550101.

Bishop, J. L., et al. (2008), Phyllosilicate diversity and past aqueous activity revealed at Mawrth Vallis, Mars, *Science*, 321, 830–833.

Buczkowski, D. L., et al. (2010), Investigation of an Argyre basin ring structure using Mars Reconnaissance Orbiter/Compact Reconnaissance Imaging Spectrometer for Mars, *J. Geophys. Res.,* E12011, doi: 10.1029/2009JE003508.

Buswell, A. M., V. Deitz and W. H. Rodebush (1937), A study of the effect of hydrogen bonding upon the infrared absorption of the hydroxyl group, *J. Chem. Phys.*, 5(7), 501–504, doi:10.1063/1.1750065.

Carozzi, A. V. (1993), *Sedimentary Petrography,* 263 pp., Prentice Hall, Englewood Cliffs, New Jersey.

Carr, M. H. (1979), Formation of Martian flood features by release of water from confined aquifers, *J. Geophys. Res.,* 84, B6, 2995–3007.

Carr, M. H. (1995), The Martian drainage system and the origin of valley networks and fretted channels, *J. Geophys. Res.,* 100, E4, 7479–7507.

Christensen, P. R. et al. (1992), Thermal Emission Spectrometer experiment: Mars Observer Mission, *J. Geophys. Res.*, 97, 7719–7734.

Christensen, P. R. et al. (2001), The Mars Global Surveyor Thermal Emission Spectrometer experiment: Investigation description and surface science results, *J. Geophys. Res.*, 106, 23,823–23,871.

Christensen, P. R. et al. (2004), The Thermal Emission Imaging System (THEMIS) for the Mars 2001 Odyssey Mission, *Space Sci. Rev.*, 110, 85–130.

Christensen, P. R. et al. (2005), Evidence for magmatic evolution and diversity on Mars from infrared observations, *Nature*, 436, doi:10.1038/nature03639.

Clark, R. N. (1981), The spectral reflectance of water-mineral mixtures at low temperatures, *J. Geophys. Res.,* 86(B4), 3074–3086.

Clark, R. N. and T. L. Roush (1984), Reflectance spectroscopy: Quantitative analysis techniques for remote sensing applications, *J. Geophys. Res.*, 89(B7), 6329–6340.

Dekov, V. et al. (2008), Hydrothermal sediment alteration at a seafloor vent field: Grimsey Graben, Tjörnes Fracture Zone, north of Iceland, *J. Geophys. Res.,* 113, B11, 10:1029/2007JB005526.

Dixon, J. C. and S. J. McLaren (2009), Duricrusts, in *Geomorphology of Desert Environments,* edited by A. J. Parsons and A. D. Abrahams, pp. 123–151, Springer Netherlands, Heidelberg, Germany.

Dove, P. M. and J. D. Rimstidt (1994), Silica-water interactions, in *Silica: Physical Behavior, Geochemistry, and Materials Applications, Rev. Miner.*, vol. 29, edited by

P. J. Heaney, C. T. Prewitt, and G. V. Gibbs, pp. 259-308, Mineral. Soc. Amer. Washington, D. C.

Edwards, C. S., J. L. Bandfield, P. R. Christensen and R. L. Fergason (2009), Global distribution of bedrock exposures on Mars using THEMIS high-resolution thermal inertia, *J. Geophys. Res.,* 114, E11001, doi:10.1029/2009JE003363.

Ehlmann, B.L. et al. (2008), Orbital identification of carbonate-bearing rocks on Mars, *Science*, 322, doi: 10.1126/science.1164759.

Ehlmann, B.L., et al. (2009), Identification of hydrated silicate minerals on Mars using MRO-CRISM: Geologic context near Nili Fossae and implications for aqueous alteration, *J. Geophys. Res.*, 114, doi: 10.1029/2009JE003339.

Ehlmann, B.L. et al. (2010a), Geologic setting of serpentine deposits on Mars, *Geophys. Res. Lett.*, 37, L06201.

Ehlmann, B. L. et al. (2010b), Impact craters as probes of the ancient Martian Southern Highlands: Insights on aqueous alteration, Abstract #P44B-05 presented at 2010 Fall Meeting, AGU, San Francisco, CA.

Ehlmann, B. L. et al. (2011), Subsurface water and clay mineral formation during the early history of Mars, *Nature*, 479, 53–60, doi:10.1038/nature10582.

Errera, J. and P. Mollet (1936), Intermolecular forces and O–H absorption bands in alcohols, *Nature*, 138, 882–882.

Eugster, H. P. (1967), Hydrous sodium silicates from Lake Magadi, Kenya: Precursors of bedded c hert, *Science*, 157, 1177–1180.

Eugster, H. P. (1969), Inorganic bedded cherts from the Magadi Area, Kenya, *Contr. Min. Pet.,* 22, 1–31.

Evans, J. R. (1962), Falling and climbing sand dunes in the Cronese ("Cat") Mountain area, San Bernadino County, California, *J. Geology*, 70(1), 107–113.

Fairen, A. G., A. F. Davila, L. Gago-Duport, R. Amils and C. P. McKay (2009), Stability against freezing of aqueous solutions on early Mars, *Nature*, 459(7245), 401–4.

Farmer, J. D. and D. J. Des Marais (1999), Exploring for a record of ancient Martian life, *J. Geophys. Res., 104*, E11, 26,977–26,995.

Farr, T. G. and J. B. Adams (1984), Rock coatings in Hawaii, *Geol. Soc. Am Bull.,* 95(9), 1077–1083.

Fassett, C. I. and J. W. Head III (2005), Fluvial sedimentary deposits on Mars: Ancient deltas in a crater lake in the Nili Fossae region, *Geophys. Res. Lett.,* 32(14), 10.1029/2005GL023456.

Fassett, C. I. and J. W. Head III (2008), The timing of Martian valley network activity: Constraints from buffered crater counting, *Icarus, 195*, doi:10.1016/j.icarus.2007.12.009.

Fergason, R. L., P. R. Christensen and H. H. Kieffer (2006a), High-resolution thermal inertia derived from Thermal Emission Imaging System (THEMIS): Thermal model and applications, *J. Geophys. Res.,* 111, E12004, doi:10.1029/2006JE002735.

Fergason, R. L. et al. (2006b), Physical properties of the Mars Exploration Rover landing sites as inferred from Mini-TES-derived thermal inertia, *J. Geophys. Res.*, 111, E02S21, doi:10.1029/2005JE002583.

Flörke, O. W., B. Köhler-Herbertz, K. Langer and I. Tönges (1982), Water in microcrystalline quartz of volcanic origin: Agates, *Contrib. Mineral. Petrol.* 80, 324–333.

Flörke, O. W., H. Graetsch, B. Martin, K Röller and R. Wirth (1991), Nomenclature of micro- and non-crystalline silica minerals, based on structure and microstructure, *Neues Jahrbuch Miner. Abh.*, 163(1), 19–42.

Flörke, O. W. et al. (2008), Silica, in *Ullmann's Encyclopedia of Industrial Chemistry*, pp. 421–507, VCH Publishers, Inc.

Folk, R. L. and C. E. Weaver (1952), A study of the texture and composition of chert, *Am. J. Sci*., 250, 498–510.

Folk, R. L. and J. S. Pittman (1971), Length-slow chalcedony: A new testament for vanished evaporites, *J. Sed. Petrol.*, 41(4), 1045–1058.

Fournier, R. O. (1985), The behavior of silica in hydrothermal systems, in *Geology and Geochemistry of Epithermal Systems, Rev. Econ. Geol.,* B. R. Berger and P. M. Bethke (Eds.), pp. 45–61, Society of Economic Geologists, Littleton, CO.

Frondel, C. (1962), *The System of Mineralogy of James Dwight Dana and Edward Salisbury Dana*: *Volume III, Silica Minerals*, 7th ed., John Wiley and Sons Inc., New York.

Gao, G. and L. S. Land (1991), Early Ordovician Cool Creek dolomite, Middle Arbuckle Group, Slick Hills, SW Oklahoma, USA: Origin and modification, *J. Sed. Pet.*, 61(2), 161–173.

Gillespie, A. R., and E. A. Abbott (1984), Mapping compositional differences in silicate rocks with 6-channel thermal images. *Proceedings of the 9th Canadian Symposium on Remote Sensing,* St. Johns, Newfoundland, Canada, Aug., 327–336.

Gillespie, A. R., A. B. Kahle and R. E. Walker (1986), Color enhancement of highly correlated images: I. Decorrelation and HSI contrast stretches, *Remote Sens. Environ*., 20, 209–235.

Glotch, T. D. et al. (2006), Mineralogy of the light-toned outcrop at Meridiani Planum as seen by the Miniature Thermal Emission Spectrometer and implications for its formation, *J. Geophys. Res.*111, doi:10.1029/2005JE002672.

Goryniuk, M. C., B. A. Rivard and B. Jones (2004), The reflectance of opal-A (0.5-25 μm) from the Taupo Volcanic Zong: Spectra that may identify hydrothermal systems on planetary surfaces, *Geophys. Res. Lett.*, 31, L24701, doi:10.1029/2004GL021481.

Graetsch, H (1994), Structural characteristics of opaline and microcrystalline silica minerals, in *Silica: Physical Behavior, Geochemistry, and Materials Applications, Rev. Miner.*, vol. 29, edited by P. J. Heaney, C. T. Prewitt, and G. V. Gibbs, pp. 209-232, Mineral. Soc. Amer. Washington, D. C.

Graetsch, H., O. W. Flörke and G. Miehe (1985), The nature of water in chalcedony and opal-C from Brazilian agate geodes, *Phys. Chem. Mineral.,* 12, 300–306.

Graetsch, H. H. Gies and I. Topalović (1994), NMR, XRD, and IR study on microcrystalline opals, *Phys. Chem. Mineral.,* 21, 166–175.

Grant, J. A. et al. (2008), HiRISE imaging of impact megabreccia and sub-meter aqueous strata in Holden Crater, Mars. *Geology*, 36, 195–198, doi:10.1130/G24340A.1.

Hamilton, V. E. and P. R. Christensen (2005), Evidence for extensive, olivine-rich bedrock on Mars, *Geology, 33*, 433–436.

Hamilton, V. E., P. R. Christensen, H. Y. McSween Jr. and J. L. Bandfield (2003), Searching for the source regions of Martian meteorites using MGS TES: Integrating Martian meteorites into the global distributions of igneous materials on Mars, *Meteorit. Planet. Sci.*, 38, 871–885.

Hapke, B. (1993), *Theory of Reflectance and Emittance Spectroscopy*, Cambridge University Press, Cambridge, UK.

Hay, R. L. (1966), Zeolites and zeolitic reactions in sedimentary rocks, *Special GSA Papers, 85,* pp. 130.

Hay, R. L. and A. Iijima (1968), Petrology of palagonite tuffs of Koko Craters, Oahu, Hawaii, *Contrib. Mineral. Petrol.*, 17, 141–154, doi:10.1007/BF00373206.

Heaney, P. J. (1993), A proposed mechanism for the growth of chalcedony, *Contrib. Mineral. Petrol.*, 115, 66–74.

Heaney, P. J. (1994), Structure and chemistry of the low-pressure silica polymorphs, in *Silica: Physical Behavior, Geochemistry, and Materials Applications, Rev. Miner.*, vol. 29, edited by P. J. Heaney, C. T. Prewitt, and G. V. Gibbs, pp. 1-40, Mineral. Soc. Amer. Washington, D. C.

Herdianita, N. R., P. R. L. Browne, K. A. Rodgers and K. A. Campbell (2000), Mineralogical and textural changes accompanying ageing of silica sinter, *Mineralium Deposita*, 35, 48–62, doi: 10.1007/s001260050005.

Herzberg, G. (1945), *Molecular Spectra and Molecular Structure. II. Infrared and Raman Spectra of Polyatomic Molecules,* 632 p., Van Nostrand, New York.

Hesse, R. H. (1989), Silica Diagenesis: Origin of inorganic and replacement cherts, *Earth Sci. Rev.*, 26, 253–284.

Hiesinger, H. and J. W. Head III (2004), The Syrtis Major volcanic province, Mars: Synthesis from Mars Global Surveyor data, *J. Geophys. Res.*, 109, E01004, doi:10.1029/2003JE002143.

Hoefen, T. M., R. N. Clark, J. L. Bandfield, M. D. Smith, J. C. Pearl and P. R. Christensen (2003), Discovery of olivine in the Nili Fossae region of Mars, *Science, 302*, 627–630.

Humphris, S. E. and G. Thompson (1978), Hydrothermal alteration of oceanic basalts by seawater, *Geochim. Cosmochim. Acta.*, 42, 107–125.

Hunt, G. R. (1977), Spectral signatures of particulate minerals in the visible and near infrared, *Geophys.*, 42(3), 501–513.

Iler, R. K. (1979), *The Chemistry of Silica*, John Wiley and Sons, New York.

Jolliffe, I. T. (2002), *Principal Component Analysis,* Springer, Netherlands, Heidelberg, Germany.

Kahle, A. B., et al. (1988), Relative dating of Hawaiian lava flows using multispectral thermal infrared images: A new tool for geologic mapping of young volcanic terranes*, J. Geophys. Res.,* 93(B12), 15,239–15.251.

Kastner, M., J. B. Keene and J. M. Gieskes (1977), Diagenesis of siliceous oozes – I. Chemical controls on the rate of opal-A to opal-CT transformation – an experimental study, *Geochim. Cosmochim. Acta,* 41, 1041–1059.

Kieffer, H. H., T. N. Titus, K. F. Mullins and P. R. Christensen (2000), Mars south polar spring and summer behavior observed by TES: Seasonal cap evolution controlled by frost grain size, *J. Geophys. Res.*, 105, 9653–9699, doi:10.1029/1999JE001136.

Knauth, P. L. (1994), Petrogenesis of chert, *Rev. Mineral. Geochem.*, 29, 223–258.

Kraft, M. D., J. R. Michalski, and T. G. Sharp (2003). Effects of pure silica coatings on thermal emission spectra of basaltic rocks: Considerations for martian surface mineralogy. *Geophys. Res. Lett.* 30. doi:10.1029/2003GL018848.

Langer, K. and O. W. Flörke (1974), Near infrared absorption spectra (4000-9000 cm^{-1}) of opals and the role of "water" in these $SiO_2 \cdot nH_2O$ minerals, *Fortschr. Mineral.,* 52(1), 17–51.

Leatherman, M. (2010), Geochemistry and reaction path modeling of the Beowawe hydrothermal system, Nevada: a barren end-member epithermal system, *M.S. Thesis,* Univ. of Missouri.

Lippincott, E., R. A. Van Valkenburg, C. E. Weir and E. N. Bunting (1958), Infrared studies on polymorphs of silicon dioxide and germanium dioxide, *J. Res. Nation. Bur. Stand.,* 61(1), 61–70.

Lynne, B. Y., K. A. Campbell, J. N. Moore and P. R. L. Browne (2005), Diagenesis of 1900-year-old siliceous sinter (opal-A to quartz) at Opal Mound, Roosevelt Hot Springs, Utah, U. S. A., *Sed. Geol.*, 179, 249–278.

Lyon, R. J. P. (1965), Analysis of rocks by spectral infrared emission (8 to 25 microns), *Econ. Geol*., 60, 715–736.

Maher Jr., H. and R. Shuster (2012), Chalcedony vein horizons and clastic dikes in the White River Group as products of diagenetically driven deformation, *Lithosphere,* doi: 10.1130/L187.1.

Malin, M. C. and K. S. Edgett (2003), Evidence for persistent flow and aqueous sedimentation on early Mars, *Science*, 302(5562), 1931–1934, doi:10.1126/science.1090544.

Malin M. C. et al. (2007), Context Camera investigation on board the Mars Reconnaissance Orbiter, *J. Geophys. Res.*, 112, E05S04, doi:10.1029/2006JE002808.

Maliva, R. G. and R. Siever (1988), Diagenetic replacement controlled by force of crystallization, *Geology*, 16, 688-691, doi:10.1130/0091-7613(1988)016.

Marzo, G. A. et al. (2010), Evidence for Hesperian impact-induced hydrothermalism on Mars, *Icarus*, 208, 667–683.

McCoy, T. J. et al. (2008), Structure, stratigraphy, and origin of Husband Hill, Columbia Hills, Gusev Crater, Mars, *J. Geophys. Res.,* 113, E06S03, doi:10.1029/2007JE003041.

McDonald, R. S. (1958), Surface functionality of amorphous silica by infrared spectroscopy, *J. Phys. Chem.,* 62(10), 1168–1178.

McDowell, M. L. (2009), Laboratory and applied studies using thermal infrared spectroscopy and other remote sensing tools for the understanding of the geologic history of Mars, *Ph.D. Thesis,* Univ. of Hawaii.

McEwen, A. S. et al. (2007), Mars Reconnaissance Orbiter's High Resolution Imaging Science Experiment (HiRISE), *J. Geophys. Res.*, 112, E05S02, doi:10.1029/2005JE002605.

McGuire, P. C. et al. (2009), An improvement to the volcano-scan algorithm for atmospheric correction of CRISM and OMEGA spectral data, *Planet. Space Sci.*, 57(7), doi:10.1016/j.pss.2009.03.007.

McKeown, N. K. et al. (2011), Interpretation of reflectance spectra of clay mineral-silica mixtures: Implications for Martian clay mineralogy at Mawrth Vallis, *Clays Clay Mineral.,* 59(4), 400–415.

McLennan, S. M. (2003), Sedimentary silica on Mars, *Geology*, 31, 315–318, doi:10.1130/0091-7613(2003)031.

McSween Jr., H. Y. (1985), SNC meteorites: Clues to Martian petrologic evolution, *Rev. Geophys.* 23, 391–416, doi:10/1029/RG023i004p00391.

Mellon, M. T., B. M. Jakosky, H. H. Kieffer and P. R. Christensen (2000), High-resolution thermal inertia mapping from the Mars Global Surveyor Thermal Emission Spectrometer, *Icarus,* 148, 437–455, doi:/10.1006/icar.2000.6503.

Melosh, H. J. (1989), *Impact Cratering: A Geologic Process*, Clarendon Press, Oxford, UK.

Michalski, J. R. et al. (2003), Thermal emission spectroscopy of the silica polymorphs and considerations for remote sensing of Mars, *Geophys. Res. Lett.*, 30, doi:10.1029/2003GL019354.

Miller, S. L. and L. E. Orgel (1974), *The Origins of Life on the Earth*, Prentice-Hall, Englewood Cliffs, NJ.

Milliken, R. E. et al. (2008), Opaline silica in young deposits on Mars, *Geology*, 36, 847–850, doi:10.1130/G24967A.1.

Milliken, R. E., D. L. Bish, T. Bristow and J. F. Mustard (2010), presented at 2010 Lunar Planet. Sci. Conf., The Woodlands, TX.

Moore, J. M., A. D. Howard, W. E. Dietrich and P. M. Schenk (2003), Martian layered fluvial deposits: Implications for Noachian climate scenarios, *Geophys. Res. Lett.,* 30, 2292, doi:10.1029/2003GL019002.

Morris, R. V. et al. (2010), Identification of carbonate-rich outcrops on Mars by the Spirit Rover, *Science*, 329(5990), 421–424, doi: 10.1126/science.1189667.

Morse, J. W. and W. H. Casey (1988), Ostwald processes and mineral paragenesis in sediments, *Am. J. Sci.*, 288, 537–560.

Murchie, S. L. et al. (2007), Compact Reconnaissance Imaging Spectrometer for Mars (CRISM) on Mars Reconnaissance Orbiter (MRO), *J. Geophys. Res.*, 112, E05S03, doi:10.1029/2006JE002682.

Murchie, S. L. et al. (2009), A synthesis of Martian aqueous mineralogy after 1 Mars year of observations from the Mars Reconnaissance Orbiter*, J. Geophys. Res.*, 114, E00D06, doi:10.1029/2009JE003342.

Murray, H. H. (1988), Kaolin minerals: Structures and stabilities, in Reviews of Mineralogy, vol. 19, *Hydrous Phyllosilicates (Exclusive of Micas),* edited by S. W. Bailey, pp. 67–87, Mineral. Soc. of Am., Washington, D. C.

Mustard, J. F. et al. (2005), Olivine and pyroxene diversity in the crust of Mars, *Science*, 307(5715), 1594–1597, doi:10.1126/science.1109098.

Mustard, J. F. et al. (2009), Composition, morphology, and stratigraphy of noachian Crust around the Isidis basin, *J. Geophys. Res.*, 114, E00D12, doi:10.1029/2009JE003349.

Nesbitt, H. W. and G. M. Young (1989), Formation and diagenesis of weathering profiles, *J. Geol.,* 97, 129–147.

Newsom, H. E., G. Graup, T. Sewards and K. Keil (1986), Fluidization and hydrothermal alteration of the suevite deposit at the Ries Crater, West Germany and implications for Mars, *J. Geophys. Res., 91,* E239-E251.

Noe Dobrea, E. Z. et al. (2010), Mineralogy and stratigraphy of phyllosilicate-bearing and dark mantling units in the greater Mawrth Vallis/west Arabia Terra area: Constraints on geological origin, *J. Geophys. Res.,* 115, E00D19, doi:10/1029/2009JE003351.

Osinski, G. R. (2005), Hydrothermal activity associated with the Ries impact event, Germany, *Geofluids,* 5, 202–220, doi:10.1111/j.1468-8123.2004.00119.x.

Parente, M. (2008), A new approach to denoising CRISM images, presented at 2008 Lunar Planet. Sci. Conf., League City, TX.

Peeters, Z. (2007), On the stability of molecules and microorganisms in interstellar and planetary environments, *Ph.D. Thesis,* Leiden University.

Pieri, D. C. (1980), Martian valleys: Morphology, distribution, age, and origin, *Science,* 210(4472), 895–897, doi:10.1126/science.210.4472.895.

Putzig, N. E., M. T. Mellon, K. A. Kretke and R. E. Arvidson (2005), Global thermal inertia and surface properties of Mars from the MGS mapping mission, *Icarus,* 173, 325–341, doi:10.1016/j.icarus.2004.08.017.

Rice, M. S. et al. (2010), Silica-rich deposits and hydrated minerals at Gusev Crater, Mars: Vis-NIR spectral characterization and regional mapping, *Icarus*, 205(2), 375–395.

Rice, M. S. et al. (2012), Reflectance spectra diversity of silica-rich materials: Sensitivity to environment and implications for detections on Mars. *Icarus,* in revision.

Rimstidt, J. D. and H. L. Barnes (1980), The kinetics of silica-water reactions, *Geochim. Cosmochim. Acta,* 44, 1683–1699.

Rimstidt, J. D. and D. R. Cole (1983), Geothermal mineralization I: The mechanism of formation of the Beowawe, Nevada, siliceous sinter deposit, *Am. J. Sci.*, 283, 861–875.

Rodgers, K. A. et al. (2004), Silica phases in sinters and residues from geothermal fields of New Zealand, *Earth. Sci. Rev.*, 66, 1–61.

Rogers, A. D. and J. L. Bandfield (2009), Mineralogical characterization of Mars Science Laboratory candidate landing sites from THEMIS and TES data, *Icarus,* 203(2), 437–453.

Rooney, T. P. (1969), Magadiite from Alkali Lake, Oregon, *Am. Mineral.*, 54, 1034–1043.

Ruff, S. W. et al. (2011), Characteristics, distribution, origin, and significance of opaline silica observed by the Spirit rover in Gusev crater, Mars, *J. Geophys, Res.*, 116, E00F23, doi:10.1029/2010JE003767.

Schiffman, P. and H. W. Day (1999), Petrological methods for the study of very low-grade metabasites, in *Low-Grade Metamorphism*, edited by M. Frey and D. Robinson, Blackwell, Oxford, UK.

Sebag, D., E. P. Verrecchia, S.-J. Lee and A. Durand (2001), The natural hydrous sodium silicates from the northern bank of Lake Chad: occurrence, petrology and genesis, *Sed. Geol.*, 139, 15–31, doi:10.1016/S0037-0738(00)00152-4.

Seelos, F. P. et al. (2011), CRISM data processing and analysis products update – Calibration, correction, and visualization, presented at the Lunar and Planetary Science Conference XXII (#1438), The Woodlands, TX.

Skok, J. R., J. F. Mustard, B. L. Ehlmann, R. E. Milliken and S. L. Murchie (2010), Silica deposits in the Nili Patera caldera on the Syrtis Major volcanic complex on Mars, *Nature Geosci.,* doi:10.1038/ngeo990.

Smale, D. (1973), Silcretes and associated silica diagenesis in southern Africa and Australia, *J. Sed. Res.*, 43, 1077–1089, doi:10.1306/74D728FB-2B21-11D7-8648000102C1865D.

Smith, D. E. et al. (2001), Mars Orbiter Laser Altimeter: Experiment summary after the first year of global mapping of Mars, *J. Geophys. Res.,* 106, 23,689–23,722, doi:10.1029/2000JE001364.

Smith, D. K. (1998), Opal, cristobalite, and tridymite: Noncrystallinity versus crystallinity, nomenclature of the silica minerals and bibliography, *Powder Diffraction,* 13(1), 2–19.

Smith, M. D., J. C. Pearl, B. J. Conrath and P. R. Christensen (2001), Thermal Emission Spectrometer results: Mars atmospheric thermal structure and aerosol distribution, *J. Geophys. Res.,* 106, 23,929–23.945.

Smith, M. R. and J. L. Bandfield (2012), Geology of quartz and hydrated-silica-bearing deposits near Antoniadi Crater, Mars, *J. Geophys. Res.*, in press.

Squyres, S. W. et al. (2008), Detection of silica-rich deposits on Mars, *Science*, 320(5879), 1063–1067, doi:10.1126/science.1155429.

Staudigel, H. and S. R. Hart (1983), Alteration of basaltic glass: Mechanisms and significance for the oceanic crust-seawater budget, *Geochim. Cosmochim. Acta.*, 47, doi: 10.1016/0016-7037(83)90257-0.

Stolper, E. (1982), Water in silicate glasses: An infrared spectroscopic study, *Contrib. Mineral. Petrol,* 81, 1–17.

Summerfield, M. A. (1983), Silcrete as a palaeoclimatic indicator: Evidence from southern Africa, *Palaeogeogr. Palaeoclim. Palaeoecol.*, 41, 65–79.

Sunshine, J. M., C. M. Pieters and S. F. Pratt (1990), Deconvolution of mineral absorption bands: An improved approach*, J. Geophys. Res.*, 95(B5), 6955–6966.

Titus, T. N., H. H. Kieffer and P. R. Christensen (2003), Exposed water ice discovered near the south pole of Mars, *Science*, 299(5609), 1048–1051, doi:10.1126/science.1080497.

Tornabene, L. L. et al. (2008), Surface and crater-exposed lithologic units of the Isidis Basin as mapped by coanalysis of THEMIS and TES derived data products, *J. Geophys. Res.*, 113, E10001, doi:10.1029/2007/JE002988.

Tosca, N. J. and A. H. Knoll (2009), Juvenile chemical sediments and the long term persistence of water at the surface of Mars, *Earth Planet. Sci. Lett.,* 286, 379–386.

Turner, C. E. and N. S. Fishman (1991), Jurassic Lake T'oo'dichi': A large alkaline, saline lake, Morrison Formation, eastern Colorado Plateau, *Geol. Soc. Am. Bull.*, 103, 538–558.

Vaughan, R. G., W. M. Calvin and J. V. Taranik (2003), SEBASS hyperspectral thermal infrared data: surface emissivity measurement and mineral mapping, *Rem. Sens. Env.* 85, 48–63.

Vaughan, R. G., S. J. Hook, W. M. Calvin and J. V. Taranik (2005), Surface mineral mapping at Steamboat Springs, Nevada, USA, with multi-wavelength thermal infrared images, *Rem. Sens. Env.* 99, 140–158.

Velde, B. (1995), *Origin and Mineralogy of Clays: Clay and the Environment,* Springer Netherlands, Heidelberg, Germany.

Vincent, R. K. and F. Thomson (1972), Spectral compositional imaging of silicate rocks, *J. Geophys. Res.* 77(14), 2465–2472.

Walter, L. S. and J. W. Salisbury (1989), Spectral characterization of igneous rocks in the 8- to 12-μm region*, J. Geophys. Res.*, 94(B7), 9203–9213.

Weaver, C. E. (1989), *Clays, Muds, and Shales*. Elsevier, New York.

Wilkins, R. W. T. (1967), The hydroxyl-stretching region of the biotite mica spectrum*, Miner. Mag.*, 36, 325–333.

Williams, L. A. and D. A. Crerar (1985), Silica diagenesis, II. General mechanisms, *J. Sed. Pet.*, 55, 312–321.

Williams, L. A., G. A. Parks and D. A. Crerar (1985), Silica diagenesis, I. Solubility controls, *J. Sed. Pet.,* 55, 301–311.

Wray, J. J., B. L. Ehlmann, S. W. Squyres, J. F. Mustard, R. L. Kirk (2008), Compositional stratigraphy of clay-bearing layered deposits at Mawrth Vallis, Mars, *Geophys, Res. Lett.*, 35, L12202, doi:10.1029/2008GL034385.

Wray, J. J., et al. (2011), Columbus crater and other possible groundwater-fed paleolakes of Terra Sirenum, Mars, *J. Geophys. Res.*, 116, E01001, doi:10.1029/2010JE003694.

Wu, C.-K. (1980), Nature of Incorporated Water in Hydrated Silicate Glasses*, J. Am. Cer. Soc.*, 63(7-8), 453–457.

Wyatt, M. B. and H. Y. McSween Jr. (2006), The Orbital Search for Altered Materials on Mars, *Elements,* 2, 145–150.

Appendix A: Omission of silicas in Mawrth Vallis and Arabia Terra

Previously published accounts of hydrated silica in Mawrth Vallis [*Bishop et al.,* 2008] and the greater Arabia Terra region [*Noe Dobrea et al.,* 2010] were omitted from this study for two reasons.

First, the published spectral shapes were not a very good match for hydrated silica, specifically the shape and location of the 2.2 μm feature (Figure A.1). Both *Bishop et al.* [2008] and *Noe Dobrea et al.* [2010] state that their hydrated-silica surfaces are likely a mixture with Al-phyllosilicates (montmorillonite/kaolinite), affecting the shape of the shape of the 2.2 μm feature, which indicates that, at minimum, the spectrum reflects the contribution of other components. Furthermore, the shape of the 2.2 μm feature was analyzed by *McKeown et al.* [2011], who measured the near-infrared spectra of several laboratory mixtures of phyllosilicates, glasses, and hydrated silica and determined that the best fit to the observed putative hydrated silica spectra was a mixture of only phyllosilicates and no silica. Therefore, silica is not a necessary surface component to explain the observed spectra.

Second, if hydrated silica were contributing to these spectra as a component of a mixture, the relative proportions of hydrated silica would be expected to vary within a single CRISM scene. Mathematically, this can be tested this using principal component

analysis (PCA) [*Jolliffe*, 2002] to isolate spectral endmembers that co-vary independent of other scene elements to determine whether the spectrum of hydrated silica is present and a principal component. Retrieved eigenvectors from PCA were compared with the spectrum of hydrated silica, and no spectral match was found. Instead, the only retrieved principal components had a shape near the 2.2 μm region that resembled neither that of hydrated silica nor of the observed spectrum. This suggests that the Arabia Terra spectrum seen by previous researchers was not a spectral mixture of phyllosilicate and hydrated silica phases, but of other unidentified spectral components.

A good spectral fit for the observed Arabia Terra spectra is an Al-Si-OH glass from an alkaline basaltic ash altered in a cinder cone [*Bishop et al.*, 2007]. It has a similar 2.2 μm feature that is attributed to contributions from Fe–OH and Al–OH in a poorly crystalline matrix (Figure A.1), and provides a suitable match with the observed features without the presence of hydrated silica glass.

Because the reported hydrated silica is consistent with a composition that does not contain hydrated silica, and that hydrated silica does not appear to be a contributor to spectral mixtures as calculated through PCA, these spectra have been omitted from this study.

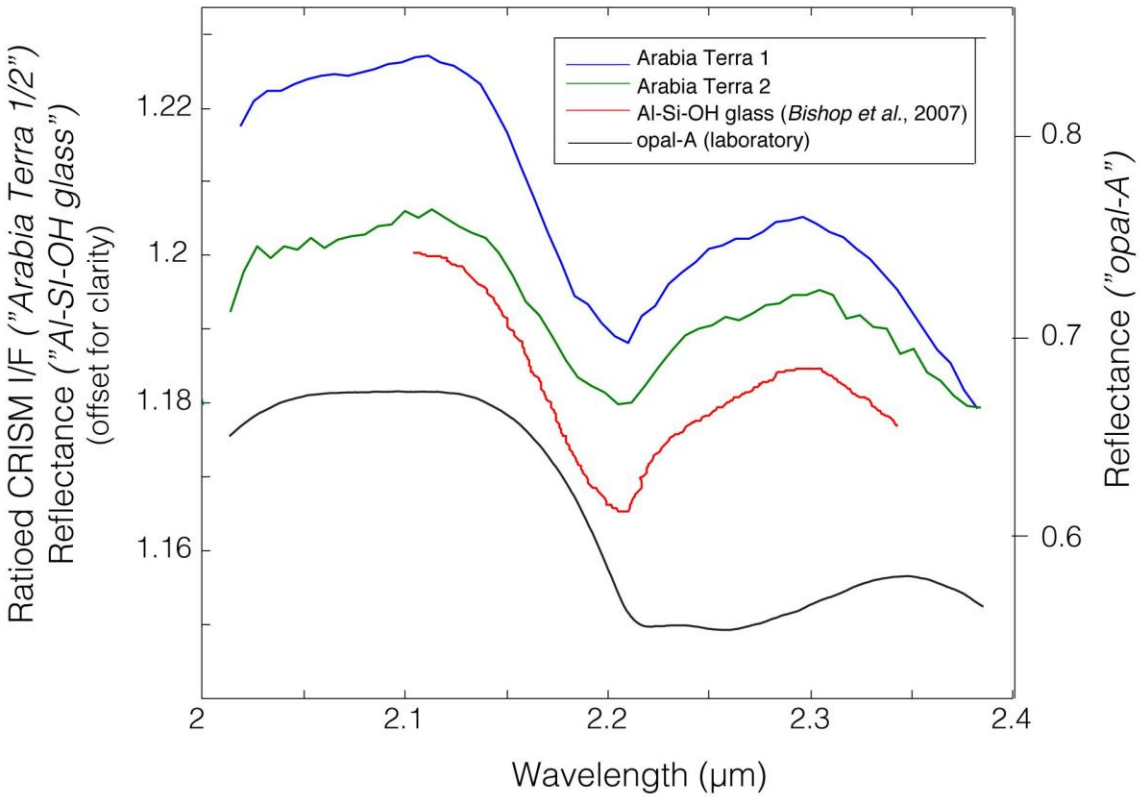

Figure A.1 – Comparison of 2.2 μm Si-OH feature from Arabia Terra relative to laboratory samples. The shape of Martian spectra are not a good match for hydrated silica, but are a better match with amorphous Al-Si-OH glass from Haleakala, Maui, Hawaii [*Bishop et al.* 2007].

VITA

In 1983, Matthew Ryan Smith was born in Porterville, California — a small farm town in the center of the state nestled between orange groves, olive groves and dairy cows. With a head for math and science, he left his agrarian roots for the University of Southern California to seek a career in computer engineering, but found that the natural world was more to his liking. He switched majors a year later, and earned a Bachelor of Sciences degree in Geological Sciences, *magna cum laude*, at USC in 2005. Being partial to the west coast, he moved to Seattle shortly afterward to pursue his new love of the planets, and earned a Doctor of Philosophy at the University of Washington in Geology in 2012 studying Martian geology. In addition to Mars, Matt also enjoys mountains, baking, college football, cycling, and (thanks to grad school) the wonderful joys of coffee.